

BRNO UNIVERSITY OF TECHNOLOGY

Faculty of Electrical Engineering and
Communication

DOCTORAL THESIS



BRNO UNIVERSITY OF TECHNOLOGY

VYSOKÉ UČENÍ TECHNICKÉ V BRNĚ

FACULTY OF ELECTRICAL ENGINEERING AND COMMUNICATION

FAKULTA ELEKTROTECHNIKY
A KOMUNIKAČNÍCH TECHNOLOGIÍ

DEPARTMENT OF RADIOENGINEERING

ÚSTAV RADIOELEKTRONIKY

TERAHERTZ ANTENNA ARRAYS FOR COMMUNICATIONS

TERAHERTZOVÁ ANTÉNNÍ POLE PRO KOMUNIKACI

DOCTORAL THESIS

DIZERTAČNÍ PRÁCE

AUTHOR

AUTOR PRÁCE

Dominika Warmowska, MSc. Eng.

SUPERVISOR

ŠKOLITEL

prof. Dr. Ing. Zbyněk Raida

BRNO 2020

ABSTRACT

The thesis is focused on the research of THz antenna arrays to be used for communications. Attention is turned to modeling metallic surfaces at THz frequencies, a proper characterization of gold conductivity, its relation to Drude model and corresponding measurements. Moreover, the best methods for modeling thin metallic layers (depending on the skin depth related to the metal thickness) are presented.

An optimized element of a THz 2×2 antenna array designed for the application of communications is developed in a way that enables an expansion to a larger array. The expansion ability is demonstrated on a 4×4 antenna array which is presented in the thesis too. The designed antennas achieve parameters better than the state-of-art antennas. The presented antennas radiate circularly polarized wave at THz frequencies, operate in a wide bandwidth, have a high gain and are of a compact size.

In the thesis, an 8×8 antenna array with a beam steering capability is presented. The main beam of the antenna array can be controlled in two dimensions. A high gain of the radiated circularly-polarized wave can be achieved that way.

Different approaches to modeling antennas with thin metallic layers are compared and the best methods are recommended from the viewpoint of different requirements. The designed 2×2 and 4×4 antenna arrays are manufactured using a microfabrication technology. Each step of the fabrication is described in detail and discussed. The reflection coefficient at the input of antennas is measured and compared with simulations. Discrepancies in results are associated with surface roughness which is analyzed by a scanning probe microscope and a scanning electron microscope.

By down-scaling the developed THz antenna, a low-profile high-gain antenna for Ka-band space applications is designed. The presented antenna achieves better results than state-of-art CubeSat antennas. The antenna performance is verified by a prototype to be operated at 9 GHz, and the radiation characteristics are experimentally confirmed.

KEYWORDS

THz antenna arrays, microfabrication, micromachining, corporate-feed arrays, beam steering, high-gain antennas, circularly polarized antennas, antennas for space applications, thin metal modeling, THz antenna modeling, thin gold modeling.

ABSTRAKT

Disertační práce je zaměřena na výzkum terahertzových anténních polí optimalizovaných pro komunikaci. Pozornost je věnována korektnímu modelování kovových povrchů na terahertzových frekvencích, správné charakterizaci vodivosti zlata, vztahu vodivosti k Drudeovu modelu a souvisejícím měřením. Dále jsou v práci podrobně popsány metody vhodné pro modelování tenkých kovových vrstev (v závislosti na hloubce vniku vztažené k tloušťce vrstvy).

V práci je navržen prvek terahertzového anténního pole. Prvek sestává ze 2×2 zářičů a je optimalizován pro komunikaci. Prvek byl vyvinut tak, aby umožňoval modulární realizaci větších anténních polí. Princip rozšíření je demonstrován na anténním poli sestávajícím ze 4×4 zářičů; toto pole je v práci podrobně popsáno. Anténní pole dosahuje lepších parametrů než stávající anténní systémy. Popisované antény vyzařují na terahertzových frekvencích kruhově polarizovanou vlnu, jsou širokopásmové, mají vysoký zisk a kompaktní rozměry.

V práci je rovněž popsáno anténní pole sestávající z 8×8 zářičů, které umožňuje řízení vyzařovacího diagramu. Hlavní lalok anténního pole lze ovládat ve dvou rozměrech. Tímto způsobem lze dosáhnout vysokého zisku antény při vyzařování kruhově polarizované vlny.

V práci jsou porovnávány různé přístupy k modelování antén s tenkými kovovými vrstvami. S ohledem na různé požadavky je diskutován výběr nejvhodnější metody.

Navržená anténní pole sestávající ze 2×2 a 4×4 zářičů byly vyrobeny technologií micro-fabrication. Každý krok výroby je v práci podrobně popsán a diskutován. Na vstupu antén byl změřen kmitočtový průběh činitele odrazu a byl porovnán se simulacemi. Odchyly mezi výsledky byly způsobeny drsností povrchu. Drsnost byla analyzována mikroskopem se skenovací sondou a skenovacím elektronovým mikroskopem.

Přepočítáním vyvinuté terahertzové antény do pásma Ka byla navržena anténa s nízkým profilem s vysokým ziskem, která je vhodná pro kosmické aplikace. Popsaná anténa dosahuje lepších parametrů než stávající CubeSat antény. Parametry antény byly ověřeny na prototypu, který byl optimalizován pro práci na kmitočtu 9 GHz. Experimentálně byly ověřeny impedanční i vyzařovací charakteristiky antény.

Terahertzové anténní pole, micro-fabrication, mikro-obrábění, anténní pole s uzavřenou napájecí sítí, řízení směrových charakteristik, anténa s vysokým ziskem, kruhově polarizovaná anténa, anténa pro kosmické aplikace, modelování tenkých kovových vrstev, modelování terahertzových antén, modelování vrstev tenkých zlata..

KLÍČOVÁ SLOVA

Terahertzové anténní pole, mikrovýroba, mikroobrábění, pole se sdruženým napájením, vychylování paprsku, vysokoziskové antény, kruhově polarizované antény, antény pro vesmírné aplikace, modelování tenkých kovových vrstev, modelování terahertzových antén, modelování tenkých zlatých vrstev

BIBLIOGRAFICKÁ CITACE

WARMOWSKA, D., *THz antenna arrays for communications*, Doctoral thesis. Brno: Brno University of Technology, Faculty of Electrical Engineering and Communication, Department of Radio Electronics, 2020. Supervised by prof. Zbynek Raida.

DECLARATION

I declare that I have written the Doctoral Thesis titled “THz antenna arrays for communications” independently, under the guidance of the advisor and using exclusively the technical references and other sources of information cited in the thesis and listed in the comprehensive bibliography at the end of the thesis.

As the author I furthermore declare that, with respect to the creation of this Doctoral Thesis, I have not infringed any copyright or violated anyone’s personal and/or ownership rights. In this context, I am fully aware of the consequences of breaking Regulation § 11 of the Copyright Act No. 121/2000 Coll. of the Czech Republic, as amended, and of any breach of rights related to intellectual property or introduced within amendments to relevant Acts such as the Intellectual Property Act or the Criminal Code, Act No. 40/2009 Coll., Section 2, Head VI, Part 4.

Brno, the 8th of July 2020

.....

Author’s signature

ACKNOWLEDGMENT

I would like to express my gratitude to my supervisor prof. Zbyněk Raida for his guidance, patience, encouragement and kindness. I want to give a big thank you to my best colleague and great advisor Kerlos Atia Abdalamak. All the talks we had and analyses we did helped me tremendously. I want to express my appreciation of the valuable advice I got from prof. Garcia-Munoz and prof. Daniel Segovia during my stay at UC3M, I am amazed at how they explain complicated things in such simple ways, always with a positive attitude. I want to thank dr. Shihab Al-Daiffe for his advice, kindness and the possibility to work in Darmstadt clean room. I thank all my Darmstadt colleagues Veronica, Mario, Alaa, Julian, Ahid and others, you helped me and motivated me. I thank my colleagues Aslihan, Mira, Martin K., Martin M. and Honza. I want to thank Petr for his enormous help in CEITEC cleanroom. I want to thank my boyfriend Alex for his support and patience.

Last but not least I would like to thank my parents, Monika and Marek, that they raised me to never stop educating myself, to be curious about the world, appreciate the beauty in everything around me and just be a good person. Thank you.

Brno.....

.....
author's signature

ACKNOWLEDGMENT

Research described in this Doctoral Thesis has been founded by the Innovative Training Network Convergence of Electronics and Photonics Technologies for Enabling Terahertz Applications (ITN CELTA) through the H2020 under Grant 675683. The author of this dissertation was one of the Early Stage Researchers in the CELTA consortium.

Some of the measurements were performed with the support of the research infrastructure of CEITEC Nano Research Infrastructure through the Ministry of Education, Youth and Sport of the Czech Republic (MEYS CR) under Grant LM2018110.

Brno.....

.....
author's signature



TABLE OF CONTENT

Introduction.....	1
1.1 THz and sub-THz waves	1
1.1.1 THz Applications	2
1.1.2 Transmission losses at THz frequencies	3
1.2 Challenges of THz antenna fabrication	5
1.3 Circular polarization	5
1.4 Beam steering	6
1.5 Satellite Communications.....	7
1.5.1 Requirements on antennas for satellite communications systems.....	8
2 State-of-the-art.....	9
2.1 THz antennas	9
2.1.1 THz antennas for communications.....	11
2.1.2 Antennas with beam steering capabilities	12
2.2 Antennas for satellite communications.....	12
2.3 Modeling thin metallic structures at THz frequencies.....	13
2.4 Microfabrication technologies.....	13
2.4.1 Dry Etching	14
2.4.2 Bonding.....	16
3 Objectives	17
4 Modeling metal at THz frequencies	18
4.1 Permittivity and conductivity relation	18
4.1.1 Drude model.....	18
4.1.2 Gold conductivity at THz frequencies	19
4.1.3 Very thin metallic films	22
4.2 Modeling thin metal at THz frequencies	22
4.3 Summary	26
5 Corporate feed THz antenna design and modeling.....	27
5.1 Design methodology.....	27
5.1.1 Design considerations	27
5.1.2 Antenna element design	28
5.1.3 Design procedure and dimensions considerations	30
5.1.4 The 4×4 antenna array design	32
5.1.5 Simulation results.....	34
5.1.6 Comparisons with state-of-art.....	38
5.2 Modeling of the THz antenna	39
5.2.1 Different models and boundary conditions	39
5.2.2 Surface roughness and layer thickness influence on the antenna performance.....	42

5.3	Antenna array with beam steering capability	45
5.3.1	Antenna design.....	45
5.3.2	Simulation results.....	46
5.4	Summary	48
6	Fabrication technology and measurements.....	49
6.1	Manufacturing technology.....	49
6.1.1	Structures etching.....	50
6.1.2	Wafer dicing.....	51
6.1.3	Gold evaporation.....	51
6.1.4	Bonding.....	53
6.1.5	Dielectric layer manufacturing.....	54
6.1.6	Assembly of the antenna	55
6.2	Measurements.....	56
6.2.1	Reflection Coefficient Measurements.....	56
6.2.2	Surface Roughness Measurements.....	58
6.3	Summary	60
7	Low-profile antenna for space applications	61
7.1	Design of antenna array at 35 GHz	61
7.1.1	Design of a 2×2 antenna element.....	61
7.1.2	Simulation results for 2x2 antenna element	62
7.2	Prototype at 9 GHz.....	64
7.2.1	Antenna and transition design.....	64
7.2.2	Prototype manufacturing.....	65
7.2.3	Measurements	65
7.2.4	Dielectric waveguide analyses	67
7.3	The 8x8 antenna array at 35 GHz.....	69
7.3.1	Antenna design.....	69
7.3.2	Simulation results.....	70
7.3.3	Manufacturing.....	71
7.3.4	Comparisons with state of art.....	72
7.4	Summary	72
8	Conclusions.....	73
	References.....	75
	List of Figures.....	82
	List of Tables	86
	List of Publications	87
	List of symbols, physical constants and abbreviations.....	88
	Curriculum Vitae.....	90

1 INTRODUCTION

The dissertation thesis is focused on a design of circularly polarized terahertz antenna arrays for communications applications at THz frequencies. To make the thesis understandable, related topics are introduced in this chapter.

The first paragraph is conceived as an introduction to electromagnetic waves propagating at terahertz frequencies. Specific properties of those waves and their exploitation in selected applications are discussed. Attention is turned to wireless communication at terahertz frequencies and related losses.

Since in the THz range, the losses are significantly higher compared to microwave frequencies, antennas have to be designed to contribute to the compensation. Challenges of THz antenna fabrication technologies are given in the second paragraph.

Circularly polarized waves are preferred for communications, and therefore, circular polarization is discussed in the third paragraph of the Introduction.

The fourth paragraph is devoted to satellite communications technologies, the recent advancements and challenges, and requirements on antennas for satellite communications.

1.1 THZ AND SUB-THZ WAVES

The number of applications of terahertz (THz) and sub-THz waves has been dynamically increasing in the last years. The research in the field has been also contributed by the Group of Applied Electromagnetics at the Brno University of Technology (BUT). Therefore, BUT was involved in the consortium of the international training network *Convergence of Electronics and Photonics Technologies for Enabling Terahertz Applications* (CELTA).

CELTA was aimed to educate the next generation of researchers who enable Europe to take a leading role in the multidisciplinary area of terahertz technology. CELTA comprised both fundamentals and applications involving components and complete systems for sensing, instrumentation, imaging, spectroscopy, and communications. All the researched technologies are keys to deal with challenges and create solutions in a large number of focus areas of the Horizon 2020 program.

Terahertz (THz) radiation is an electromagnetic radiation in the spectrum of frequencies ranging from 0.1 THz to 10 THz which correspond to wavelengths from 3 mm to 30 μm . Waves within the lower range of the THz band, 100 GHz – 300 GHz, can sometimes be referred to as sub-THz waves.

The position of the THz band in the electromagnetic spectrum is shown in Figure 1. The THz band is still not well explored, when compared to relatively well-developed science and technology in the microwave and optical parts of the electromagnetic spectrum. Due to difficulties in producing THz sources and detectors, the term "terahertz gap" is used

to describe this frequency range. However, this technological gap has been changing now, since much more research has been done in the THz field. The recent increased interest in THz range has been driven by the properties of THz waves and by a wide range of potential applications [1].

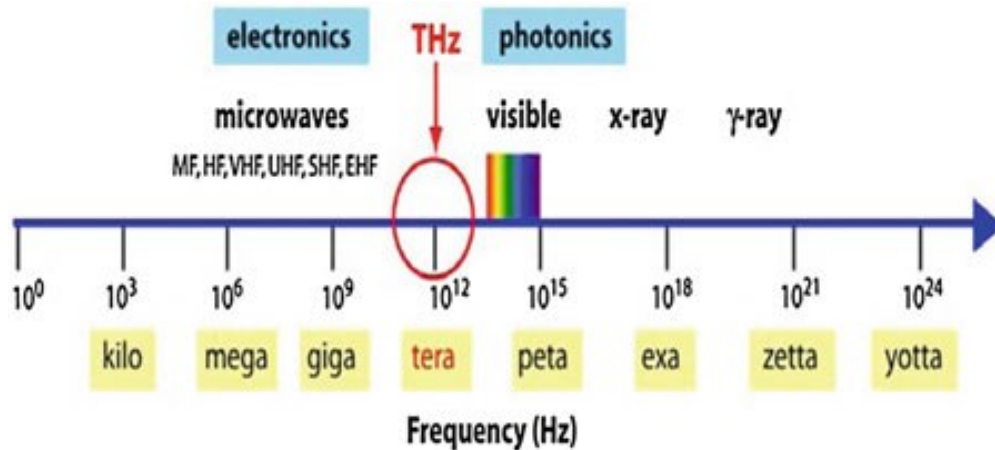


Figure 1. Position of the THz band in the electromagnetic spectrum [1].

The THz radiation has many interesting properties which differ from other waves in the electromagnetic spectrum, for example [1],[2]:

- **Penetration.** Water, metal, and dielectric exhibit a different penetration of THz waves. Water, as a strongly polar liquid, exhibits highly absorptive behavior in the THz region. Metals, on the other hand, are highly reflective at THz frequencies because of their high electrical conductivity. Finally, dielectrics are usually opaque at optical frequencies but transparent at THz ones.
- **High-resolution images.** THz wavelengths are much shorter than microwave ones, and therefore THz waves can be used to provide images with a very high resolution in the range of sub-millimeters.
- **Spectroscopy.** Most solid materials exhibit characteristic spectral features in the frequency range from 0.5 THz to 3 THz range. These spectral features allow the detection of many different substances, even when sealed in a package or being hidden behind clothes.
- **Non-ionizing radiation.** THz radiation is non-ionizing and can be used with very low power levels (μW) thanks to a very low photon energy. This characteristic makes THz waves very suitable for medical and biological applications.
- **High intensity.** Focusing and collimating THz waves is much easier than microwave ones. Hence, higher intensities can be achieved.
- **Unlicensed band.** Currently, frequency bands are licensed up to 250 GHz. Higher bands are license-free.

1.1.1 THz Applications

The presented characteristics of THz waves differ from waves in different ranges of the

electromagnetic spectrum. Thanks to the unique features, there are many applications which exploit devices and systems operating in the THz range:

- **Communications.** In recent years, the demands for high data rates and wide bandwidth of wireless communication have dramatically increased. In order to achieve high data rates of 10 to 20 Gbit/s, the carrier frequencies in the millimeter or sub-millimeter wavelengths range are necessary to be used. The attenuation at THz frequencies is high, but there are several bands that could be used for high-data-rate wireless communication.
- **Medical Imaging.** Water has a high absorption in the THz spectrum. Therefore, hydrate objects exhibit a strong contrast in comparison with surrounding materials. The THz radiation is quite gentle to the human body due to the high water absorption, and THz waves cannot penetrate into the human body. These characteristics offer a big opportunity for the THz technology to make an impact on the medical applications. THz waves can be used to precisely detect the margins of the cancer tissue. THz imaging provides a good contrast between different types of tissue, due to the possibility of recognition of spectral fingerprints. Therefore, the THz waves can be used to detect cancer, characterize burn injuries or tooth decay [2],[3].
- **Non-destructive testing.** THz waves easily penetrate a paper or a plastic which are often used as packaging materials. This allows to characterize different packages and objects without damaging them. THz waves can also help in the art conservation. Due to THz characteristics, we can analyze different layers of substances the painting was covered in order to conserve it better. This is also applicable for different kinds of old books and manuscripts, where removing the cover could possibly damage the document.
- **Security.** Penetration through clothes provides many options of the detection of weapons, explosives, chemical and biological agents. Thanks to this feature, THz imaging systems can be used at the airports for a fast scan at the security check to detect hidden objects carried by people, or in their luggage.

From all the applications mentioned above, many of them are being currently exploited (for example, airport security scans, THz-imaging, and spectroscopy). The most interesting application is the communications, as the THz band delivers an abundance of bandwidth which would enable sending large amounts of data. Current demand on data transfers is constantly rapidly increasing, and high-performance THz antennas are necessary. Therefore, this work focuses on developing THz antennas for communication systems.

1.1.2 Transmission losses at THz frequencies

Although the THz waves have a lot of interesting and useful characteristics, there are some challenges in exploiting this part of the electromagnetic spectrum. There are three types of losses related to an electromagnetic wave transmission [4].

First, the strong atmospheric attenuation occurs at THz frequencies. In Figure 2, the atmospheric attenuation is presented as a function of frequency. Evidently, the

attenuation is very high at certain frequencies within the THz range. This should be taken into consideration if the THz system will be used on Earth or for Earth-space communications [1].

Second, the free space path loss (FSPL) is the source of losses in the THz region. These type of losses is strictly related to the frequency of operation. The higher the frequency, the higher the losses [5]:

$$FSPL = \frac{4\pi df}{c} \quad (1)$$

Here, d is the distance between the transmitter and the receiver, f denotes the operation frequency and c is the velocity of light.

Lastly, high losses in the THz region are related to the non-line of sight propagation. This propagation occurs when there are objects in the Fresnel zone of the communicating antennas. The influences of the objects in the Fresnel zone can be even higher in the THz region because the THz waves react differently with materials than microwaves. For example, the water absorption is much higher.

Since the losses in the THz region are higher than losses at lower frequencies, THz antenna designs need to contribute to their compensation. Hence, the antennas should provide a high gain and very directive radiation characteristics. Moreover, the distances on which the communication systems are operating have to be much smaller than for low-frequency systems.

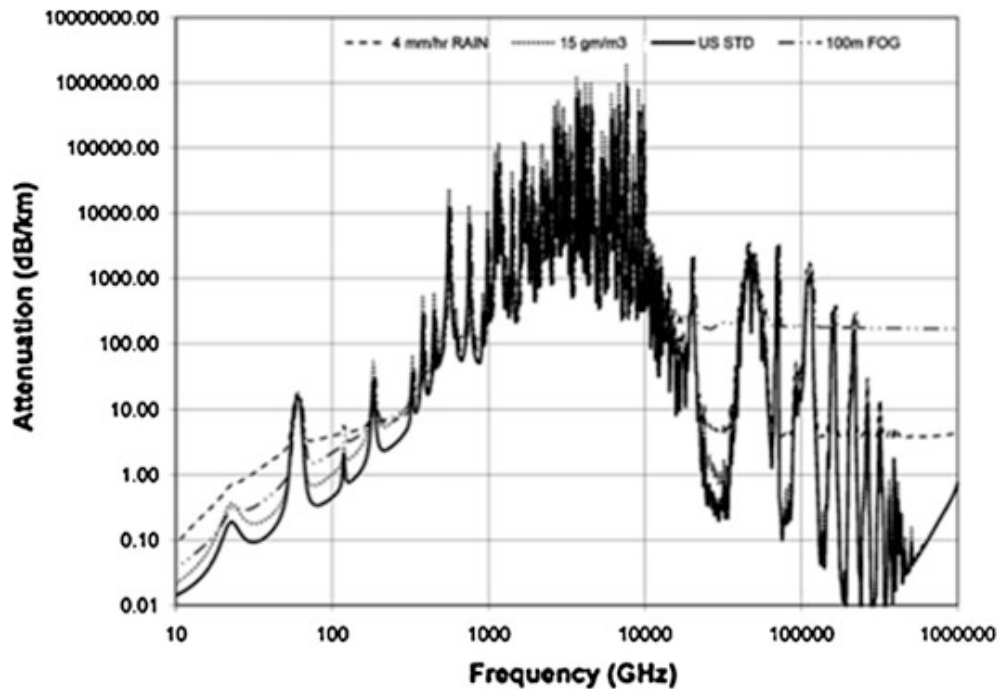


Figure 2. Atmospheric attenuation in THz and infrared range of the electromagnetic spectrum [1].

1.2 CHALLENGES OF THz ANTENNA FABRICATION

The design and manufacturing of antennas to be operated at THz frequencies brings a lot of technological challenges. In case of the popular technology of manufacturing metallic antennas on a dielectric substrate, the thickness of the substrate is often comparable to the wavelength at THz frequencies. This makes the substrate very thick and its effect has to be taken into account. With a thick substrate, rays at certain angles become completely reflected and trapped within the substrate as a surface wave [6]. A substrate with a small thickness and low dielectric permittivity can solve the problem in a lower part of the THz spectrum, but such thin substrates do not exist or are very expensive for higher frequencies. Surface wave effects can be reduced by exploiting lenses. Thanks to lenses, rays impinge nearly from a normal direction to the surface and do not suffer from the total internal reflection.

Very small sizes of transmission lines are another problem of the microstrip technology. Hence, the manufacturing is highly problematic or even impossible at higher THz frequencies. This issue can be solved by the use of feeding based on waveguides and by the exploitation of slots for the excitation of the antenna structure. Lastly, the accuracy of the printed circuit board (PCB) technology is a big problem and makes the fabrication impossible for most of the cases.

The lack of a proper characterization of the substrates is another problem with the designs at THz frequencies. Most of the popular microwave substrates are characterized up to 10 GHz. Permittivity of materials decreases with frequency, and the exact value has to be known for a precise design [7]. Some substrates have been characterized, but still many substrates are not completely described in the THz range [8]. Considering all of these disadvantages, the PCB based technologies are usually not employed at THz frequencies. However, there are some THz antennas implemented by these technologies.

Therefore, new fabrication technologies are required. When operating at such short wavelengths, devices become very small, and also the sensitivity is increased. High accuracy and high precision of the fabrication process, usually at the level of micrometers or nanometers, is therefore necessary. Silicon micro- and nano-fabrication is commonly used for the manufacturing of the THz antennas. The technology provides excellent results in terms of accuracy and tolerances, but is not well-accessible (only a limited number of cleanrooms in the world). The prices can be very high because of the need for the state-of-art machines and highly trained staff to operate them.

The existence of the so-called “THz-Gap” is another drawback. The THz band lies between the microwave band and the infrared band. There are sources available in those bands but cannot be used in the THz range directly. From the microwave side, fabricating solid-state sources at the THz frequencies is difficult because of a very small size which is related to a small available power. From the optical side, conventional lasers are not available in the THz range because suitable semiconductors do not exist.

1.3 CIRCULAR POLARIZATION

An antenna radiates an ideally circularly polarized wave when the horizontal component of the radiated field is identical to the vertical one. In case of realistic antennas, the

magnitude of the components differs, and we talk about circular polarization when the ratio of the horizontal and vertical components is between 1 and 2 (in the decibel scale, from 0 dB to 3 dB). This ratio is referred to as the axial ratio of the circular polarization. Circular polarization can be right-handed or left-handed depending on the direction of the rotation of the electric field vector of the radiated wave.

One of the biggest advantages of the circularly polarized antennas is that they do not require alignment of the transmitting and the receiving antenna. This is not the case for linearly polarized antennas, where two linearly polarized antennas always should be positioned parallel to each other in order to avoid polarization mismatch losses. Moreover, circularly polarized antennas can operate well with linearly polarized ones and only half of the power is lost, for both the vertical and the horizontal linear polarization. Moreover, circularly polarized links benefit from resilience to multipath reflections in different environments as well as other propagation effects dependent on polarization such as Faraday rotation [9] and reduction of rain clutter [10].

Considering these advantages, circularly polarized antennas are preferred in communications systems to avoid unnecessary losses added to the transmission losses in the THz region. Circularly polarized antennas are widely employed in many different applications such as terrestrial communication systems, satellite communication systems, radars [11] and others.

In order to design an antenna that radiates circularly polarized waves, an adequate structure of the radiating element has to be chosen. Different shapes, with a single point feed were exploited, however, these types of antennas radiate circularly polarized waves in a narrow bandwidth; the axial ratio bandwidth is narrow. The narrow axial ratio bandwidth is a common problem for many circularly polarized antennas. This limits the frequency bandwidth in which the antenna can operate, furthermore it is a restraining factor for the possible applications.

For the reasons mentioned above, the axial ratio enhancement techniques have been an interesting subject for many researchers. In [12], a much wider axial ratio bandwidth of the antenna was obtained when a double feed was chosen. For a circularly polarized microstrip antenna, the axial ratio bandwidth can be further enlarged by choosing multiple feeds. By combining multiple antenna elements, each fed separately, with a phase shift on each of the feeds, a sequential rotation technique can be obtained [13]. Thanks to this technique, wide axial ratios are attainable [14]. However, a complicated design of the feeding network the disadvantage [15].

1.4 BEAM STEERING

As it was already stated, at THz frequencies the channel losses are considerably higher than at the microwave range. One of the solutions to those losses is beam forming which is related to employment of antennas with highly directive and narrow beams.

Moreover, in order to localize and communicate with the mobile terminals, beam steering is necessary. By choosing the proper direction of radiation, the unwanted signals can be avoided for the receiving antenna and in case of transmitting antenna the beam can be steered in the direction of the receiving terminal. Currently, the most popular solution to

achieve beam steering is implementing active phase shifters in the antenna feeding. This type of phase shifters supplies wide range of the available phase shift and fast switching times. However, the complexity is high which is related to high digital demand, large size as well as increased temperature of the devices [4].

Passive phase shifters offer interesting characteristics [16]–[18] without the disadvantages that the active ones hold [4]. In [19] authors present a phase shifter, operating at 75 – 500 GHz, based on carbon nanotubes placed on a dielectric rod waveguide (DRW), that can be incorporated into a metallic waveguide. By changing the intensity of light applied to the carbon nanotubes the dielectric constant of the DRW changes, which affects the phase of the signal that is transmitted in the waveguide.

In [20] a phase shifter based on liquid crystal placed inside a DRW is presented, the bias voltage around the DRW changes the dielectric constant of the carbon nanotubes which influence the phase of the transmitted signal in the range of 0° - 900° .

1.5 SATELLITE COMMUNICATIONS

Satellite Communications (SatComs) are going through a large transformation nowadays intending to refocus on broadband data services. The transformation is aimed to increase [21]:

- The volume of the media streaming so that big amounts of data can be transmitted.
- To increase the broadband coverage to underserved areas such as developing countries or remote, rural areas.

Before, only a limited number of organizations were involved in the SatComs industry. Recently, many private ventures have been included [21]. In January 2020, SpaceX has deployed 242 satellites to construct its Starlink constellation, intending to reach nearly 12 000 satellites by mid-2020 [22]. With new investments, the SatComs technologies are developing rapidly and the industry is rapidly growing.

Currently, SatComs operate mainly in L, S and C bands. Applications such as GPS, Galileo, weather and ship radars, SatComs, space research, space operation, EO satellite services, TV broadcasting are all using the spectrum within the L, S and C bands [21]. Those bands spread across 1 to 8 GHz, and altogether provide only 7 GHz bandwidth. Therefore, the existing frequency bands become congested. Bandwidth is abundant in the higher frequencies ranges and the transition of the satellite technologies to those bands is unenviable. Hence, new communication systems, including antennas, with excellent parameters, operating at the K and Ka bands are necessary. The satellite spectrum with the most exploited bands L, S, and C and future bands K, Ka, and Q/V is presented in Figure 3 [21].

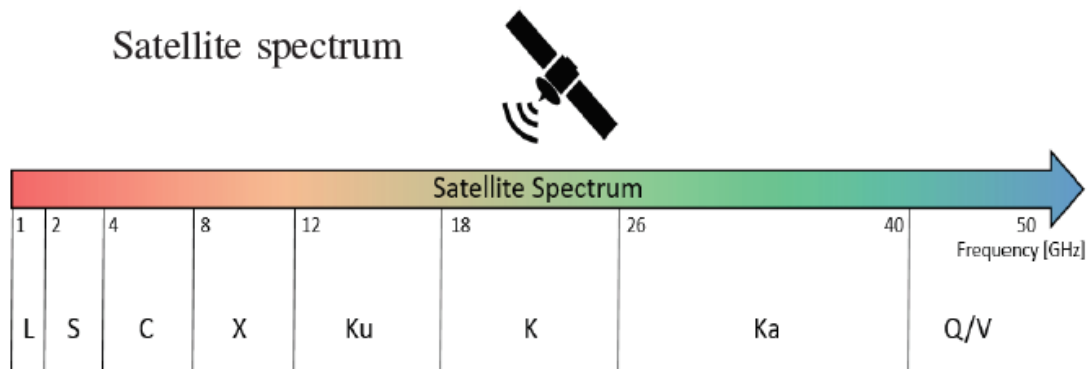


Figure 3. Satellite spectrum [21].

1.5.1 Requirements on antennas for satellite communications systems

Systems operating in space have high requirements on the design, because they need to survive in a very harsh environment. The temperature in space can be even -150°C , however during the launch the elements need to withstand the temperature of even 150°C and the shock of being accelerated to $28,100 \text{ km/h}$. The elements of the satellite are also subject to radiation and need to survive in space for at least 20 years without any need for repairs. Moreover, the size of the communication systems should be small and the weight should be light because the costs of launching every gram to space is high. Considering an antenna design for space, antenna systems should have high gain, directive radiation characteristics with a narrow main lobe, and low side lobe levels.

Currently, the most popular antenna architectures are reflector antennas fed by horns. The large size of the reflector enables to increase the gain significantly and allows the beams to be more focused, however it also introduces issues [21]. Such a large reflector is bulky and cannot be mounted on a satellite, therefore deployable reflectors were introduced. Such an antenna has the large reflector confined, so it takes very little space, and when the satellite is already on the orbit, the reflector opens. This technology eliminates some issues, however, the deployment can be problematic as some mechanical issues can occur.

Antennas are requested to transmit and receive circularly polarized waves, since the mutual orientation of the transmit antenna and the receive one varies. Moreover, the wave polarization can be rotated by the atmosphere.

2 STATE-OF-THE-ART

The content of this chapter is a brief introduction to THz antennas and THz antennas designed for communications. Next, designs of antennas for satellite communications are presented. The following paragraph is devoted to the modeling of thin metallic structures at THz frequencies. In the last paragraph, the advances in microfabrication technologies are given.

2.1 THZ ANTENNAS

For the operation at THz frequencies, three types of antenna geometries are dominantly used – log-spiral and log-periodic antennas, bow-tie dipoles, and horn antennas.

Log-spiral antennas (Figure 4a) are circularly polarized and provide a relatively constant input impedance. These antennas have almost constant radiation pattern and operate in very wide bandwidths. Unfortunately, these antennas are not able to obtain very high gains. An example of such an antenna can be found in [23]. The antenna has a bandwidth from 30 GHz to 5.2 THz, and the gain is 1 dB, approximately.

Log-periodic antennas (Figure 4b) do not hold a constant impedance and polarization when the frequency changes. Also, their radiation efficiency decreases for higher frequencies of operation and the achieved gain is low. However, log-periodic antennas have a convenient radiation pattern and can obtain high directivity over a wide bandwidth. This antenna topology is very popular in the THz region [24]–[26].

The shape of the **bow-tie antenna** (Figure 4c) is similar to a dipole with the arms widening from the middle to the end. The bow tie is also of a self-complementary topology and provides the most constant impedance at the input compared to the log-spiral and log-periodic antennas. However, its radiation pattern gets worse with increasing frequency. An example of a bow-tie antenna was presented in [27].

None of the log-spiral, log-periodic, and bow-tie antennas can achieve directional radiation patterns. For this reason, those antennas are usually completed by a lens to focus the beam into a desired direction. That way, the radiation becomes more directive. Unfortunately, lenses have a very large size and their behavior is hard to model. Moreover, the design of lenses is complex and time-consuming and the manufacturing can be very expensive [28].

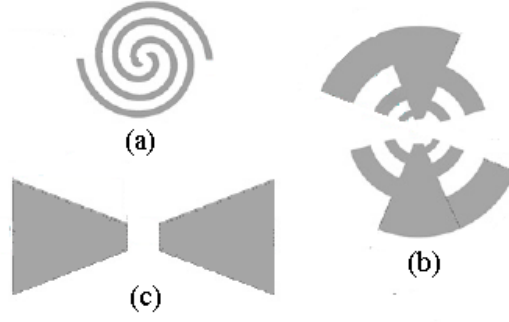


Figure 4. Typical geometries of THz antenna elements:
a) log-spiral antenna, b) log-periodic antenna, c) bow-tie antenna.

Horn antennas are very popular in the THz region due to very high gains and directive radiation patterns [28], [29]. Horns are usually made of metal and their manufacturing can be very expensive, even at low frequencies, because of the shape. The size and the height of horn antennas are comparable to the wavelength of operation, and their integration into modern systems might be problematic. The relation between the size, the height and the directivity of the horn antenna is shown in Figure 5 [30], in the lower part of the figure the geometry of the antenna is presented.

In [29] authors, present a horn antenna that achieves a gain of 23 dBi, operating at 495 GHz with a large height of $30 \lambda_0$. Moreover, it is difficult to implement an antenna array made out of horns. Because of their large size, the distance between the radiating elements is large, and this negatively influences the array radiation characteristics.

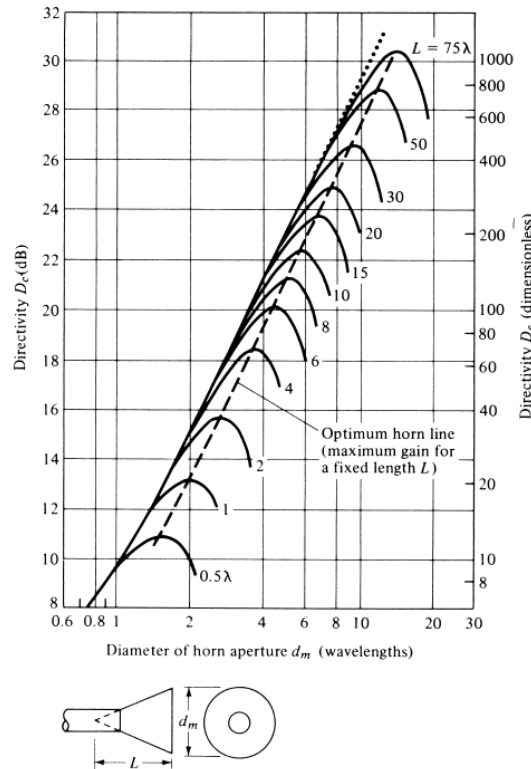


Figure 5. Directivity of horn antenna with different aperture diameter and antenna height [30].

2.1.1 THz antennas for communications

To establish communication links at THz frequencies, antennas with directive radiation characteristics, high-gain, circular polarization, and wide bandwidths are necessary. Aspects as low-profile, easy integration into modern systems, low-cost manufacturing, and the possibility to group elements into an antenna array are also important factors.

There are many designs of high-gain, circularly polarized antennas to be operated in the mm-wave bands. Upscaling mm-wave designs to THz frequencies is one of the design strategies.

Fabry-Perot antennas [31]–[33] antennas can radiate circularly polarized signals, have a low profile, and, thanks to a large number of radiating elements, can achieve high gains. However, their bandwidths are very limited (1-3%) and the design proves to be very problematic to be scaled to THz frequencies, mostly due to fabrication limitations.

In case of **spiral antennas**, radiation characteristics have to be converted to unidirectional ones which can be performed by techniques using:

- Cavities/absorbers. However, the losses are significantly increased [34].
- Conical shapes. However, the fabrication processes can prove to be very tricky and expensive at such high frequencies. To the best of the author's knowledge, the highest obtained frequency by an actual manufactured prototype is 14 GHz [35].

Lens antennas can overcome all the previous challenges by placing spiral (or other planar antennas) on a dielectric lens. However, these lenses should be electrically large in order of $10\lambda_0$ [36].

Dielectric rod waveguide antennas achieve excellent gains and bandwidths. However, they have an electrically large height [37]–[40]. A similar issue occurs for the horn antennas that were discussed before.

The large size of the lens, horn, and dielectric rod antennas can make it problematic to integrate them into modern communication systems. Therefore, a compact high gain and circularly polarized solution with a straight-forward manufacturing process is necessary.

On the other hand, **corporate feed antennas** can be integrated into the system easily. These types of antennas usually include multiple layers comprising radiating elements (slots or patches) and feeding networks which excite radiating elements. Even though these antenna structures consist of many layers, the profile of corporate feed arrays is very low, as all the layers have a small height. By increasing the number of radiating elements in the array, the gain is increased, the radiation pattern becomes more directive, and the bandwidth is enhanced [41]. Therefore, corporate feed arrays are a promising solution for creating a high gain, wide bandwidth THz antennas.

In [42], the authors presented multilayered 2×2 and 4×4 arrays. The antennas were designed and manufactured to operate at 1 THz. One of the manufacturing steps included a spin coating by a photoresist of the thickness of $\lambda/4$, which is very thick at lower THz frequencies, and therefore problematic to manufacture. The presented design was compact and wideband, however, the gain was limited to 10 dBi (the 2×2 array) and 14 dBi (the 4×4 array). Moreover, the antennas did not provide circular polarization.

In [43], the authors presented a larger array with a similar design to be operated at 350 GHz. Also, a silicon-based manufacturing process was included, and the antenna achieved a higher gain. However, the antenna [43] was again designed for linear polarization and had an electrically large height.

Another antenna with slot radiators and the corporate feed was presented in [44]. The antenna operated at 60 GHz, showed high-gain and radiated circularly polarized waves. Nevertheless, the bandwidth was only 4% and the design with multiple thin layers is not feasible to be implemented at THz frequencies.

2.1.2 Antennas with beam steering capabilities

One of the conventional ways in order to achieve beam steering in the required direction is the mechanically move the antenna. This solution is employed in radar systems, however it is not suitable for modern communications applications, because of high time consumption, latency requirements and large sizes.

Frequency scanning antennas, do not require the use of phase shifters or mechanical steering and can achieve high range of steering angles. Many implementations of frequency scanning antennas at THz frequencies have been presented [45]–[47]. However in such solutions the beam steering is never obtained at single frequency, the beam direction changes with the varying frequency. In the modern communication system this would occupy too wide bandwidths for one system and is not acceptable. A solution more compact and faster than mechanical steering and one that can steer the beam without changing frequency is to include phase shifters in the feeding system.

Currently, antennas with active phase shifters are widely used because of their impressive parameters. THz antennas with beam steering implemented by active phase shifters were presented in [48], [49]. However these phase shifters have high digital demands and complexity which has a direct influence on their cost and size [21].

In [20] authors present a dielectric rod antenna array with liquid crystal phase shifters that allow beam reconfigurability. However, the antenna operates only at 100 GHz and can steer the beam into three different directions. Another antenna employing liquid crystal phase shifters in a Fabry-Perot cavity was described in [50]. The antenna operates at 1 THz, however the beam cannot be continuously steered. Presented THz beam steering antennas offer interesting characteristics, however none of them has the ability to continuously steer the beam, has high gain and operates with circular polarization.

2.2 ANTENNAS FOR SATELLITE COMMUNICATIONS

Currently, the SatComs research is focused on improving the capabilities of the communication links to increase the data rates and deliver coverage to underserved areas [21]. To achieve that, an antenna design with high gain and wide bandwidth is necessary. The main challenges for the antenna designers are to improve the gain and bandwidth while fitting within the size, power, and weight limits for Satellite Communications.

One of the most common solutions for high-gain space missions antennas are deployable

reflector antennas [51]. Although they enable the multiple-frequency operation with high efficiency and high gain, they still require high mechanical complexity due to their deployment. In [52], an inflatable antenna was presented, which also provides high gain, but the bandwidth is achieved in Ka-band is only 0.5%. Additionally, it has a complex structure as it needs to be filled with gas.

As another solution, the authors presented in [53] is a Ka-band helical antenna. However, it has a gain of only 21 dBi and of $25 \lambda_0$.

A metallic antenna with a high-gain and wide bandwidth was presented in [54], it achieves pick gain of 26 dBi with the size of $7 \times 7 \lambda_0$. An advantage of such antenna is a lack of an unreliable deployment or inflation mechanism.

2.3 MODELING THIN METALLIC STRUCTURES AT THZ FREQUENCIES

Upscaling millimeter-wave systems to terahertz frequencies requires a proper characterization of used materials (metal conductors and dielectric layers in case of passive components). In the terahertz region, dielectric permittivity and electric conductivity of metallic materials varies with frequency [55], [56]. Those frequency variations have to be carefully incorporated into precise numerical models of passive terahertz structures. A proper way of modeling has to be selected to achieve appropriate results.

There are many commercial solvers available and each of them has several different methods that can be used to model a thin metallic layer. In this thesis, a suitable method based on the relation of the skin depth to the layer thickness is presented.

2.4 MICROFABRICATION TECHNOLOGIES

In recent years micromachining technologies are becoming more popular for high-frequency antenna manufacture. These technologies can provide very high accuracy and high precision even when the manufacturing structures are the size of single micrometers. Micromachining is a technology that has been widely used for fabrications of MEMS components [57]. One of the most mature micromachining technologies is silicon micromachining [58]. In this technology, structures are etched in silicon, for such etching metallic masks are often necessary, therefore photolithography and wet metal etching are used. Etched silicon structures can be metalized when necessary by evaporation or metal sputtering. Micromachining allows to create multilayer structures simply by fabrication of many layers and bonding them together in the final step. Silicon one of the most popular material to build such structures [43], [46], [59] however Gallium Arsenide is also employed [60], even devices where the structure is entirely built by photoresist were presented [42].

Silicon technologies provide high precision and accuracy. Thanks to the technology being very advanced, it is possible to manufacture very small structures with the precision of micrometers or even nanometers. The drawback of silicon technologies is the costs of different processes and materials which can be high. Moreover, a well-

equipped cleanroom and well-trained staff have to be available, which can make the manufacture to be quite pricey. There are still not many cleanrooms in Europe than can provide micromachining possibilities.

There is a number of design constraints that occur during manufacture, which is related to the fact that every process has its constraints. The choice of the material defines the available technologies and puts constraints. Silicon is a popular choice because of a number of advantages such as well-developed technologies, a wide choice of sizes, thicknesses and other parameters of the wafers and low price.

Two manufacturing technologies enable micromachining, and thanks to them innovative antennas, detectors, sensors and other devices can be manufactured, these technologies are dry etching and bonding.

2.4.1 Dry Etching

Etching allows controlled removal of desired material from a substrate. Etching methods can be primarily divided into two categories: wet etching and dry etching. Wet etching is referred to as etching the substrate by a liquid chemical. Dry etching is etching the material by gases or plasmas, where the main etching mechanism can be fully chemical, fully mechanical or mix of the two [61].

Wet and dry etching methods provide quite different results, however, both of them require the use of a mask to protect the areas that are not meant to be etched and expose the areas that are to be removed. The material chosen for the mask should adhere easily to the substrate, not be affected by the etching solution, enable easy removal after the etching process is finished. Popular choices of mask materials for silicon wafers are silicon dioxide, photoresist and different metals.

Several parameters characterize the etching quality [61]:

- Etch rate – the rate at which the material is removed, it defines how fast the process works. It is important to have good control over the etching.
- Anisotropy and aspect ratio- Anisotropy defines in which direction does the etching occur. If the etching is equal in all the directions, then it is anisotropic, if the etch happens only in one direction (usually down the substrate) then it is isotropic etch. Mostly isotropic etches are desired because straight walls can be achieved. Aspect ratio defines the straightness of the walls achieved during the etching.
- Selectivity – is the ratio defining how much the mask is etched in comparison to how much the material is etched. If the selectivity is low the mask could be etched before the etching is finished which can result in etching the parts of the material that should not be etched.
- Etch rate uniformity – how uniform is the etch rate all over the wafer. With low uniformity the areas in the middle of the wafer could be etched much faster than the material on the outer areas of the wafer.
- Surface roughness – defines how smooth the inside walls of the etched surface are.

In general wet etching gives high etching rates. However, for this reason, the accuracy of wet etching is usually lower, and etching is anisotropic. With dry etching it is possible to achieve isotropic etching with very low surface roughness and high selectivity, however, the etch rates are much lower so etching a thick material could take a lot of time.

One of the dry etching procedures is Reactive Ion Etching (RIE) where the surface of the material is bombarded by ions of different gases. Deep Reactive Ion Etching (DRIE) is especially useful for antenna manufacture, because almost straight vertical walls can be obtained. DRIE has the advantage of anisotropic etching thanks to passivation of the vertical walls, which protects them from etching gases. This type of etching is usually a mixed etching of chemical and mechanical etching, in chemical etching the ions bond with the material chemically and in such way parts of the material are removed, in mechanical etching the ions physically push out the parts of the unwanted material in the milling process. The results of two types of DIRE: Bosch and cryogenic processes are presented in Figure 6.

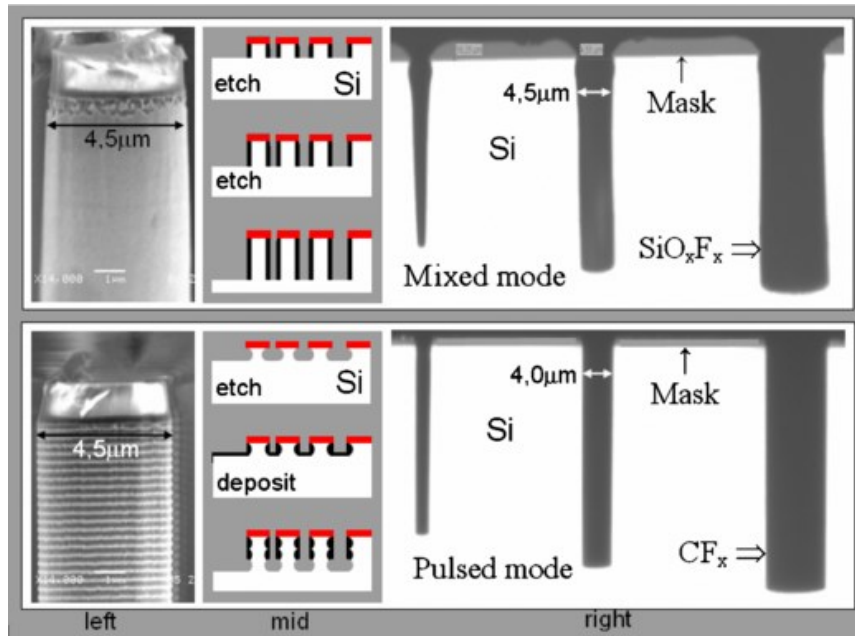


Figure 6. Comparison of results of deep reactive ion etching in mixed mode (cryogenic process) and pulsed mode (Bosch process) [62].

Cryogenic etch is one of the DRIE methods. This process is a mixed-mode etch when etching gasses and passivation gasses are released simultaneously. The etching includes the use of SF_6 and O_2 , the gases mix and SiO_xF_y grows on the walls providing passivation for them and F_x etches the silicon. This type of etching is predominantly chemical etching. The advantage of this method is that the gases used are clearer than in the Bosch method and the vertical walls are much smoother. However, in order for the passivation layer not to evaporate the process has to take place in temperature from -140°C and -85°C . Moreover, because the same gas is responsible for etching as well as passivation, the process outcomes are harder to control [63], [64].

Bosch etch is another method of DRIE. This process is a pulsed mode etch where for a short period an etching gas is released then stopped, after that a passivation gas is released for walls passivation and stopped, in such a way the process is continued until the required number of iterations is reached. SF_6 is used as an etching gas here and C_4F_8 as a passivation gas. In case of Bosch process, the etching is predominantly mechanical, based on milling. The presence of two gases where each of them is responsible for etching or passivation allows better control of the process in comparison to the cryogenic etch. Moreover, the fact that the process can be done in temperature around 15°C and does not need intensive cooling down is another advantage of this process [62].

2.4.2 Bonding

Bonding is a process of fixing two wafers together with high alignment and is usually used in the packaging of electronics. Wafer bonding can be divided into bonding with intermediate layer and direct bonding.

The mechanism of direct bonding (fusion bonding) is based on bringing two wafers together under specific pressure and temperature. This type of bonding quality is strictly related to parameters such as surface energy, surface roughness and surface morphology [61]. Direct bonding can occur thanks to the short-range forces, the dominant ones here being van der Waals forces and hydrogen bonds [65].

In case of intermediate bonding, two wafers are brought together with an intermediate layer between them, this layer can be adhesive, polymer, solder, glass frit or metal. For bonding with intermediate layer surface roughness and surface topology are not as critical [61].

Bonding is an enabling technology for micromachining. During antenna manufacture bonding tends to be used to fix together layers of a multilayer structure with good accuracy. Usually, bonding is the last step of the antenna manufacture, therefore the surface is not extremely smooth anymore, for this reason, bonding with intermediate layer is preferred.

For bonding with intermediate layer, gold is mostly employed, because it is oxidation and corrosion resistant, has low yield point and high electrical conductivity. Typically, the bonding temperature is 300°C , which is much lower than fusion bonding temperature 800°C . The typical applied pressure between two wafers is 7 MPa [61]. In [66], it was shown that by increasing the pressure, the temperature can be decreased and while decreasing the pressure, the temperature should be increased for the bonding to occur. In [67] authors presented eutectic bonding of silicon wafers with gold as an intermediate layer at the pressure of 0.8MPa, for 30 min at 400°C .

3 OBJECTIVES

The dissertation thesis is focused on a design of a **circularly polarized terahertz antenna array**. To make the design comprehensive:

- The physical behavior of metallic surfaces at THz frequencies has to be properly modeled. Hence, **comparison of modeling approaches to be used for metallic surfaces** of THz antenna arrays is the first objective.
- An **antenna suitable for communications in the THz range** should be designed. To be suitable for THz communications applications, the antenna should be circularly polarized, have high gain, wide axial ratio bandwidth and directive radiation. Developing the design methodology is the second objective.

The design methodology should comprise the possibility to extend the antenna to a bigger array. When completed by phase shifters, the array should be capable to steer the main beam. Moreover, the design technology should allow the array to be manufactured by a microfabrication technology.

- Properties of fabrication technologies have to be considered when modeling the array. Hence, technologies for manufacturing THz arrays have to be compared and **the designed antenna at THz frequencies should be manufactured by microfabrication** technologies, which is the third objective.

The best available technology is chosen, and different THz constraints and phenomena are taken into consideration. Technological aspects are considered when modeling.

- The **design procedure should be as general as possible**, which is the fourth objective. The generality of the procedure is verified by replicating the design at microwave frequencies.

The replication resulted in a circularly polarized antenna array suitable for space applications. Attention is turned to high gain, wide axial ratio bandwidth, low-profile and performance better than state-of-art antenna designs provide.

4 MODELING METAL AT THZ FREQUENCIES

Gold is frequently used for manufacturing high-frequency devices. As it was mentioned before, the benefits include high electrical conductivity, resistance to oxidation, and resistance to corrosion. Gold is often chosen for the metallization of THz antennas due to the mentioned advantages.

It is well known that metals change their dielectric permittivity and conductivity with the increase of frequency. In the optical regions, those changes are very significant. In the microwave region, variations are usually small enough to be ignored. THz waves being between those two regions are not so well described in terms of gold conductivity and permittivity changes. Gold conductivity varies not only with frequency but also with the thickness of the layer and type of the deposition process [68], [69].

When designing THz antennas, described phenomena have to be properly described and included in numerical models. Modeling issues are deeply discussed in the following paragraphs.

4.1 PERMITTIVITY AND CONDUCTIVITY RELATION

Dielectric permittivity can be described by the equation [70]:

$$\varepsilon_r(\omega) = \varepsilon_1(\omega) + i \varepsilon_2(\omega) \quad (4.1)$$

Here, ε_1 represents the real part and ε_2 represents the imaginary part of permittivity [71].

The conductivity can be described by the equation [71]:

$$\sigma = \sigma_1 - i \sigma_2, \quad (4.2)$$

where σ_1 represents the real part and σ_2 represents the imaginary part of the conductivity. The conductivity is related to the dielectric permittivity by the equation [71]:

$$\sigma = \omega \varepsilon_0 \varepsilon_2 - i (\omega \varepsilon_0 (1 - \varepsilon_1)) \quad (4.3).$$

4.1.1 Drude model

In order to calculate the conductivity of a material, the dielectric permittivity is needed. It is possible to calculate the dielectric permittivity of a material using the Drude model if plasma frequency and damping frequency of the material are known [71]:

$$\varepsilon_r(\omega) = 1 - \frac{\omega_p^2}{\omega(\omega + i\omega_d)} \quad (4.4)$$

Here, ω_p is plasma frequency. At this frequency, ε_r of the material is equal to zero, and $\omega_d = 1/\tau_d$, where τ_d represents electron relaxation time. The relaxation time τ_d parametrizes the cumulative effects of various electron scattering processes.

The Drude model depends on the plasma frequency and the damping frequency. In past times, many experiments aimed to measure the plasma and damping frequencies of gold were made [71]–[76]. The values are presented in Table 1. Due to the exploitation of different measurement methods, varying environment of measurements, and different measured gold samples (various thicknesses and deposition methods), the published conductivities differ significantly. Moreover, the used methods were not well described, hence hard to replicate.

Table 1. Values of measured plasma frequency f_p and damping frequency f_d for gold.

Ref.	Author	f_p [PHz]	f_d [THz]
[71]	Olmon	2.0382	11.37
[72]	Ordal	2.183	6.46
[73]	Blaber	2.068	4.449
[74]	Zeman	2.15	17.14
[75]	Grady	2.165	17.94
[76]	Berciaud	2.176	17.71

As mentioned before, the conductivity of gold can be calculated by the Drude model. Another way to obtain gold conductivity is a direct measurement of the dielectric permittivity and recalculating the result to conductivity with equation $\varepsilon_{r(\omega)} = \varepsilon_{1(\omega)} + i \varepsilon_{2(\omega)}$ (4.1). This was done by many researchers, but mostly in the optical region. Only two works present the dielectric in the part of the THz region, in one down to 10 THz [71] and in another down to 1 THz [72].

4.1.2 Gold conductivity at THz frequencies

The real and imaginary parts of the conductivity values calculated by the Drude model with the use of the values from the literature (see Table 1) and the values obtained through measurement of dielectric permittivity [71], [72] are presented in Figure 7 and Figure 8. The results of the analysis with parameters from [74], [75], [76] were almost identical so they were presented as one curve marked as Grady.

At frequencies below 1 THz, the real part of the conductivity is constant and the imaginary part rises linearly for all the models and measurements. At frequencies above 10 THz, both the real part and the imaginary one decrease linearly. Hence, trends are identical and absolute values have to be calibrated. The discrepancies in values of the conductivity at the lower frequencies can be observed, which are associated with different measurement methods employed and varying gold sample thicknesses.

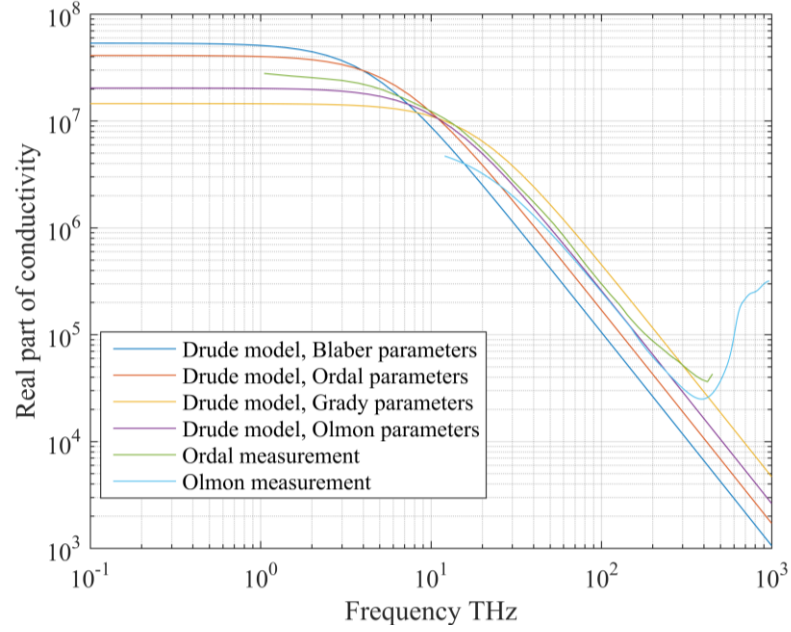


Figure 7. Frequency response of the real part of the conductivity obtained analytically and through measurement of dielectric permittivity.

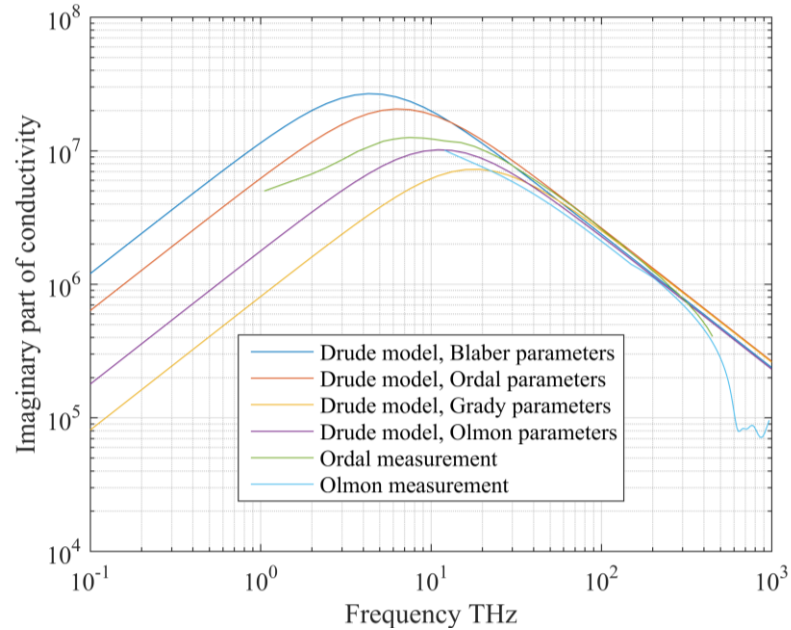


Figure 8. Frequency response of the imaginary part of the conductivity obtained analytically and through measurement of dielectric permittivity.

In order to observe the importance of using precise values of plasma frequency and damping frequency on the value of conductivity calculated by the Drude model, two tests were carried out.

In the first test, the plasma frequency was changed from 2.0382 PHz to 2.183 PHz (which correspond to the maximum and minimum measured values of plasma frequency for gold available in literature) while the damping frequency was constant $f_d = 12.5$ THz. The outcome of this test was that the real and imaginary parts of conductivity varied only by 0.01×10^7 S/m which could be considered insignificant.

In the second test, the damping frequency was varied between the values 4.449 THz to 17.94 THz (the maximum and minimum measured values of damping frequency for gold available in literature) while the plasma frequency was constant $f_p = 2.13$ PHz. The conductivity changed by even $4 \cdot 10^7$ S/m for some frequencies. The results of this analyses are presented in Figure 9 and Figure 10.

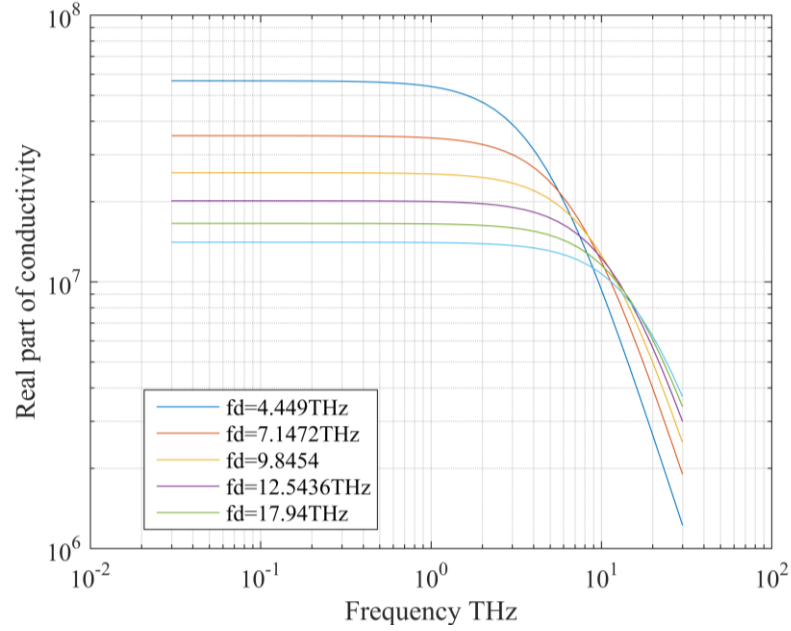


Figure 9. Frequency response of the real part of the conductivity calculated by the Drude model, $f_p=2.13$ PHz, f_d varied according to minimum and maximum values available in the literature.

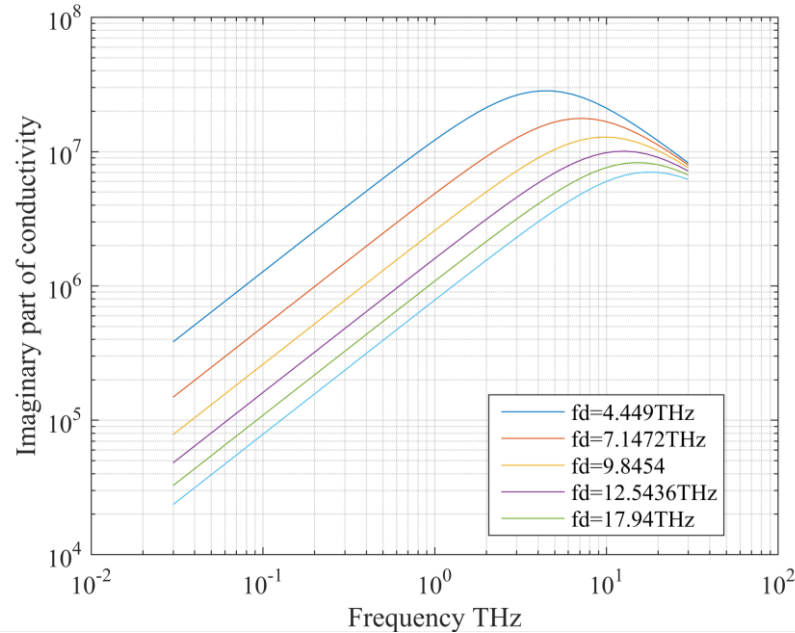


Figure 10. Frequency response of the imaginary part of the conductivity calculated by the Drude model, $f_p=2.13$ THz, f_d varied according to minimum and maximum values available in the literature.

Hence, it can be concluded that in the Drude model while calculating the conductivity choosing a proper damping frequency, from values available in literature, has a significant impact on the result, while the selection of the value of the plasma frequency does not impact the result significantly.

4.1.3 Very thin metallic films

Interesting findings about the influence of the thin gold film thickness on the conductivity were shown in [68], picture from that work is presented in Figure 11. It can be observed that the conductivity of gold, for films significantly thinner than the skin depth thickness on a given frequency, varies significantly depending on the thickness of the film and frequency of the measurement, from $0.8 \cdot 10^6$ S/m for 9 nm films on 1 THz to $4.5 \cdot 10^6$ S/m.

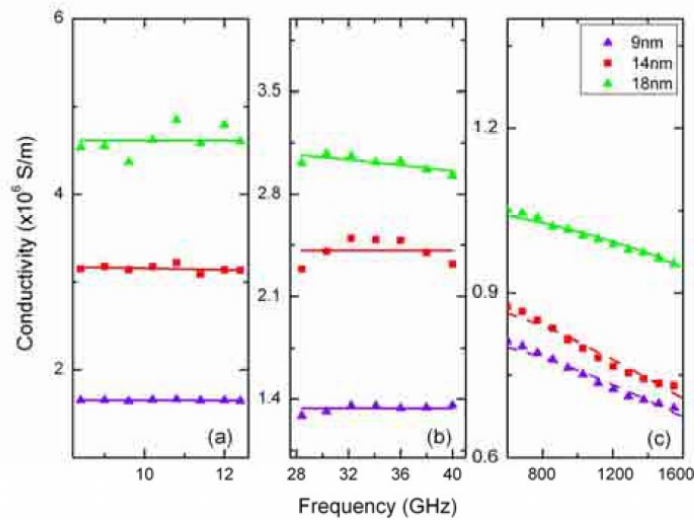


Figure 11. The real part of the conductivity of gold films at (a) X band, (b) Ka band, (c) THz frequencies. The discrete dots are experimental data; the solid lines are the fittings of the Drude model [68].

4.2 MODELING THIN METAL AT THZ FREQUENCIES

At lower frequencies, the electromagnetic field can be assumed to rapidly decay in a metal, and the metallic surface can be approximated by a perfect electric conductor with a relatively small deviation from reality.

At terahertz frequencies, behavior of metals significantly changes. The depth of electromagnetic wave penetration and the thickness of used metallization layers influences the conductivity. Such an effect has to be taken into consideration in the numerical model.

For the proper modeling of different structures with thin gold layers at THz frequencies, the relationship between the thickness of the gold layer and the conductivity is discussed in detail. Test models were created in HFSS and CST Microwave Studio.

In the case of the time-domain finite-integration technique (CST Microwave Studio):

- Default options (no additional boundary conditions were associated with a thin gold layer).

In the case of the frequency-domain finite-element technique (HFSS), different methods have been considered:

- Default options (no additional boundary conditions were associated with a thin gold layer),
- Meshing inside the gold layer,
- *Finite Conductivity* boundary was applied,
- *Layered Impedance* boundary was associated.

In addition to the two main models including the default modeling in CST and HFSS simulators, three other models were tested.

First, **HFSS with solving fields inside the metal** layer was used. This method is usually used for metals with low conductivities (lower than 0.1 MS/m). Exploiting this method forces the simulator to mesh with the utilization of tetrahedral structures and to compute the fields, even inside the conductor, for more accurate results. However, this approach subsequently increases the complexity of simulations due to a larger mesh.

The next method is using a **finite conductivity** boundary condition for the metal layer, which is a method proposed for imperfect conductors. While simulating a perfect electric conductor, all tangential electric field components are ignored. In the finite conductivity method, these components are estimated using [77]

$$E_{tan} = Z_s(\hat{n} \times H_{tan}) \quad (4.5)$$

where E_{tan} and H_{tan} are the tangential components of the electric and magnetic fields respectively, \hat{n} is the unit normal vector of the layer, and Z_s is the surface impedance of the boundary. Z_s can be calculated as [77]:

$$Z_s = (1 + j)/(\delta\sigma) \quad (4.6)$$

where δ is the skin depth and σ is the conductivity of the conductor. It is worth to mention here, that the finite conductivity boundary only approximates the behavior of the field at the surfaces of the metal without the actual calculation of fields inside it as in the previous method.

Finally, the last method – the **layered impedance** – consists of modeling the problem as a set of multiple layers starting from the first vacuum-material boundary onwards. HFSS estimates the tangential electric field components in the same way as in the previous method $E_{tan} = Z_s(\hat{n} \times H_{tan})$ (4.5) except that it calculates the impedance of the surface, based on the material properties and metal thickness as [77]:

$$Z_s^i = Z^i \frac{Z_{tran}^i}{Z^i \cosh(\gamma_i T_i) + Z_s^{i+1} \sinh(\gamma_i T_i)} \quad (4.7)$$

where γ_i is the transverse propagation constant of the i^{th} layer which has a thickness of T_i . γ_i is calculated as [77]:

$$\gamma_i = k_0 \sqrt{\mu_r^i \epsilon_{cr}^i} \quad (4.8)$$

where ϵ_{cr}^i and μ_r^i are the relative complex permittivity and permeability for the i^{th} , which are calculated as follows [77]:

$$\epsilon_{cr}^i = \epsilon_r^i - j \left(\frac{\sigma^i}{2\pi f_r \epsilon_0} + \epsilon_r^i \tan \delta_\epsilon \right) \quad (4.9)$$

$$\mu_{cr}^i = \mu_r^i - j(\mu_r^i \tan \delta_\mu) \quad (4.10)$$

Z^i and Z_{tran}^i are the intrinsic and the transfer impedances of layer i^{th} calculated as [77]:

$$Z^i = \sqrt{(\mu_0 \mu_r^i) / (\epsilon_0 \epsilon_{cr}^i)} \quad (4.11)$$

$$Z_{tran}^i = Z^i \sinh(\gamma_i T_i) + Z_s^{i+1} \cosh(\gamma_i T_i) \quad (4.12)$$

If this metal is an internal layer, the surface impedance in equation 4.7 will be equal to the average impedance estimated for both sides of the metal layer which are in contact with the computational domains.

As a proof of concept for showing the effect of different simulation models, a metallic waveguide with an internal thin metal wall was studied. Three frequencies were tested 200 GHz, 350 GHz, and 500 GHz. For the simulations, a waveguide that provides a single-mode TE_{10} performance at the frequency of interest was employed. At 350 GHz the used waveguide was WR 2.2 with dimensions of $0.570 \text{ mm} \times 0.285 \text{ mm}$.

The waveguide was terminated by a wave port to act as a matched load. An internal thin metallic wall, with the same cross-section as the waveguide, was placed in the center of the waveguide. The thickness of the gold layer varied in a range from $0.01 \text{ }\mu\text{m}$ to $10 \text{ }\mu\text{m}$. The model that was used is depicted in Figure 12.

The skin depth of gold on tested frequencies is $\delta = 175 \text{ nm}$ at 200 GHz, $\delta = 132 \text{ nm}$ at 350 GHz, and $\delta = 111 \text{ nm}$ at 500 GHz. The reflection coefficient at the terminal of the thin metallic wall was observed.

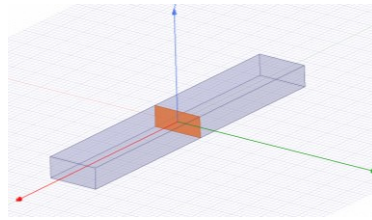


Figure 12. Model of the waveguide with a thin gold sheet inside.

For comparison purposes, the theoretical calculations of the reflection coefficient were also performed following [78] as:

$$S_{11} = \frac{(Z_L^2 - Z_w^2) \tan(\beta T)}{2Z_L Z_w + (Z_L^2 + Z_w^2) \tan(\beta T)} e^{-j\beta L_w} \quad (4.13)$$

Here, β stands for the propagation constant of the gold layer and Z_w is the characteristic impedance of the waveguide (Z_{TE} in this case) which has a length of L_w .

In Figure 14, Figure 15 and Figure 15 the reflection coefficient at the input port of the waveguide is depicted as a function of the gold-layer thickness using the previously discussed methods at testing frequencies 200 GHz, 350 GHz and 500 GHz.

It is clear here how the default HFSS and CST simulators deviate from the accurate performance in case of the metal thickness is smaller than the skin depth. This can provide a remarkable difference between simulations and measurements for THz arrays if the designers did not consider this point in their calculations. Even, finite conductivity boundary condition which is used for imperfect conductor does not provide good results for such cases, unless the conductor starts to be thick enough (metal thickness above the double of its skin depth). On the other hand, HFSS simulations with layered impedance boundary conditions and with solving inside agree well with the theoretical values. For thicknesses much higher than penetration depth, all the simulations start to convergence with similar values close to the theoretical ones.

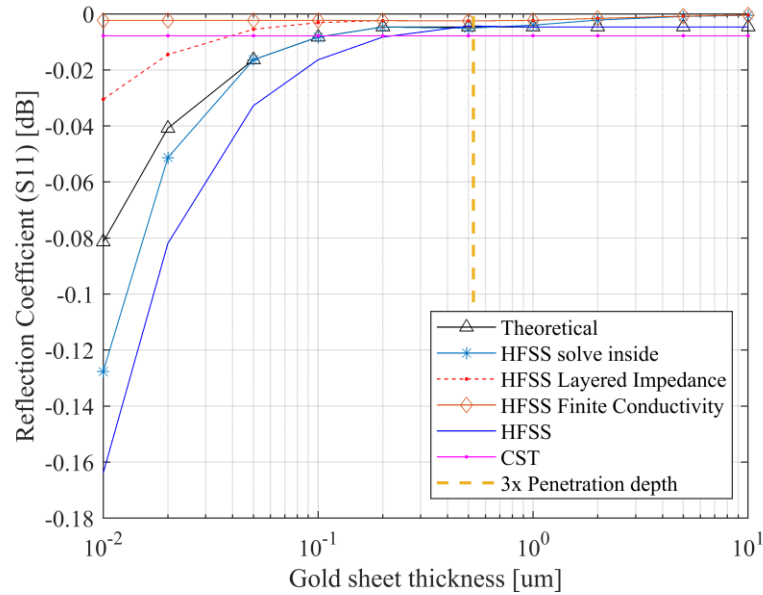


Figure 13. Reflection coefficient at the input port of waveguide as a function of the thickness of a gold wall in the cross-section at 200 GHz.

After analyzing the results at 200 GHz, 350 GHz and 500 GHz it was concluded that acceptable outputs are obtained if the gold layer thickness is:

- Lower than 3δ (HFSS layered impedance or solve inside);
- Higher than 3δ (all expect HFSS with solving inside).

Considering these conclusions, conditions at the boundary of the gold and the air can be efficiently modeled depending on the operation frequency and the thickness of the gold layer.

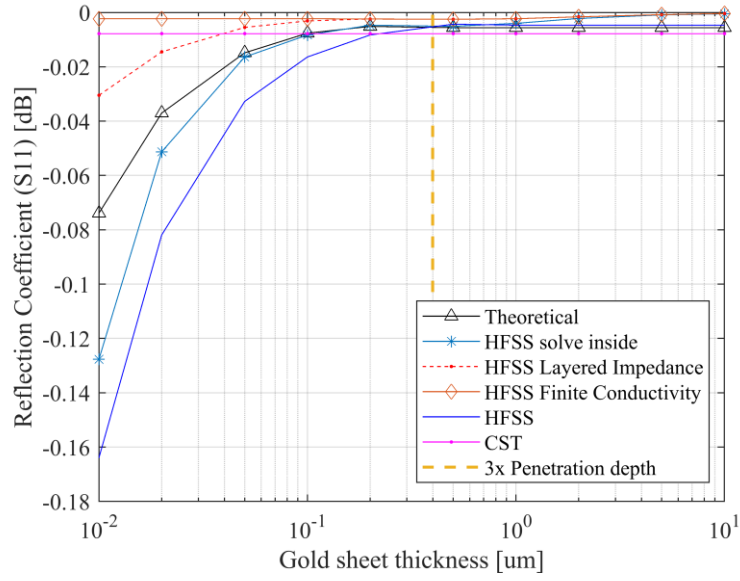


Figure 14. Reflection coefficient at the input port of waveguide as a function of the thickness of a gold wall in the cross-section at 350 GHz.

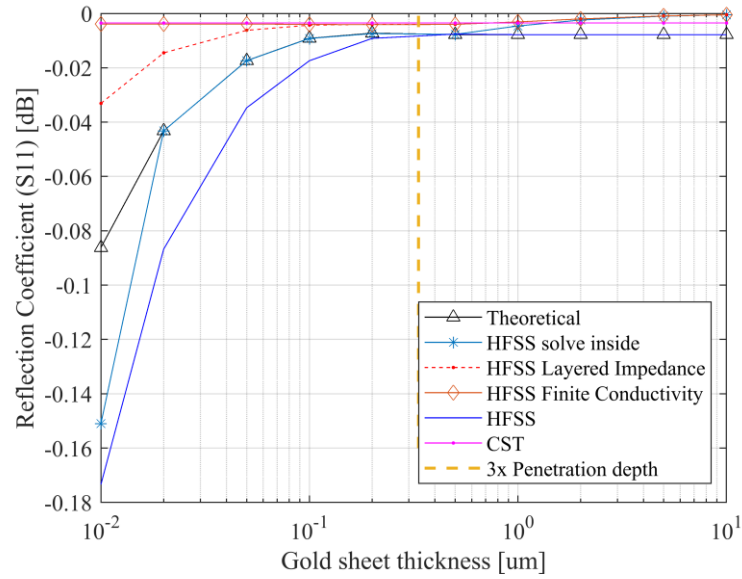


Figure 15. Reflection coefficient at the input port of waveguide as a function of the thickness of a gold wall in the cross-section at 500 GHz.

4.3 SUMMARY

Permittivity and conductivity relation is given in this chapter and the Drude model is presented. Conductivity of gold is discussed in terms of the Drude model, different measurements in THz and optical region, and layer thickness influence on conductivity.

Later, the focus was turned to the modeling of terahertz structures covered by thin metallic layers. The methods were discussed in detail. Moreover, the methods were compared and the optimum approaches were chosen depending on the thickness of the metal layer and its relation to the skin depth.

5 CORPORATE FEED THZ ANTENNA DESIGN AND MODELING

In this chapter, a design of a THz antenna array for communications is presented. The design methodology is given, including the design of the 2×2 array element and 4×4 antenna array. The simulation results of both the antennas are given and compared with state-of-the-art structures.

Models of THz antennas with thin metallic walls incorporating different boundary conditions and different material structure are analyzed and compared. The best modeling strategies are chosen. Sensitivity analyses are performed prior to fabrication.

In the last sub-chapter a beam steering capability of the designed antenna is discussed.

5.1 Design methodology

In this sub-chapter, the design considerations are discussed. Then, the design of an array element is presented. The design procedure and dimensions considerations for the 2×2 are further discussed. The array element is designed in the way that enables expansion it into a larger array, which is represented by a 4×4 array design. The simulation results of both of the antennas are presented and pre-manufacture analyses are performed. Finally, the designed antennas are compared with state-of-the-art antenna designs.

5.1.1 Design considerations

The objective of the presented design is to achieve an antenna that shows a directive radiation with a high gain, radiates circularly polarized wave, operates in wide impedance and polarization bandwidth, and works at THz frequencies. The design should enable antenna elements to be grouped into a multiple-element antenna array. Moreover, current manufacturing possibilities and constraints have to be taken into consideration.

In a simple antenna array design, a single radiating element is fed by a single feeding. This kind of design forces the array elements to have large distances between them in order to accommodate all the feeding branches below each point. Furthermore, that creates unwanted radiation characteristics such as high side lobes. Moreover, the feeding system can be very complex for large arrays of this type of design.

A solution to these problems consists of grouping multiple radiating elements and feeding them by a single point [79]. This can be achieved by employing a cavity, which is fed from the feeding system by a single point. The cavity delivers then the signal into multiple radiating elements. In this case, it is necessary to precisely design the cavity to achieve the required field distribution inside it, as well as, select the right position of the radiating elements in relation to the cavity. This technique is used in different concepts

of antennas like Fabry-Perot antennas [31] and SIW cavity antennas [79].

At THz frequencies, large air cavities or dielectric cavities are problematic to manufacture. One of the emerging solutions is etching different structures such as slots and cavities in silicon and creating multilayer structures. This type of design is feasible at THz frequencies, provides low-profile and low size while maintaining great antenna radiation characteristics.

5.1.2 Antenna element design

The antenna array element design consists of four radiating elements and it is fed from a single point of the feeding system. Antenna element is designed in a way that enables further expansion to an array consisting of multiple antenna elements. The multilayer design is fully based on air-filled metalized waveguides, slots and cavities. The design is prepared to operate at a central frequency of 350 GHz.

The design of the antenna elements is presented in Figure 16. All the antenna design dimensions are given in Table 2.

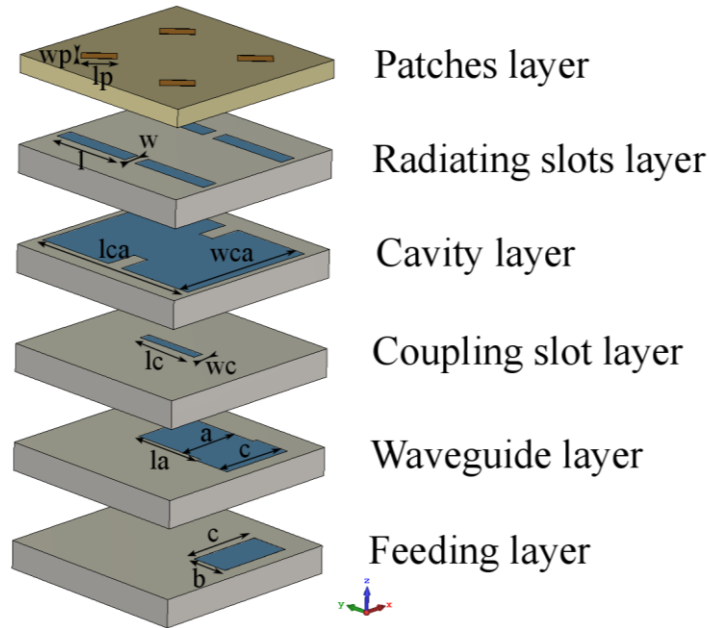


Figure 16. The 2x2 antenna element.

The signal is to fed to the antenna from the bottom through a WR2.2 waveguide. For this reason, the bottom layer – the feeding layer has a slot with the size identical to the size of a WR2.2 waveguide. The feeding layer and the waveguide layer create an E-bend transmission.

The waveguide layer includes a part of a waveguide, this layer is extended to a feeding system when the array is enlarged. In the waveguide, the fundamental mode TE_{10} is excited by the port. EM field in the waveguide is coupled to upper layers by the coupling slot.

Table 2 Antenna element parameters given in millimeters.

Layer	Parameter definition	Value
Patches	Patch length (lp)	0.24
	Patch width (wp)	0.11
	Thickness of the layer (h)	0.127
	Element spacing	0.71
Radiating slots	Slots length (l)	0.63
	Slots width (w)	0.12
	Slots offset in x-axis	0.075
Cavity	Cavity length (lca)	1.36
	Cavity width (wca)	1.1
	Iris wall length	0.25
	Iris wall width	0.11
Coupling slot	Slot length (lc)	0.5
	Slot width (wc)	0.08
Waveguide	Waveguide width (a)	0.5
	E-bend waveguide width (c)	0.57
	Waveguide height (b)	0.285

The signal from the waveguide is coupled to the cavity by the coupling slot. The slot is a shunt slot, positioned longitudinally in the end-left corner of the waveguide to couple the maximum power to the cavity. All the five bottom layers have the same thickness of $t = 0.2$ mm.

The coupling slot is located centrally with respect to the cavity. In the cavity, the iris walls ensure the required field distribution and appropriate impedance matching. The simulated electric and magnetic field distribution in the air-filled cavity is shown in Figure 17. The central-plane of the cavity along the y-axis is equivalent to an electric wall. Therefore, the direction of the field in the right part of the cavity is opposite to the field in the left part of the cavity. Thanks to this, four slots can be excited not only with the same amplitude but also in-phase.

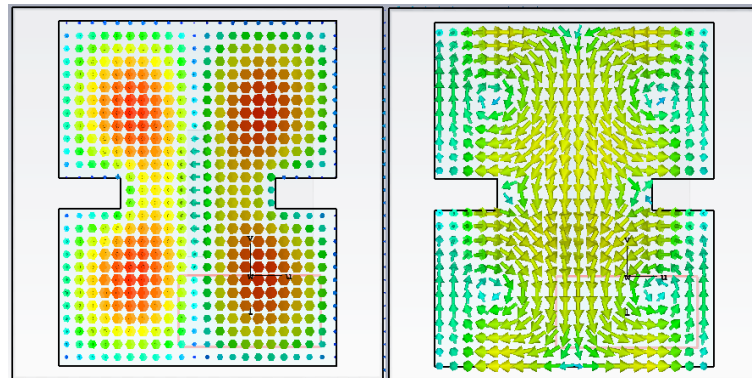


Figure 17. The electric (left) and magnetic (right) field distribution in the cavity of the antenna element.

On top of the cavity, in the radiating slots layer, four rectangular slots are located. If the cavity would be divided into four exact quarters and each radiating slots would be placed exactly centrally of such piece, the radiated power would be low. Therefore, the position of each slot is shifted outside of the center of each quarter of the cavity to ensure the maximum power radiation.

The last layer is a dielectric layer made of Arlon CuClad 217 [80]. The dielectric layer has a height of $h = 0.127$ mm. On the top of the dielectric, metallic, rectangular patches are placed. Each patch is rotated by 45° with respect to the radiating slot below. The power radiated by radiating slots excites metallic patches, and, because of the 45° rotation, two orthogonal modes are excited in each patch and the circular polarization is created. The mechanism of the circular polarization creation is presented by showing the surface current distribution on the patches in Figure 18.

Y-cut through the antenna element is shown in Figure 19 a) to present the electric field distribution inside the structure. The top view of the antenna with all the elements visible is shown in Figure 19 b) for a better understanding of the position of elements.

The size of the antenna element (2×2 array) is $1.75\lambda_0 \times 1.75\lambda_0 \times 1.3\lambda_0$.

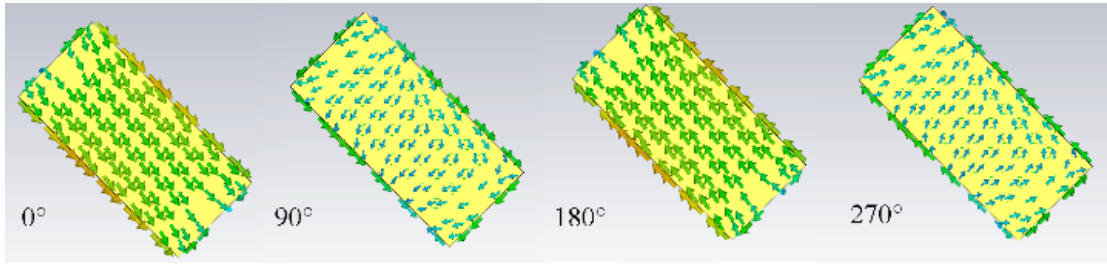


Figure 18. The surface current distribution on the patches in the top layer in phases: 0° , 90° , 180° , and 270° .

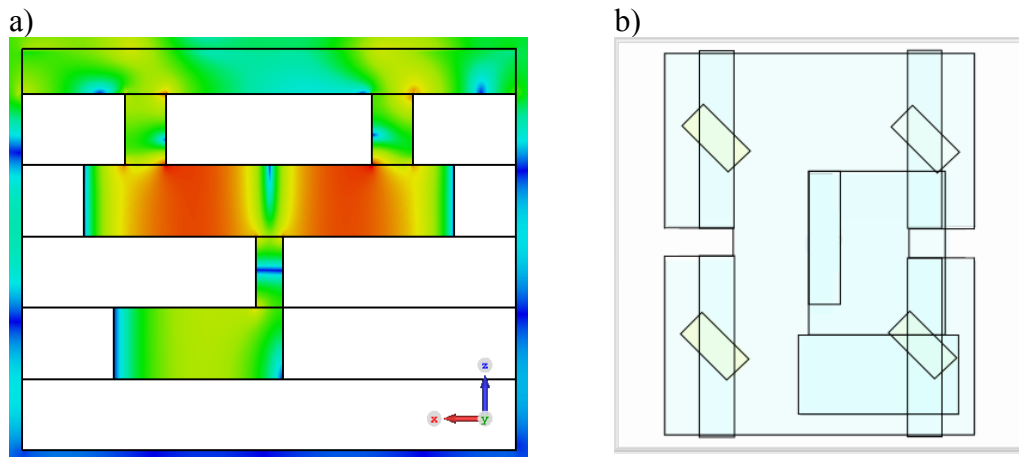


Figure 19. Designed terahertz antenna element a) Y-axis cut, electric field distribution inside the antenna element b) top view.

5.1.3 Design procedure and dimensions considerations

The antenna design is recommended to be started from designing the patches with the radiating slots. By adjusting the radiating slots, required directive radiation

characteristics can be obtained. Later, the cavity can be added and, by adjusting the cavity size and iris walls dimensions, the right field distribution can be obtained.

As the next step, the waveguide with the coupling slots can be adjusted to achieve the right output impedance which matches the input impedance of the cavity with radiating elements. As the final step, the E-bend structure is added.

Waveguide

The successful design of an E-bend with very low losses requires a common stepped geometry to be used. When employing the stepped geometry, the number of layers has to be increased during the manufacturing. In order to simplify the design, no stepped geometry was exploited. The designed E-bend transmission has a transmission coefficient of -0.3 dB.

Coupling slot

The length of the coupling slot is related to the frequency of operation. The width of the coupling slot limits the bandwidth and ensures the impedance matching. The narrower the slot is, the narrower the operating impedance bandwidth is.

A starting point for the right coupling slot length choice is the fact that the length of the slot should be equivalent to half of the wavelength on the central frequency. The width of the coupling slot limits the bandwidth and ensures the impedance matching. The narrower the slot is, the narrower the operating impedance bandwidth is.

Cavity

The mode is a hybrid of mode appearing in cavity of the half-length and the cavity with no iris walls (cases a, d in Figure 20). Iris walls in the cavity influence the electric field distribution, and four maxima or minima can appear. If the iris walls are too long, the maximum of the electric field appears above the feeding slot only, and four slots cannot be excited properly (case b in Figure 20). Therefore, the length of the iris walls has to be optimized (case c in Figure 20). The length of the iris walls was chosen to be 0.25 mm.

Radiating slots

Radiating slots need to be excited with uniform field with the field lines going in the same direction. Otherwise the fields radiated by slots next to each other would get suppressed. The position of each slot is shifted outside of the center of each quarter of the cavity to ensure the maximum power radiation.

In case of a central position, the maximum or minimum of the electric field is exactly below the slot, and no power is radiated. If slots were moved to the borders of the cavity, the distance between radiating elements is too large and negatively influences the sidelobe level. The optimal position satisfying those two constraints was found to be 0.71 mm distance between the slots in the x-axis and y-axis. This distance is also the radiating element separation of the array.

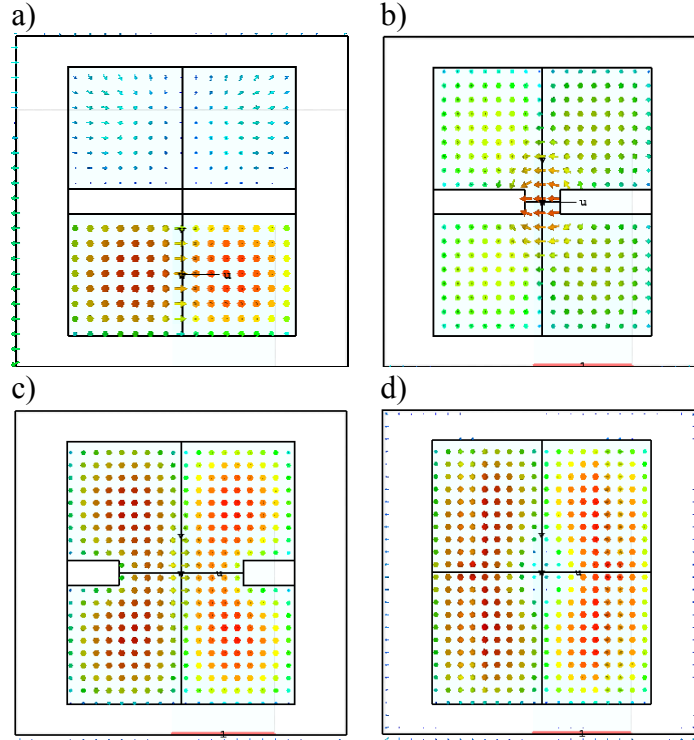


Figure 20. Electric field distribution in the cavity. The cavity
a) of half-length, b) of full-length and long iris walls,
c) of full-length and optimal iris walls,
d) of full-length and no iris walls

Patches

The height of the top layer of the antenna influences the circular polarization. By changing it, the axial ratio bandwidth is moved to higher or lower frequencies. The required low axial ratio in the operating bandwidth can be obtained by tuning the length and the width of the patches. The ratio of the length to the width of the patches is an important parameter here.

5.1.4 The 4×4 antenna array design

The 2×2 antenna element was expanded to the 4×4 array. The top layers were multiplied, and in the waveguide layer, a feeding system was introduced. This ensures an easy array expansion; only the feeding system needs to be designed. The design of the 4×4 antenna array is presented in Figure 21.

The feeding system consists of three waveguide-based T power dividers, which together make an H power divider structure. This structure is widely used and well described [81], [82]. The sizes of waveguides and the E-bend are the same as in the antenna element. To ensure equal power division, good isolation and reflection coefficient iris walls were placed in the middle of the three T dividers. The central iris wall has a size of $0.25 \text{ mm} \times 0.05 \text{ mm}$, while the left and right iris walls have a size of $0.30 \text{ mm} \times 0.05 \text{ mm}$. The feeding system structure is presented in Figure 22.

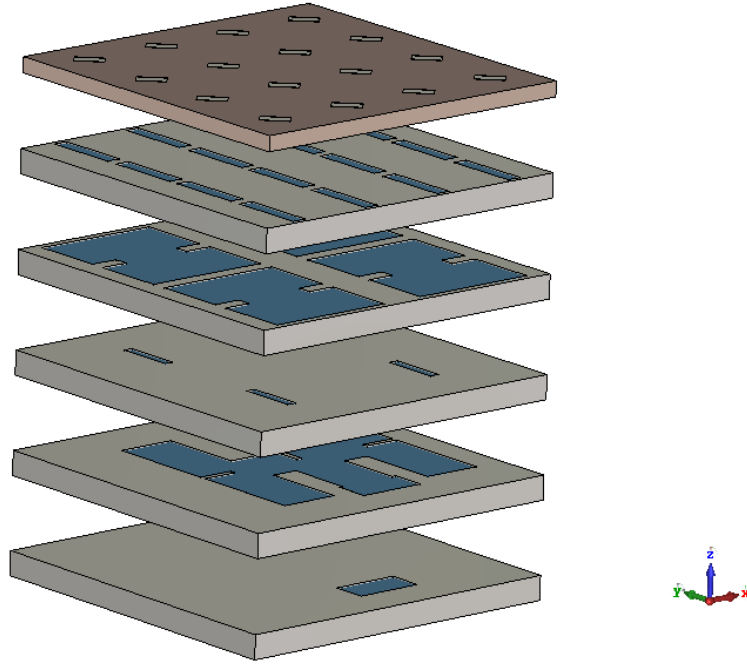


Figure 21. 4x4 antenna array design.

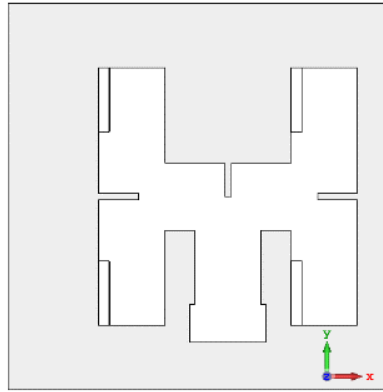


Figure 22. Top view of the feeding system of the 4×4 antenna array with three T-shaped power dividers.

The signal is fed to the antenna array through an E-bend transition located in the center bottom part of the H shaped feeding system. The feeding system has the reflection coefficient below -10 dB. The power splits to the four coupling slots equally with values -6.3 dB and the maximum deviation from this value is 0.04 dB. The transmission from the feeding port to all four ports and reflection coefficient at the feeding port is presented in Figure 23.

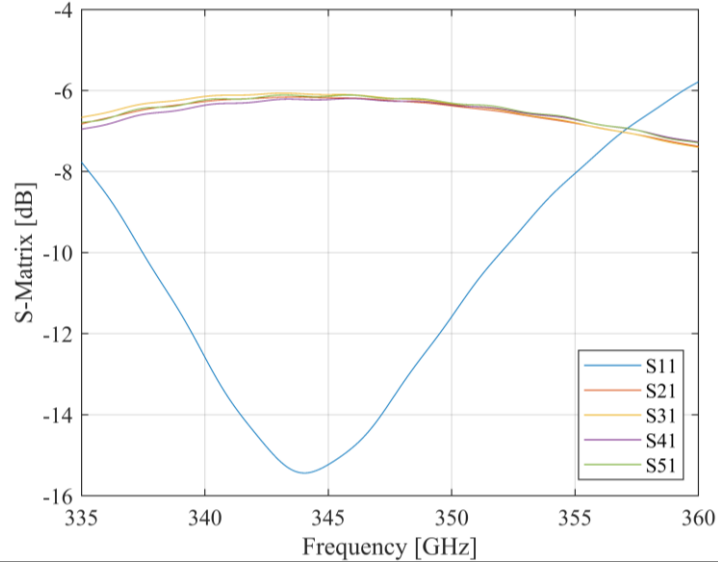


Figure 23. Transmission coefficients and reflection coefficient for the input port of the power divider.

5.1.5 Simulation results

The designed antenna element was simulated in CST Microwave Studio. Where the 2×2 array element achieves a peak of the realized gain for the left-handed circular polarization of 13.8 dBi, the 4×4 array achieves the value of 18.4 dBi.

Frequency responses of the reflection coefficient and realized gain for the left-handed circular polarization of the 4×4 and 2×2 antenna arrays are shown in Figure 24. The 2×2 antenna array operates in a frequency band of 25 GHz and the 4×4 antenna array in a frequency band of 30 GHz. Frequency bands are given for both impedance and polarization (related to axial ratio) bandwidths.

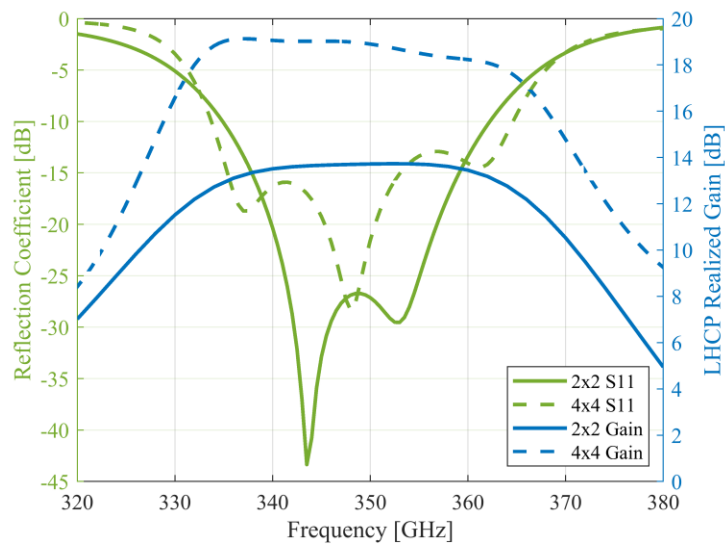


Figure 24. Simulated reflection coefficient and the left-handed circular polarization realized gain response vs frequency of the 2×2 and 4×4 antenna arrays.

The radiation efficiencies for both the 2×2 and the 4×4 antenna arrays are shown in Figure 25. In the operating band, the 2×2 antenna array has radiation efficiency above 0.90 and the 4×4 antenna array above 0.85. The presented efficiencies are given for the precise models that take into consideration all the metal and dielectric losses of materials (see more in the modeling chapter). However, models do not account for manufacturing inaccuracies (including over-etching and surface roughness). The efficiencies are expected to decrease for the fabricated antennas because of fabrication inaccuracies.

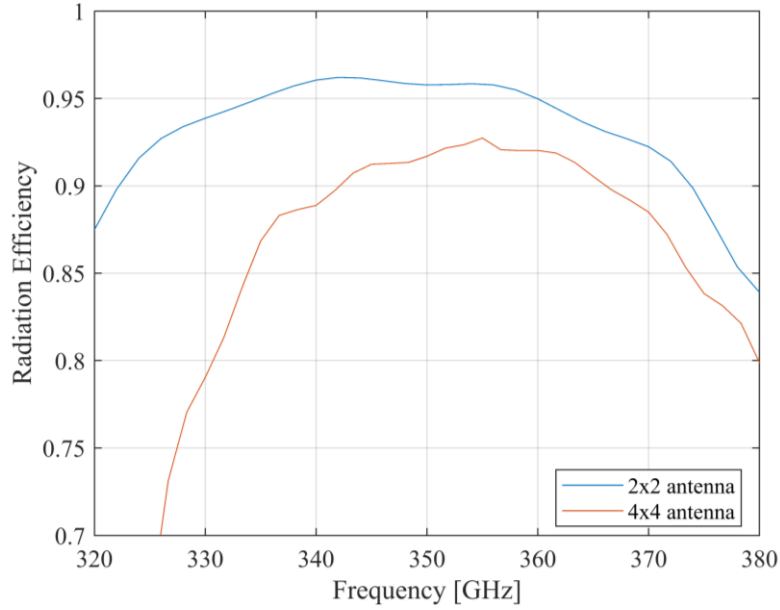


Figure 25. Simulated radiation efficiency of the 2×2 and 4×4 antenna arrays.

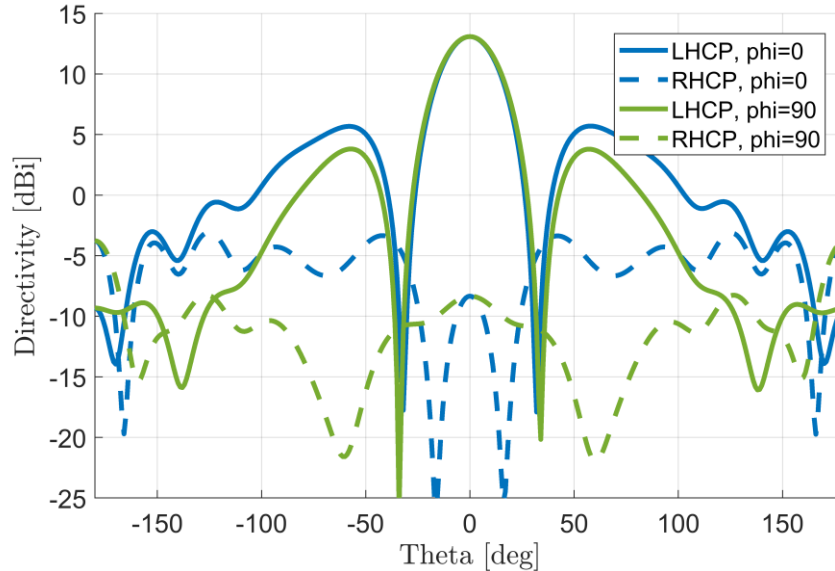


Figure 26. Simulated gain for $\theta = 0^\circ$ and $\theta = 90^\circ$ for the right-handed circular polarization (RHCP) and the left-handed circular polarization (LHCP).

The radiation patterns of the 2×2 antenna element for $\theta = 0^\circ$ and for $\theta = 90^\circ$ for the right-handed and left-handed circular polarization, are depicted in Figure 26. The antenna

shows a highly directive radiation pattern, with front to back ratio of 24 dB. The isolation between co-polar (LHCP) and cross-polar (RHCP) components at the boresight is higher than 35 dB.

Radiation patterns for $\theta = 0^\circ$ and for $\theta = 90^\circ$, for the 4x4 antenna array at the bandwidth border frequencies (335 GHz and 365 GHz) and center frequency (350 GHz) for RHCP and LHCP are shown in Figure 27 and Figure 28.

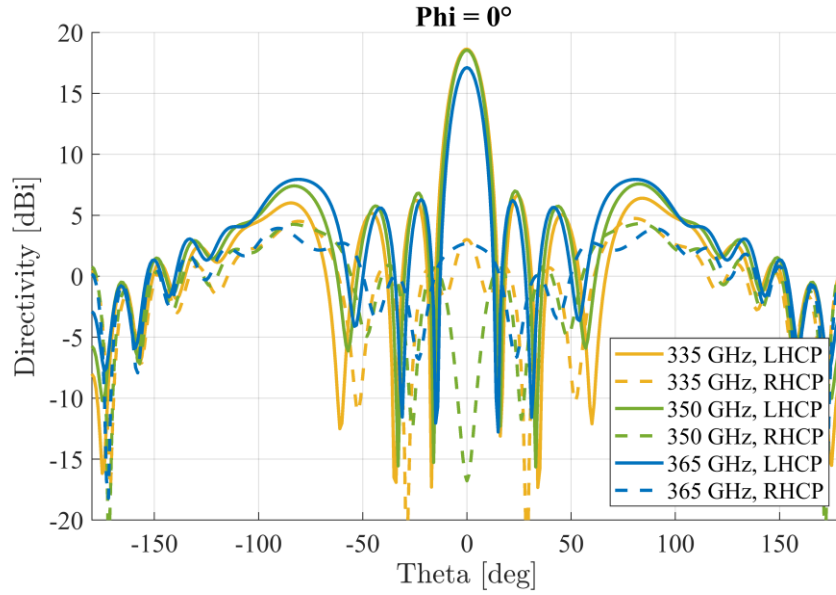


Figure 27. Directivity of the 4x4 antenna array for $\theta = 0^\circ$.

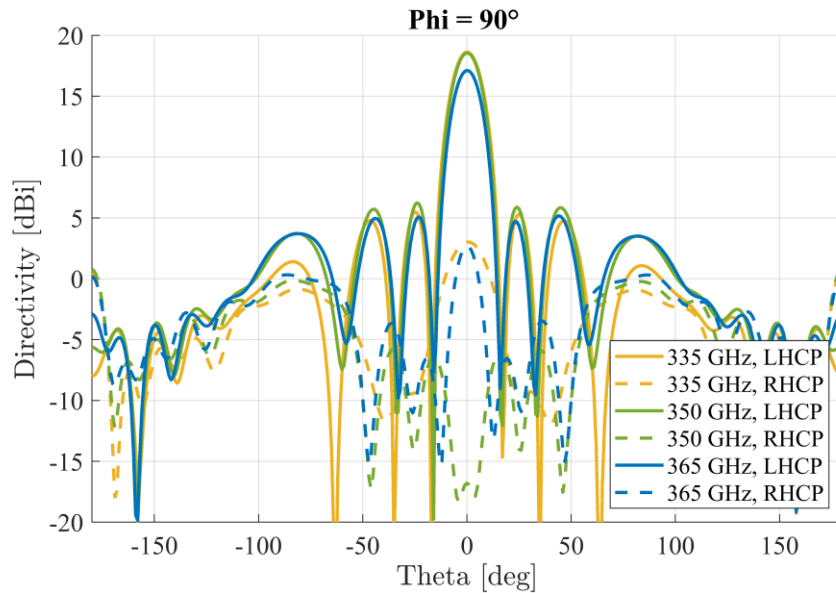


Figure 28. Directivity of the 4x4 antenna array for $\theta = 90^\circ$

Pre-manufacture sensitivity analyses

Over- and under-etching are common fabrication problems of silicon technology. A sensitivity analyses to over- and under-etching of 10 μm on all etched elements

parameters was performed on the 2×2 antenna array. The results are shown in Figure 29. It can be observed, that under-etching moves the reflection coefficient minimum to higher frequencies, and vice versa (slots become larger or smaller). In simulations, all the parameters are under- or over-etched to get the worst case. The reflection coefficient results differ slightly from the results shown in Figure 24 because here they were calculated for the antenna without the E-bend.

Misalignment of layers is another common manufacturing problem. Modern technologies reduce the misalignment to $10 \mu\text{m}$. In the analysis, one from two neighboring layers was moved by $10 \mu\text{m}$ in x and y directions, and another one was moved by $-10 \mu\text{m}$ in x and y directions. Hence, the total relative misalignment was $20 \mu\text{m}$. The results are shown in Figure 30.

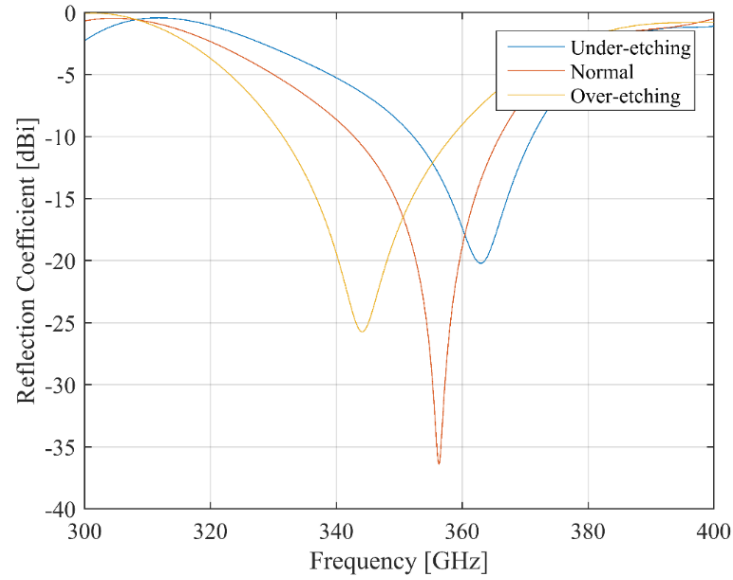


Figure 29. Frequency response of the reflection coefficient of the 2×2 array with under-etching (blue), normal etching (red), and over-etching (yellow).

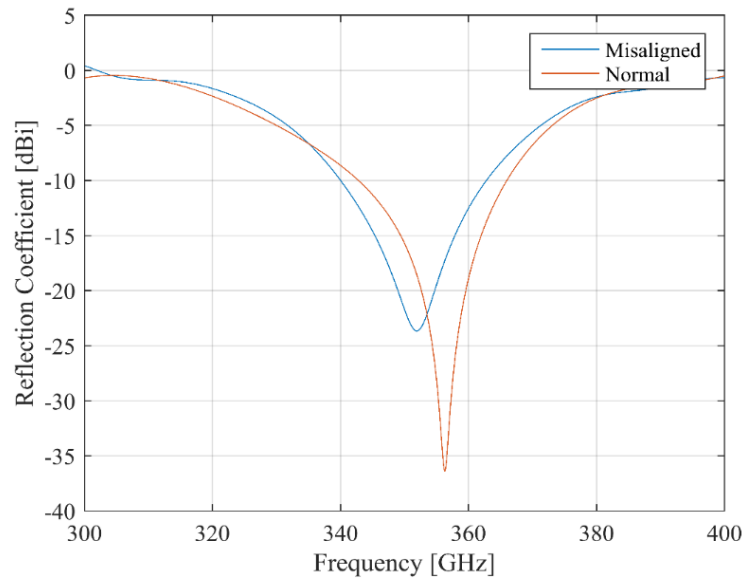


Figure 30. Frequency response of the reflection coefficient of the models with ideal (red) and misaligned (blue) layers.

Characterization of dielectric materials at THz frequencies is problematic. In datasheets, substrate parameters are specified at 10 GHz [24] ($\epsilon_r = 2.2$ and $\tan \delta = 0.009$ for Arlon CuClad 217). In [25], dielectric parameters of dielectrics similar to Arlon CuClad (made from similar materials) were measured. The results prove that this types of materials hold relatively constant permittivity in the band of 0.4 THz to 1.0 THz, with changes around 0.02. Therefore the antenna performance with the permittivity varying for ± 0.02 was analyzed. The reflection coefficient remained unaffected by changing permittivity. The results of changes of dielectric permittivity influence on axial ratio and gain are shown in Figure 31. It can be observed that the gain remains unchanged, and the minimum of the axial ratio is slightly shifted.

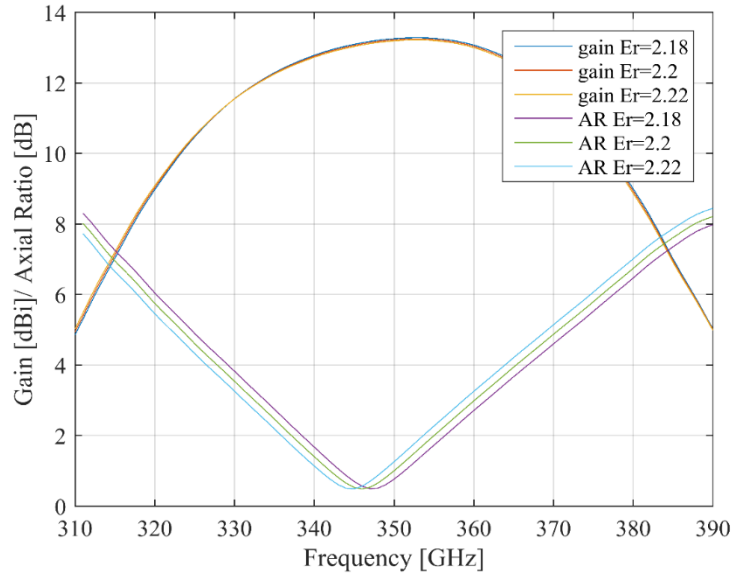


Figure 31. Gain and axial ratio frequency responses of 2×2 array for changing permittivity.

5.1.6 Comparisons with state-of-art

The presented antenna design is the first design operating at 350 GHz with circular polarization, with wide impedance and polarization bandwidth and gain above 18 dBi. The array can be easily enlarged by a simple expansion. In Table 3, comparison to other high-gain/circularly polarized antennas is given. The size is given as a diagonal in relation to λ_0 .

The bow-tie antenna presented in [27] operates with the circular polarization and in a wide band, however, has a gain of only 6 dBi. Horn antennas require a large height [28].

Fabry-Perot designs [31]–[33] provide circular polarization and comparable gains but have very narrow bandwidths, larger electrical sizes and operate only at lower frequencies. There is one design presented at THz [3], but it includes only simulations, was never fabricated and the manufacture constraints for THz frequencies were not considered.

Although dielectric rod array [6], lens array [4], corporate feed metallic posts array [42]

and slots array [43] can achieve high gains and wide bandwidths, these antennas exhibit significantly larger heights and do not radiate with circular polarization.

Most of the antennas present interesting results, however, none of them achieve simultaneously high-gain, circular-polarization, wide bandwidth, low profile, and THz operation (feasibility of fabrication the design at THz frequencies).

Table 3. Comparison of high-gain/circularly polarized/THz frequency antennas with this work. Operation frequency f_c , impedance bandwidth BW , and circular polarization CP .

Ref.	Design	f_c (GHz)	Height (λ_0)	Size (λ_0)	BW (%)	Max gain (dBi)	CP
[27]	Bow-tie	350	0.12	2.3	20	6	Y
[28]	Horn	340	8.4	4	12	20	N
[31]	Fabry-Perot	10	0.05	5.7	0.3	15	Y
[31]	Fabry-Perot	1000	0.006	4.2	1.4	12	Y
[33]	Fabry-Perot	15	0.85	9.9	2	19	Y
[35]	Conical spiral	8	4.5	5.7	150	10	Y
[37]	Dielectric Rod	61	4	4.1	2	15	Y
[36]	4 × 4 Lens	257	14	31.1	160	30	N
[39]	4 × 4 Dielectric Rod	92.5	20.6	4.3	38	23.5	N
[40]	Dielectric Rod	155	11	0.76	19	17.5	N
[42]	4 × 4 Met. posts array	1000	3	2.8	26	14	N
[43]	16 × 16 Slot array	350	7	18.1	13	30	N
[44]	16 × 16 Slot array	61.5	2	21.5	4	33	Y
This work	2 × 2 Slot array	350	1.3	2.5	8	13.8	Y
This work	4 × 4 Slot array	350	1.3	5	9	18.4	Y

5.2 MODELING OF THE THZ ANTENNA

The in-depth analysis of a terahertz antenna array with thin metallic walls is costly in terms of computational resources needed. A simplified analysis is necessary for quick, preliminary antenna design, and can be useful during the optimization. To demonstrate potential simplifications, different models of the 2×2 array were created.

High surface roughness and different thickness of the metallic layers can influence the antenna performance. Analyses of the significance of these parameters on antenna characteristics are needed.

5.2.1 Different models and boundary conditions

Three different models of the 2×2 array were defined as:

- The PEC model. Antenna structure is fully constructed of a perfect electric conductor with hollow waveguides.

- A full-gold model. The PEC in the PEC model was replaced by gold. Hence, the antenna was conceived as hollow waveguides and slots in the bulk gold.
- The precise model of the antenna. This model is accurately modeling the structure in a way it is manufactured, serves here as a reference. Silicon structure ($\epsilon_r=11.64$, $\tan \delta = 0.001$ at 350 GHz [83]) with gold metallization of the hollow waveguides and slots and in-between the layers. The gold metallization layer is $0.4 \mu\text{m}$ thick.

In Figure 32, three models are presented. Different materials were depicted by different colors: in beige the dielectric (Arlon CuClad 217), in orange copper, in grey PEC, in yellow gold and in pink silicon. The gold layer thickness in the precise model is not in scale for better visibility.

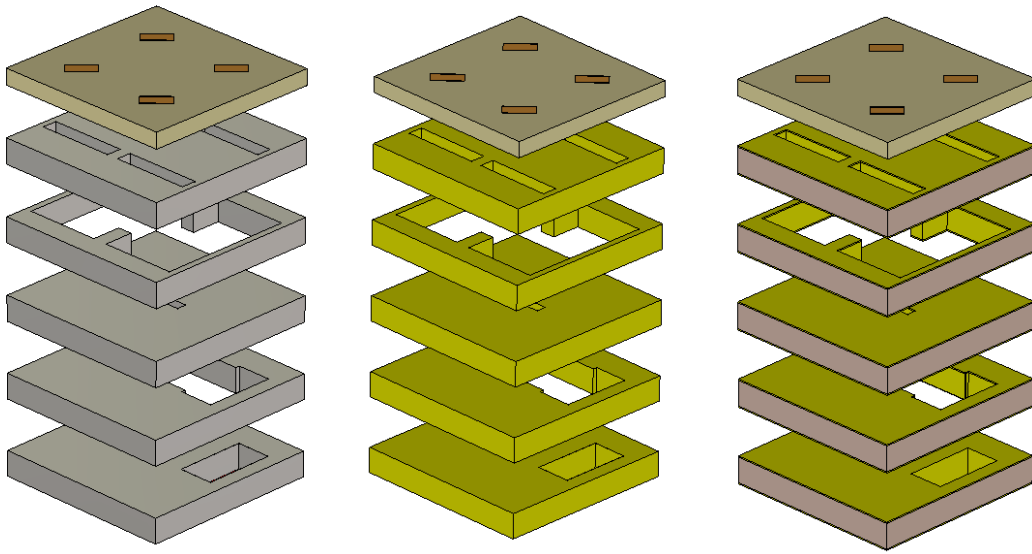


Figure 32. Three analyzed models of the antennas from the left: PEC model, full-gold model and precise model.

The models were analyzed in CST (time-domain finite-integration technique) and HFSS (frequency domain finite-element method).

Frequency responses of the magnitude of the reflection coefficient at the input port of the antenna array of different models are shown in Figure 33. PEC models and bulky-gold models result in very similar responses. The difference between CST and HFSS is given by different meshes. Whereas CST approximated the structure by 2.500.000 elements, HFSS used about 100.000 elements to represent the structure.

Reference models developed in CST and HFSS show a reasonable agreement. Whereas all the HFSS results are close to the reference, CST outputs for simplified (PEC and full-gold) models slightly deviate in the resonant frequency (352 GHz versus 346 GHz). On the other hand, the good matching (below -35 dB) and the bandwidths are almost identical.

Frequency responses of gain and axial ratio of the antenna array in the main lobe direction of the different models are shown in Figure 34. Since responses of the axial ratio and gain are in a close agreement for the bulky-gold model and the PEC one, the

only line denoted PEC is used to represent both the models. The gain response shows the realized gain for left-handed circular polarization.

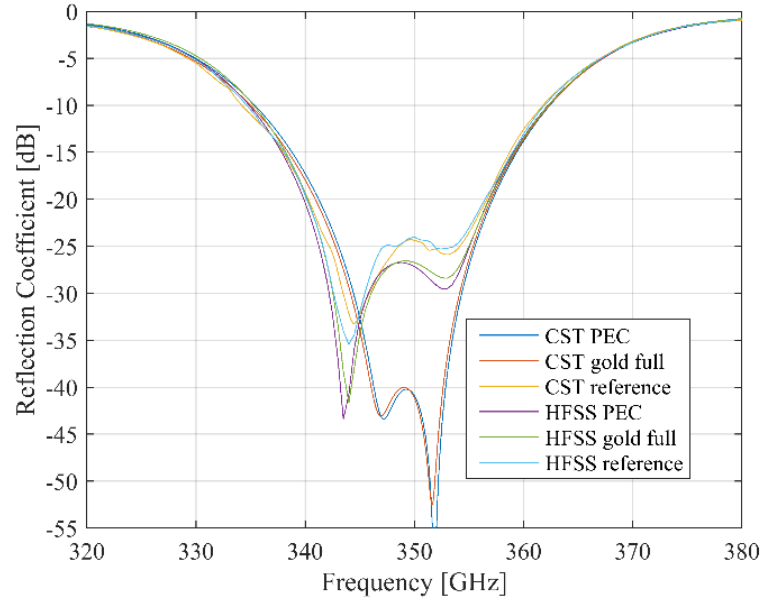


Figure 33. Frequency response of reflection coefficient at the input port of the antenna array: comparison of different models and solvers.

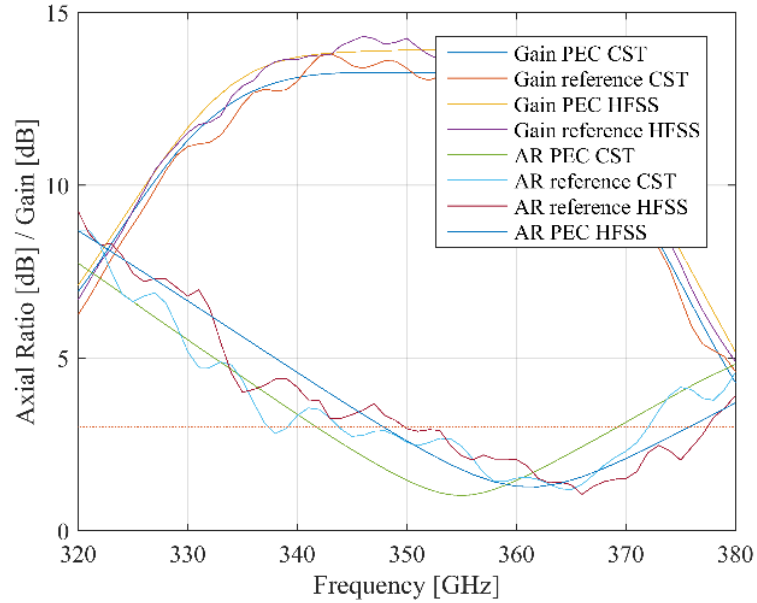


Figure 34. Frequency response of gain and axial ratio of the antenna array: comparison of different models and solvers.

Frequency responses of reference models exhibit deteriorations compared to smooth responses of simplified models. These deteriorations are related to the fact, that the whole outside surface of the antenna is metalized for the fully metallic models, while the outer surface consists mostly of silicon for the reference model (the layers on the edges cannot be fully metalized during the manufacturing). The lack of the metallization on the outer walls causes changes in radiation patterns, which is closely related to gain

and axial ratio. Even though, there are minor discrepancies in the results, an agreement between simplified and reference models is reasonable. Additionally, outputs of the HFSS simplified model are closer to precise models than CST ones.

The numerical parameters of compared models are summarized in Table 4. The CST reference model requires 10 times more mesh cells than simplified models; hence the computation time is increased from 2 minutes to more than 2 hours. In the case of HFSS models, the fastest analysis was achieved for the bulky-gold model (not the PEC one).

Table 4. Numerical parameters of models shows that the CST PEC model shows the minimum CPU-time and memory demands. Hence, the CST-PEC model can be selected as a proper surrogate model for optimization. Considering the accuracy of results and the computation time, the HFSS bulky-gold model produces results agreeing well with the reference model. Nevertheless, CPU-time results are significantly lower compared to the reference model. For fine modeling, the HFSS bulky-gold model is recommended.

The PEC CST model is recommended to be used for fast and time-efficient calculations (a recommended choice for optimization). The antenna modeled this way can be fully characterized within the whole operating band in 2:41 minutes.

Table 4. Numerical parameters of models

Model	Cells [$\times 10^3$]	CPU time [hh:mm:ss]	Memory [GB]
CST PEC	2 500	00:02:41	1.1
CST bulky gold	2 500	00:02:53	1.2
CST reference	24 500	02:31:00	7.4
HFSS PEC	105	02:15:00	7.0
HFSS bulky gold	111	00:50:00	7.9
HFSS reference	131	03:45:00	8.3

5.2.2 Surface roughness and layer thickness influence on the antenna performance

Due to manufacturing inaccuracies, the surface roughness of gold can vary. Analyses of increasing surface roughness influence on antenna parameters were performed with the use of the precise model from 5.2.1. The model was analyzed in CST Studio. The surface roughness influence on the reflection coefficient is shown in Figure 35. It can be seen that the higher the surface roughness the more the reflection coefficient minima is moved to lower frequencies. Similarly, the influence of the increasing surface roughness was observed on the radiation efficiency, it is presented in Figure 36. In the picture it can be seen that the antenna with a gold surface roughness of 10 nm or 100 nm has radiation efficiency of around 0.9 in the operational frequency band, however, when the surface roughness is increased to 500 nm the radiation efficiency is lowered to around 0.7 in the operation band and for the roughness of 1000 nm the radiation efficiency is only around 0.6. The values of 0.5-0.7 are commonly reported as efficiencies of the antennas in the THz region[84], [85].

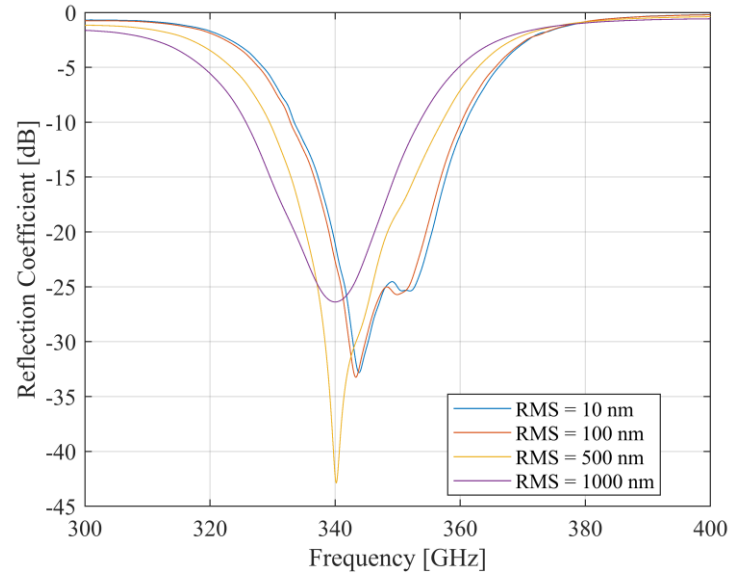


Figure 35. Increasing surface roughness (RMS) influence on the reflection coefficient plotted in frequency.

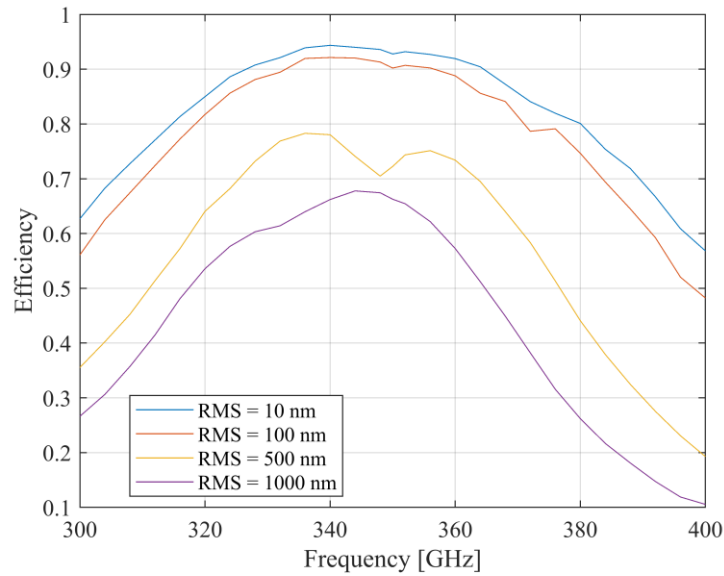


Figure 36. Radiation efficiency of the 2x2 antenna array in frequency for increasing gold surface roughness (RMS).

Similar analyses were done for varying gold thickness, the analyzed values were 100 nm, 400 nm, 1 μm , 10 μm . Manufacturing possibilities of gold evaporation and sputtering were taken into consideration while choosing the analyzed gold thicknesses. The gold conductivity 45 MS/m was used. No significant influence on radiation efficiency or reflection coefficient was observed.

Discrepancies in the radiation patterns were found for the highest analyzed gold thickness value of 10 μm . The directivity patterns for $\phi = 0^\circ$ and $\phi = 90^\circ$ and gold thicknesses 100 nm, 400 nm, 1 μm , 10 μm are shown in Figure 37 and Figure 38. Different radiation patterns for models with gold thickness of 10 μm are related to the model design, in which the outer walls of the antenna are not metalized. When the gold

layer thickness between the layers is low, the whole outer surface of the antenna is behaving as if it was fully made of silicon. However, when the gold thickness between the layers increases then it influences the radiation pattern. This is can be associated with the increased metallic surfaces that are reflective for the radiated wave.

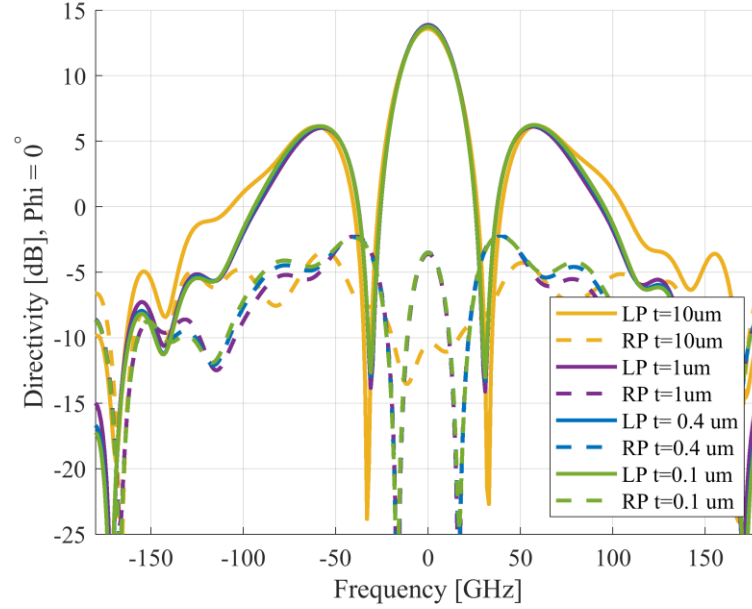


Figure 37. Directivity in $\phi = 0^\circ$ of the 2x2 antenna element for different thicknesses of the gold layer.

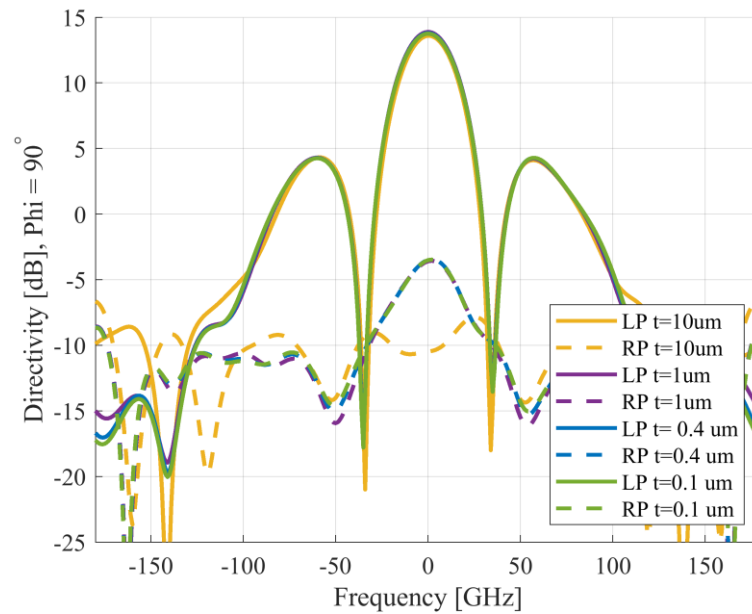


Figure 38. Directivity in $\phi = 90^\circ$ of the 2x2 antenna element for different thicknesses of the gold layer.

5.3 ANTENNA ARRAY WITH BEAM STEERING CAPABILITY

One of the ways to overcome the high losses in the THz region is the employment of beam steering. While the use of beamforming creates a very directive radiation pattern and enhances the gain, beam steering allows to switch the direction of the radiation of the antenna. By choosing the proper direction of radiation, the beam can be steered in the direction of the receiving terminal. In order to incorporate beam steering in an antenna array, it is necessary to include phase shifters in the feeding system.

5.3.1 Antenna design

Inspired by the impressive results mentioned before, the designed antenna array was extended to 8×8 elements to incorporate beam steering. The antenna design is presented in Figure 39. Liquid crystal, carbon nanotubes or MEMS phase shifters could be implemented in the antenna feeding layer to achieve phase shifting.

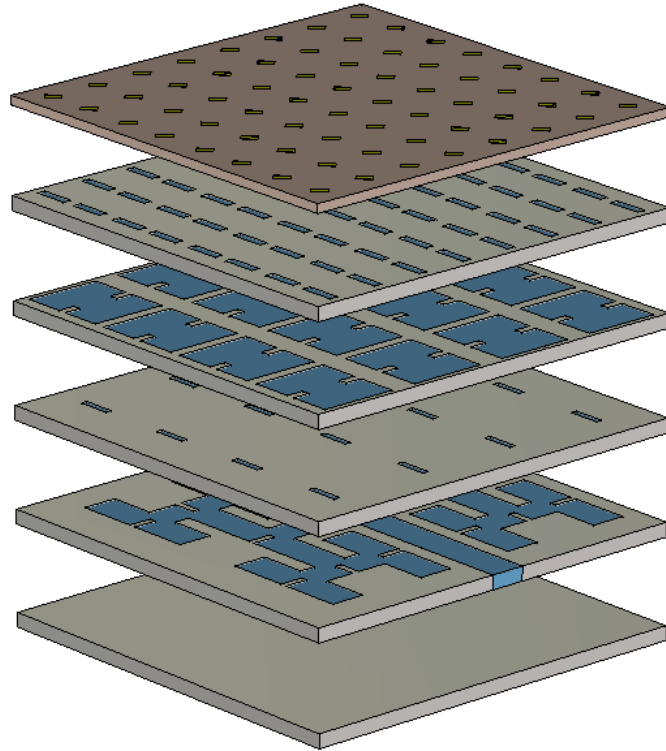


Figure 39. The 8×8 antenna with beam steering design capability.

The feeding system can be expanded in the same manner as for expansion from 2×2 to 4×4 array. The design of the feeding layer is shown in Figure 40. Phase shifters could be placed into the feeding layer, which requires appropriate adjustments in this layer.

The feeding system has to be redesigned depending on the type of a phase shifter employed. Since the type of the phase shifter is unknown, the phase-shifting was introduced automatically in the signal fed through the coupling slots to simulate the antenna performance.

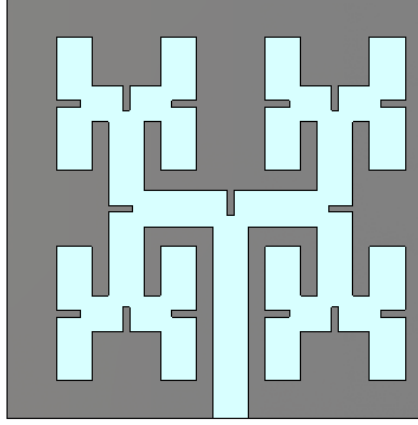


Figure 40. Design of the feeding system of the 8×8 antenna array.

5.3.2 Simulation results

The phase shift is introduced in the feeding layer in a way that every column of coupling slots had a phase shift of $+30^\circ$ in relation to the previous column. In this way, each 2×2 antenna array element is fed by the signal with the same phase. By introducing such a progressive phase shift on each column of coupling slots, the azimuthal tilt of the beam was achieved, with the beam tilted by 2° . By increasing the progressive phase shift to 80° , the azimuthal tilt of 8° was obtained.

By changing the phase shift for every verse of coupling slots, scanning in elevation was achieved with the same maximum tilt of 8° for 80° progressive phase shift in each verse. The azimuthal scanning presented by radiation patterns in gain of the array with progressive phase shifts from -80° to 80° is shown in Figure 41. Similarly, the elevation scanning is shown in Figure 42. In such a manner, the beam can be tilted simultaneously both in azimuth and elevation.

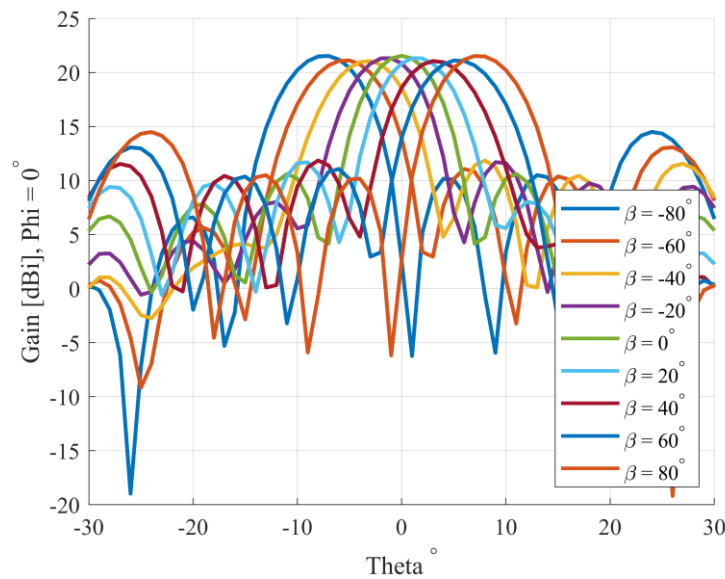


Figure 41. 8×8 antenna array directivity, $\theta = 0^\circ$, scanning in azimuth. β describes the progressive phase shift.

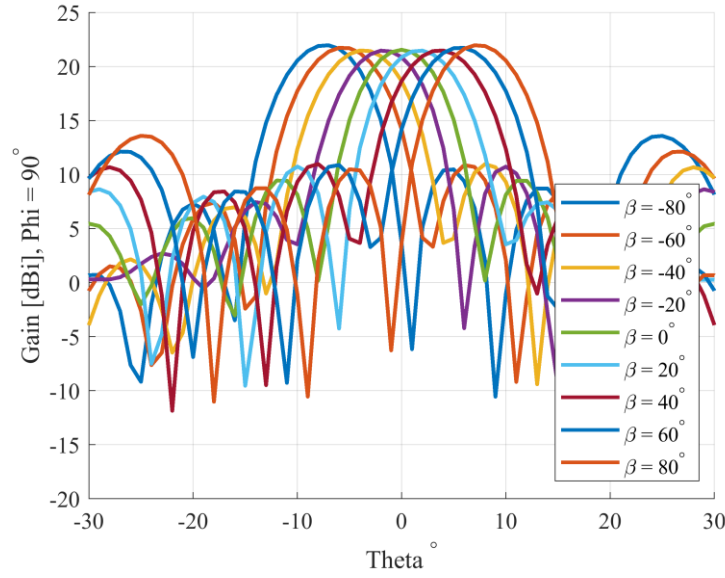


Figure 42. 8x8 antenna array directivity for $\theta = 90^\circ$ scanning in elevation. β describes the progressive phase shift.

The antenna radiates waves with left-handed circular polarization. The axial ratio and gain plots in frequency are presented in Figure 43 for the $\theta = 0^\circ$ and main beam direction of 0° . The axial ratio bandwidth for each of the available beams between -8° to 8° in azimuth and elevation is at least 10 GHz, from 345 GHz to 355 GHz. The impedance bandwidth of the antenna is from 345 GHz to 355 GHz. The gain of the antenna is above 21 dBi in the whole bandwidth and for all beam directions.

These analyses prove that the antenna design is suitable for advanced beam steering applications, with scanning in two dimensions, where a directive circularly polarized beam is radiated with very high gain and in a wide bandwidth.

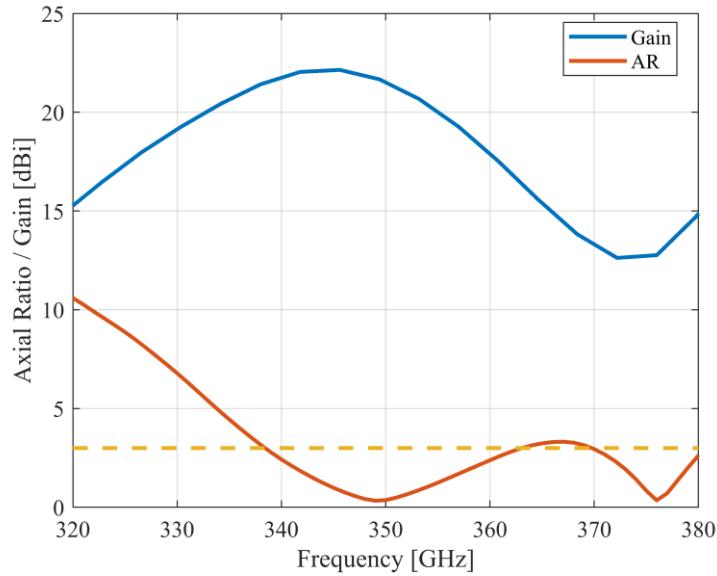


Figure 43. Axial ratio and gain plot in frequency for the $\theta = 0^\circ$, and $\beta = 0^\circ$. β describes the progressive phase shift.

5.4 SUMMARY

In this chapter, the complete design of high-gain, low profile 2×2 antenna element with corporate feed is presented. The principle of feeding, radiation and creation of circular polarization are presented. The instructions for designing and optimization of such design are given. The design of the expanded 4×4 array is described.

Two designed antenna arrays are in 2×2 and 4×4 configuration. The antennas operate with circular polarization at 350 GHz, have polarization and impedance bandwidths of 25 GHz and 30 GHz, with peak gains 13.8 dBi and 18.4 dBi, respectively. Antenna arrays have a low profile of only $1.3 \lambda_0$.

The antennas performance is compared to other state-of-art designs. To author's knowledge, the presented design is the first antenna operating at THz frequency with simultaneously achieving such high gain, circular polarization, low-profile, wide bandwidth, and the possibility to extend to larger antenna arrays without significantly increasing the manufacturing/assembly complexity.

Moreover, the development of different full-wave models of a terahertz antenna array is discussed. The performances of the analyzed models in two commercial solvers are compared, and the best models for different applications are recommended. The parametric analyses of surface roughness and gold layer thickness are performed prior to manufacture. It is concluded that increasing surface roughness influences the radiation efficiency negatively and the gold layer thickness does not influence the antenna performance significantly. However, very thick gold can change the radiation pattern slightly.

The 8×8 antenna array with beam steering capabilities is presented. In the feeding layer of the designed antenna array, phase shifters were implemented. The antenna operates at 350 GHz with circular polarization. By introducing a progressive phase shift from -80° to 80° in the feeding layer, the beam can be steered from -8° to 8° in both the dimensions: elevation and azimuth. The gain of the antenna remains above 21 dBi for all the beam directions.

6 FABRICATION TECHNOLOGY AND MEASUREMENTS

In this chapter, the fabrication technology is discussed. The antennas designed in chapter 5 were manufactured in micromachining technology. All the steps are described in detail and photos of the samples during fabrication and final manufactured antennas are shown. The fabricated antennas are characterized by their reflection coefficients. The surface roughness measurements by Scanning Probe Microscope and Electron Microscope are presented.

6.1 MANUFACTURING TECHNOLOGY

The short description of the fabrication process is given here. Later, it is followed by a detailed description of each step.

- Prior to manufacture, elements necessary for the alignment of the layers of the antenna were added. Two big circles and three small circles were included in the design. Also, the size of each layer was enlarged to 1 cm \times 1 cm for easier handling and mounting on the flange.
- Structures (slots, cavities and waveguides) were cut by a laser in a p-type, 200 μ m thick, 2-inch silicon wafer. The average accuracy of the cut of structures was about 15 μ m.
- Wafers were diced into 1 cm \times 1 cm samples.
- The 400 nm thick gold layer was evaporated on the samples. The samples were tilted by 15° and were being rotated during the evaporation to ensure that gold covers surfaces inside the cavities and slots.
- Samples were bonded using silicon eutectic bonding, under 330° C and an average of 100 N pressure on a FineTech Flip Chip machine. Bonding was performed layer by layer. Each process lasted 55 minutes.
- Copper patches on the top dielectric layer (Arlon CuClad217) were etched using a standard lithography process with a negative photoresist nLOF.
- A dielectric top layer was precisely aligned and glued to the antenna using the bonding machine without any heating.

The microfabrication steps are depicted in Figure 44.

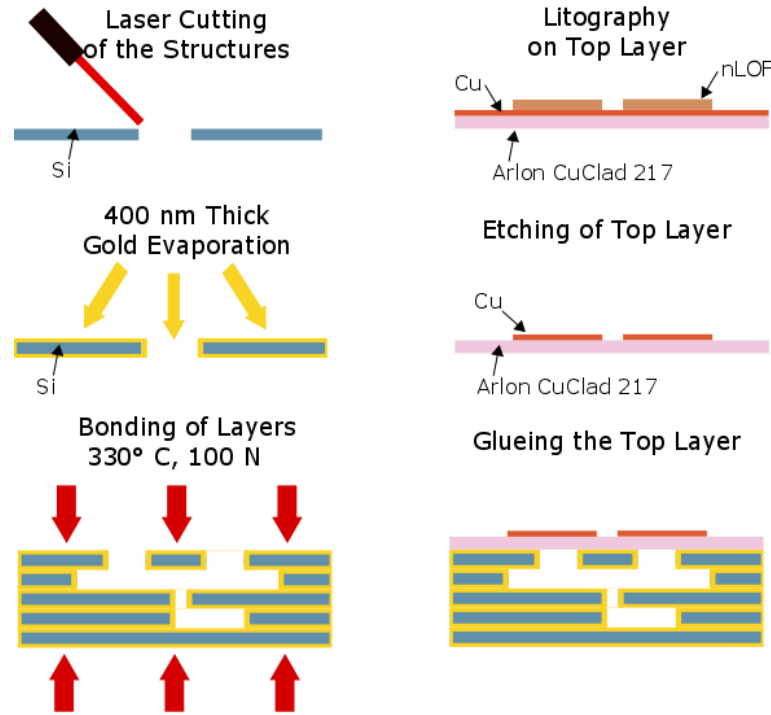


Figure 44. Microfabrication steps of the antennas.

6.1.1 Structures etching

Antennas were manufactured in p-type silicon wafers with a thickness of 200 μm and a size of 2 inches.

First, a reactive ion etching technology was tested in order to etch the antenna structures in silicon layers. Test silicon samples were cleaned with acetone, propanol and oxygen plasma in Oxford Instruments Plasma Lab 80. Positive photoresist AZ1518 was put on the samples and spin-coated for even photoresist distribution. Later the masks were aligned using the mask aligner machine, the photoresist was exposed to light and developed using the developer AZ400K mixed with H_2O in proportions 1:4.

As a next step, a nickel was sputtered on the samples. After the lift-off process, the remaining nickel formed a mask for the etching process and was measured to be 450 μm . Samples prepared in the described way were put into the chamber of Oxford Instruments Plasma Lab 80 machine to perform reactive ion etching. CF_4 was chosen with 45 sccm flow together with oxygen with 5 sccm flow. The forward power was 250 W, the process lasted for 60 minutes.

Later, the thickness of the etched area was measured. We calculated that the etch rate of the process was 0.5 $\mu\text{m}/\text{min}$. The aspect ratio was around 40% which was considered unacceptable. Other parameters for the etching were tried, but none of them gave satisfactory etching results. For the reason of low etch rate and high aspect ratio, the etching with reactive ion etching process was dismissed.

The cavities, slots and waveguides were cut in the wafers by laser etching. The cutting was performed with ultrashort laser pulses and the cut was produced through layer-by-layer ablation of material. On four Si wafers, all of the structure sizes were measured

and compared with the project values. The average accuracy of the cut structures was around 15 μm . Almost all the structures were over-etched. Very narrow iris walls in the feeding layer of the 4x4 antenna array were very sensitive and prone to being destroyed. A lot of caution had to be applied while handling or cleaning these structures.

6.1.2 Wafer dicing

In the next step, the wafers were diced by a dicing machine with a diamond blade into 1 cm x 1 cm samples. The wafer has to be stuck to an adhesive foil before the dicing so during the dicing all elements cannot move. The samples after dicing are presented in Figure 45. In the presented photo, the wafer is still stuck to the adhesive foil. In order to remove the foil, the UV light was applied, which melt the glue on the foil and enabled easy foil removal. Later, the samples were cleaned by acetone, propanol and finally by oxygen plasma in Oxford Instruments Plasma Lab 80.



Figure 45. Wafer with the 4x4 antenna array layers after dicing into samples.

6.1.3 Gold evaporation

Before the gold evaporation, it was necessary to mount the samples to a rotating device. The samples mounted onto the rotation device are shown in Figure 46. Gold was evaporated on all the samples on both sides by a Leybold evaporator. A rotation device with an implemented tilt of 15° was used to ensure even deposition inside the vertical walls. The metal deposition process started with titanium evaporation, which is used for enhanced adhesion of the gold layer to the silicon surface. The inside of the gold evaporation chamber is presented in Figure 47.

The rotation device with samples mounted to can be seen in the top of the picture, next to there a similar plate with quartz in the middle of it for estimation of the gold layer thickness. Below the two round plates, there are two small concave elements which hold the gold during the evaporation. These elements are connected to a current source which

heats them together with the gold. By reading the frequency at which the quartz is oscillating, it is possible to estimate the gold layer thickness on the quartz. By controlling the current applied to the gold holders, the speed of the evaporation can be controlled or stopped completely. The whole process can be performed only under vacuum conditions which are achieved by a pump with the help of a nitrogen-based cooling system. It takes around 8 hours for the machine to achieve a vacuum before the evaporation process can be initiated.



Figure 46. Silicon samples on the holder before gold evaporation.



Figure 47. The inside of the gold evaporation chamber.

After the gold evaporation, the metallic layer was measured by a Dektak Mechanical Profilometer. The thickness of the evaporated gold was measured to be 400 nm, which is 268 nm thicker than the calculated skin depth of gold on 350 GHz.

6.1.4 Bonding

The bonding process was performed by FineTech Flip Chip machine which does not provide automation of the bonding nor utilizes a vacuum environment for the process, thus simplifying and reducing the costs of the process. The bonding machine provides a good alignment thanks to two cameras with a zoom system and software that enables a clear view of the alignment.

Two samples are aligned first. Later, one of them is placed on top of the other with selected load for a specified period of time with heat applied from top and bottom. A study of the optimal bonding conditions was performed. It was found that a temperature higher than 330° C melted the gold and penetrated inside the vertical structures. Temperature lower than 320°C resulted in a lack of bonding and caused an eventual disconnection of the layers. Too low loads resulted in an unsuccessful bonding processes. Applying higher loads than 160 N for 5 layers caused the silicon to break. The optimal process for bonding was found to be 330°C heat from both top and bottom and a load of 80 N for 55 min for bonding two layers.

To bond three layers, the same process was used. For every next layer, the load was increased by 20 N. Therefore, 120 N was used to bond five layers. The manufactured 2×2 antenna is presented in Figure 48. The 4×4 and 2×2 arrays are shown in Figure 49.

In Figure 50 the Flip Chip bonding machine is presented. On the right side, the arm that is used for applying the pressure can be observed. In the photo, the arm is in use and it is in the lower position. On the top and the left side, two cameras with light sources can be seen. There is a being bonded in the central part of the heating plate with a vacuum.

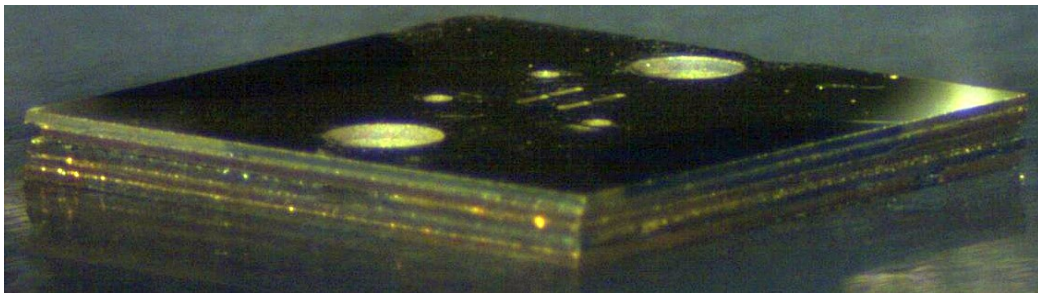


Figure 48. Side view of the 2x2 antenna array before mounting the top layer, taken by the bonding machine camera.

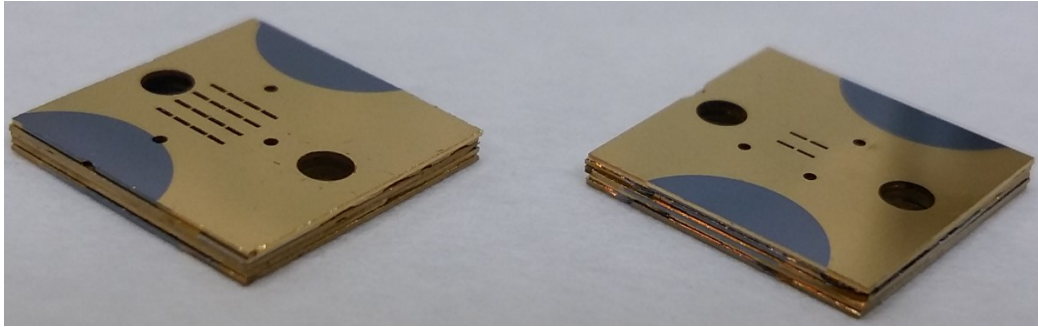


Figure 49. 4x4 and 2x2 antennas before mounting the top layer.

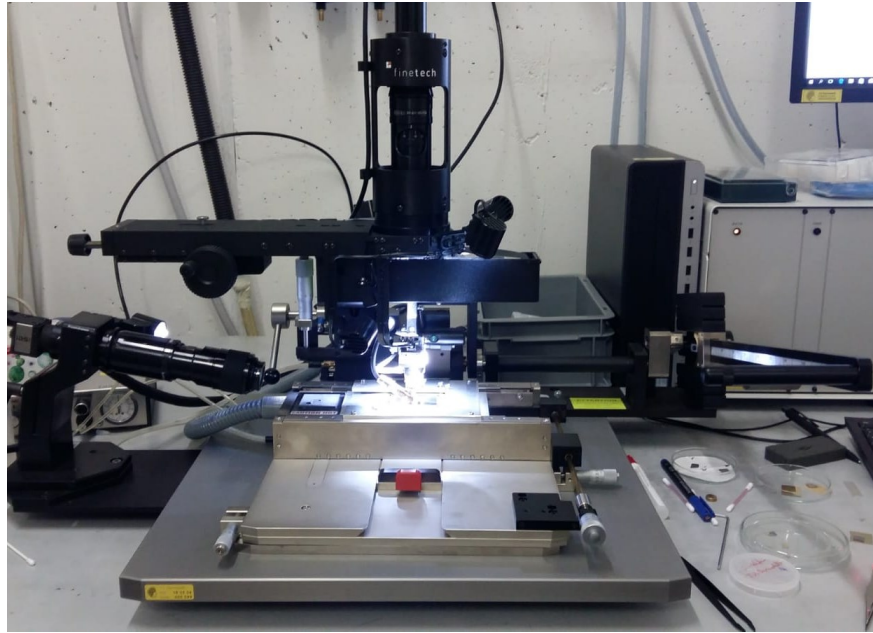


Figure 50. FlipChip bonding machined, during bonding.

6.1.5 Dielectric layer manufacturing

The top layer is made of material Arlon CuClad217 with dielectric permittivity of 2.2. Processes performed on each dielectric sample:

- Samples were diced into 1 cm x 1 cm squares.
- Negative photoresist nLOF was applied.
- Spinning the dielectric samples with the photoresist in the spin coater with the speed of 4000 rotations per minute.
- Samples were baked at 110°C for 1 min.
- The mask was aligned and the sample was exposed to light for 10 s.
- Samples were again baked at 110°C for 1 min.
- Sample was put in the developer AZ726MIF with constant motion for 1 min, put for 20 s in H₂O and later put into running H₂O for 3 s.
- The achieved photoresist structures were 3μm thick.

- Sample was stuck by duct tape to a plastic holder
- Plastic holder was placed in the etching machine and the copper was etched with Fe_3Cl for 50s.
- The holder with the samples was rinsed with water.
- Using the CNC drilling machine, the holes of 0.4 mm and 1.6 mm in diameter were drilled in the dielectric.
- For the 4x4 antenna array, the smaller holes were not drilled as there were problems with the CNC drilling machine alignment.

As the last step of the antenna manufacture and assembly, the dielectric layer was aligned and stuck on top of the silicon layers with tiny drops of super glue using the bonding machine for alignment (no heat was applied). Figure 51 depicts the top view of the two of the manufactured antennas.

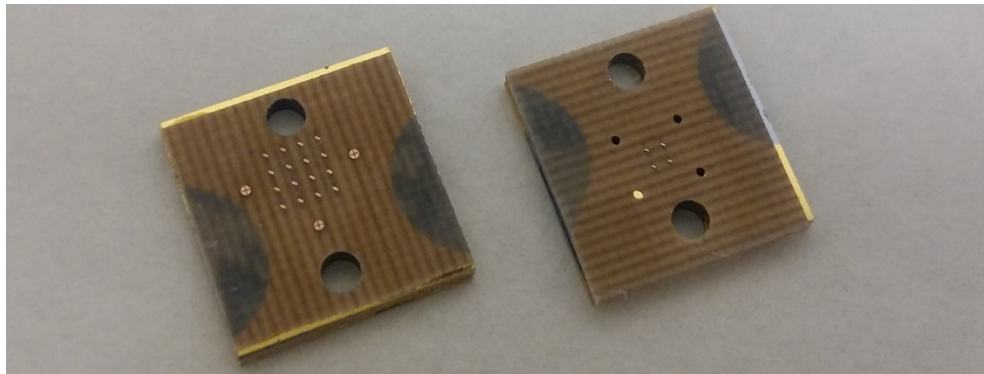


Figure 51. Manufactured 4x4 and 2x2 antenna arrays.

6.1.6 Assembly of the antenna

The antenna was glued to the WR2.2 flange using the bonding machine for alignment without any heat applied and the pressure of 20 N. The flange makes it possible to connect the VNA in order to measure the antenna. Without the flange, the antenna would have to be precisely placed on the waveguide which was not possible in our lab and could possibly destroy the antenna structure. The antenna attached to a flange is presented in Figure 52.



Figure 52. Manufactured 2x2 antenna array attached to WR2.2 flange.

6.2 MEASUREMENTS

6.2.1 Reflection Coefficient Measurements

The antenna measurements took place in the Warsaw University of Technology laboratory. The manufactured antennas were connected to a VNA through a frequency extender and a standard WR2.2 waveguide. The measurement set up is shown in Figure 53.

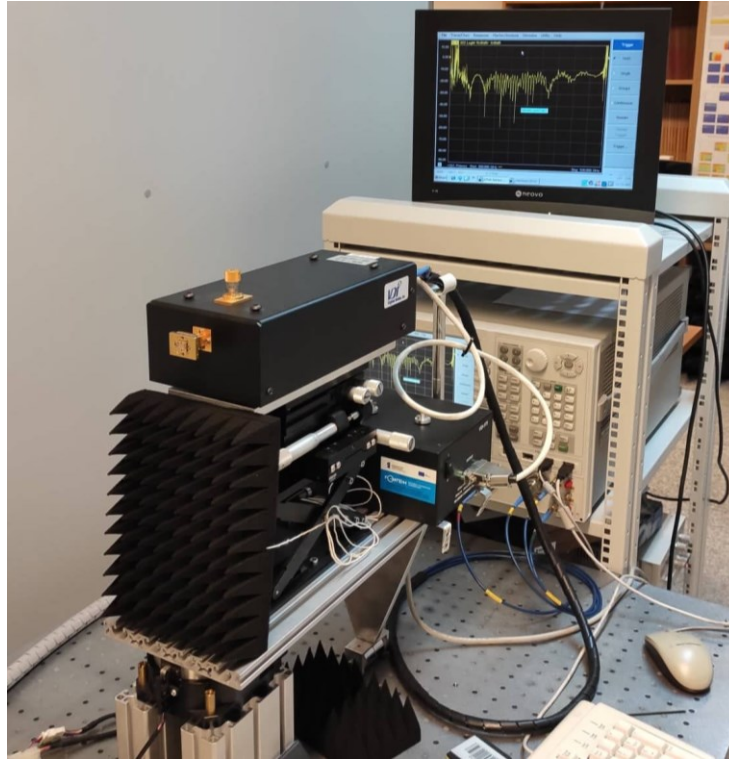


Figure 53. VNA measurement setup.

Two manufactured 2x2 antenna arrays and two manufactured 4x4 antenna arrays were connected to the VNA and their reflection coefficient was measured. In Figure 54, the reflection coefficient of the two 2x2 antenna arrays is plotted together with the reflection coefficient from the simulation of this antenna. Similarly, in Figure 55, the reflection coefficient of the two 4x4 antenna arrays is plotted together with the simulated reflection coefficient of this antenna. Deviations are due to manufacturing inaccuracies such as over-etching of the slots and cavities and high surface roughness, caused by laser cutting. Therefore, another simulation was added to the graph, taking manufacture inaccuracies into account (decreased conductivity, dimensions of slots and cavity varying within $\pm 30 \mu\text{m}$). The simulation with manufacture inaccuracies is similar to the measured results.

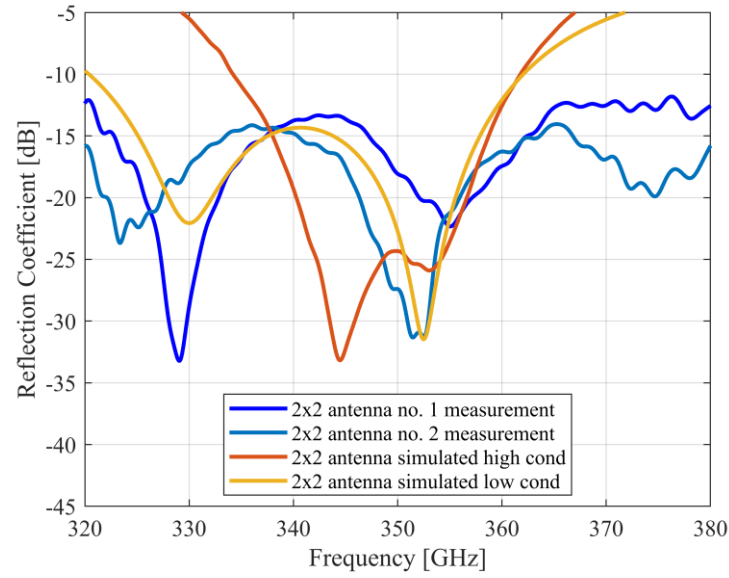


Figure 54. Measured frequency response of the reflection coefficient compared with the simulated one for the 2x2 antenna array.

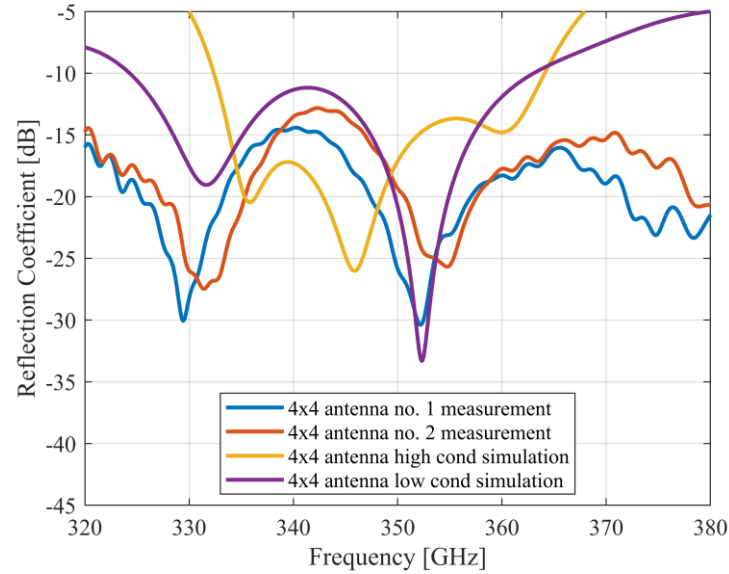


Figure 55. Measured frequency response of the reflection coefficient compared with the simulated one for the 4x4 antenna array

Radiation characteristics, gain and efficiency could not be measured in the laboratory of Warsaw University of Technology because only one frequency extender that operating in this frequency range was available. Multiple requests have been made to other research institutes in Europe but no other laboratory with suitable frequency extender was found. More laboratories and cleanrooms with proper manufacturing and measurement equipment are needed in Europe in order for European THz antenna research to become competitive.

6.2.2 Surface Roughness Measurements

To investigate the sources of deviations in the reflection coefficient measurement results the surface roughness was measured by a scanning probe microscope in CEITEC cleanroom. A picture of the scanned surface is presented in Figure 56. Black rectangles visible in the picture are due to the performed bonding, and are elevated from the lighter color surface by around $1\text{ }\mu\text{m}$. The profile of the tested surface without the elevated black rectangles is presented in Figure 57.

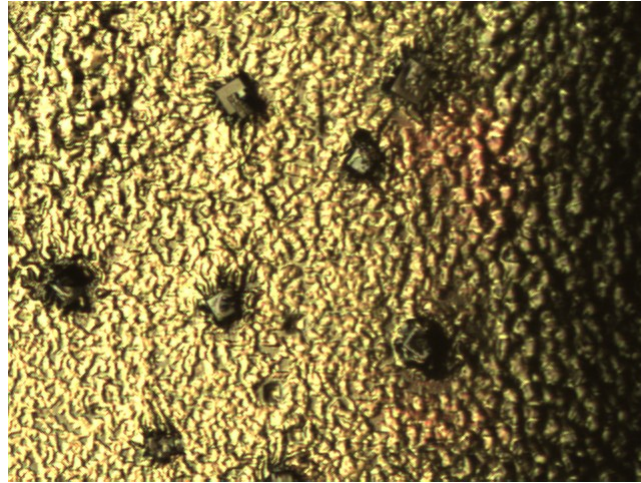


Figure 56. A photo of the surface tested for the surface roughness; the captured surface is roughly $200\text{ }\mu\text{m} \times 250\text{ }\mu\text{m}$. Image prepared from measurement by Scanning Probe Microscope.

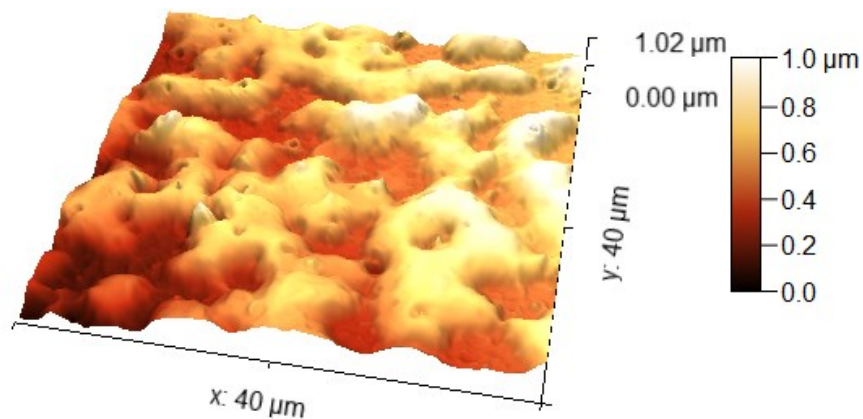


Figure 57. Surface roughness profile of $40\text{ }\mu\text{m} \times 40\text{ }\mu\text{m}$ spot within the area presented in Figure 53. Image prepared from measurement by Scanning Probe Microscope.

In addition to the surface roughness measurements, by Scanning Probe Microscope, the surface of the manufactured sample and the inside of a vertical wall were viewed under Focused Ion Beam Scanning Electron Microscope in CEITEC cleanroom.

The surface of the manufactured antenna sample is presented in Figure 58. The presented area has the rough size of $4\text{ }\mu\text{m} \times 4\text{ }\mu\text{m}$. The inside of the large alignment circle is shown in Figure 59, the presented area has the rough size of $500\text{ }\mu\text{m} \times 500\text{ }\mu\text{m}$. Four layers are

visible in the picture. It can be observed that some parts are not coated with gold and the over surface roughness seems high. Close up view of the upper layer from Figure 59 is shown in Figure 60. The rough size of the presented surface is $150\text{ }\mu\text{m} \times 150\text{ }\mu\text{m}$.

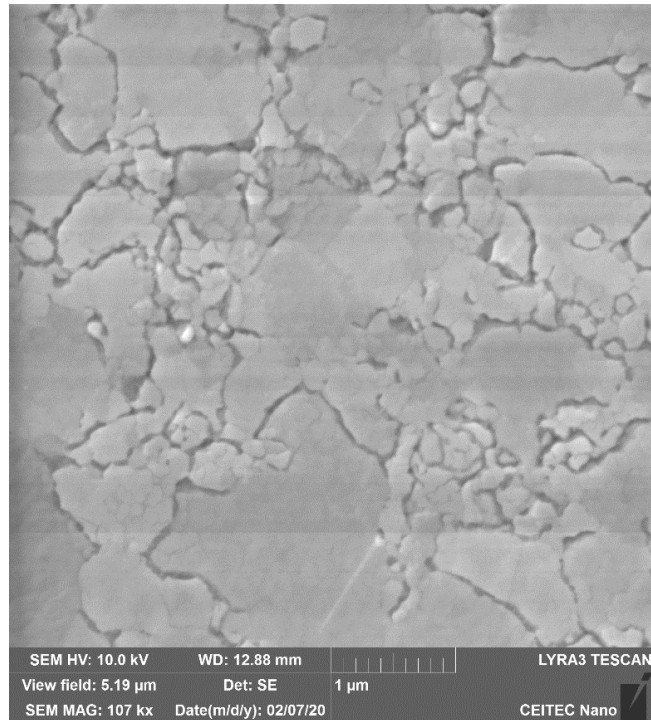


Figure 58. Surface of the metalized silicon layer of the manufactured antenna sample. Image from Focused Ion Beam, Scanning Electron Microscope.

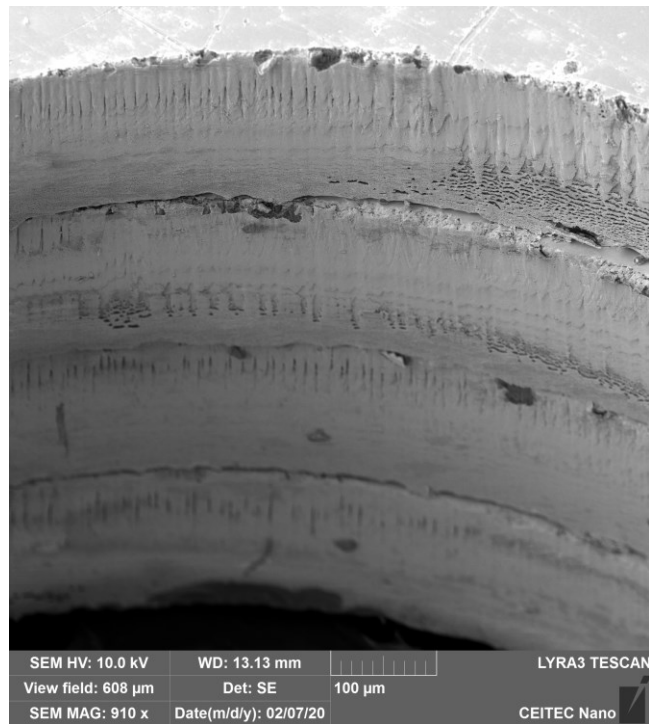


Figure 59 View of the inside of the big alignment circle of the antenna prototype. Image from Focused Ion Beam, Scanning Electron Microscope.

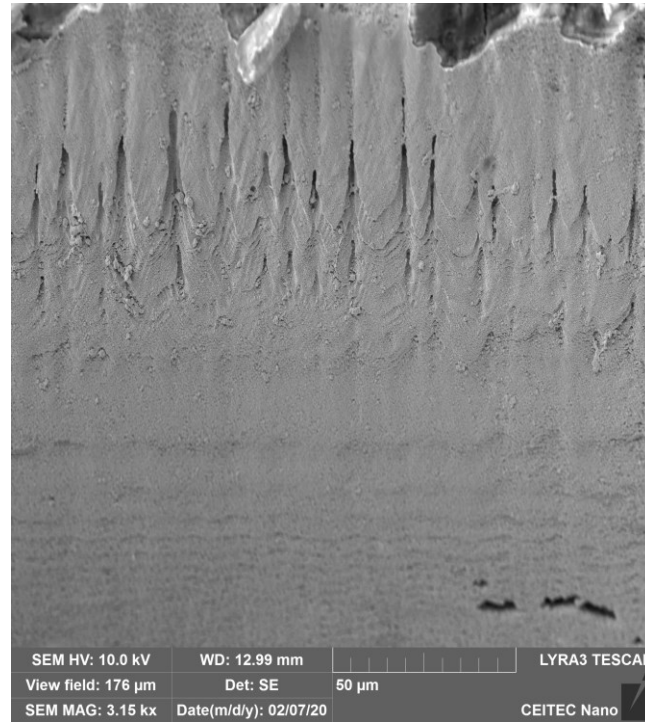


Figure 60. Close up view of the upper layer shown in Figure 47. Image from Focused Ion Beam, Scanning Electron Microscope.

The average surface roughness (RMS) was calculated, from the measurements by Scanning Probe Microscope, to be 500 nm which is higher than the gold layer thickness on the antenna surface. Hence, the laser cutting caused the average value of the surface roughness to be as high as the thickness of the layer of the antenna. This roughness decreased the conductivity and introduced losses. Moreover, the inaccuracy of the cutting changed the sizes of the slots and cavities resulting in changed resonance and coupling parameters. In the future manufacture of the antenna, the laser cutting will be avoided. Instead, a deep reactive ion etching should be used.

6.3 SUMMARY

In this chapter, the microfabrication of the antenna is presented. Each step of the manufacturing including structures etching, wafer dicing, gold evaporation, bonding, dielectric layer fabrication and assembly are discussed in detail. The presented technology is cheaper and more available than traditional micromachining. Four antenna arrays were manufactured by the described technology.

The antenna performance is characterized by the reflection coefficient measurements conducted by a VNA. Deviations between the simulated results and the measured ones are obtained due to a lower surface roughness. Surface roughness was measured and included in the simulations to explain the deviations.

7 LOW-PROFILE ANTENNA FOR SPACE APPLICATIONS

In corporate feed, multilayer antenna arrays, radiating slots are fed with cavities and waveguides placed below them without any movable mechanical elements. Such a solid multilayer design results in a significant performance while maintaining a low-profile and reliable operation. Those qualities make the antenna a good fit for CubeSats communication links. In this chapter, a corporate feed, multilayer 8x8 antenna array operating with circular polarization at 35 GHz is presented. The antenna has a higher gain, a wider bandwidth, and much more compact size than state-of-art antennas demonstrated in [53] and [54].

7.1 DESIGN OF ANTENNA ARRAY AT 35 GHZ

7.1.1 Design of a 2×2 antenna element

The 2x2 antenna element from chapter 5 is scaled down to 35 GHz. The antenna consists of four metallic layers, with hollow waveguides, slots and cavities. The height of each metallic layer is 2 mm.

The antenna structure is completed by a dielectric layer with metallic patches. The dielectric layer of a height 1,27 mm is made from Arlon Cuclad 217 [80]. The E-bend was not included in the design of the 2×2 antenna for simplification. The antenna design with parameters is presented in Figure 61.

The design was scaled. However the waveguide dimensions had to be selected to agree with the waveguide WR standards for the 35 GHz band. The WR-22 was chosen with the size 5.69 mm x 2.845 mm and the cut-off frequency 26.346 GHz. Some adjustments of the dimensions were made to achieve good results. The dimensions of the designed antenna are given in Table 5.

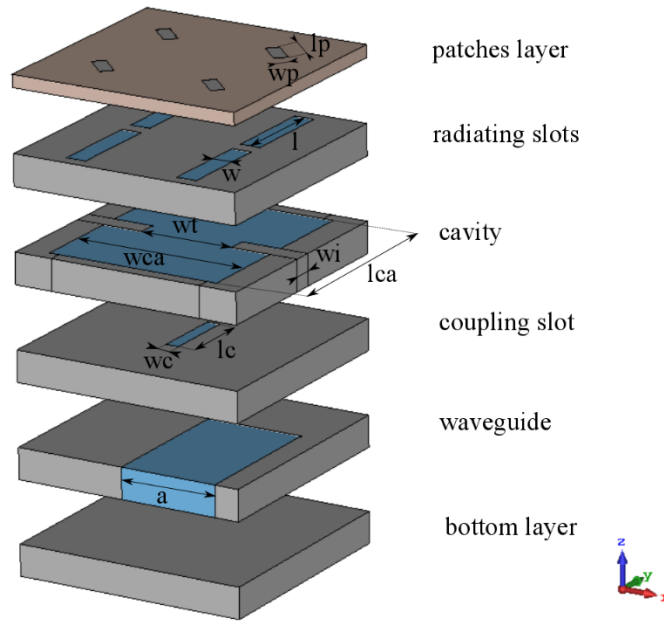


Figure 61. The cell consisting of 2x2 patches. The distance between layers was added to show the whole design.

Table 5. Dimensions of the single-cell antenna at 35 GHz in mm.

Layer	Parameter definition	Parameter
Patches	Patches length (lp)	2.45
	Patches width (wp)	1.1
	Thickness of the top layer (h)	0.787
	Element spacing	7.72
Radiating slots	Slots length (l)	6.8
	Slots width (w)	1.03
	Slots offset in x-axis	0.75
Cavity	Cavity length (lca)	6.25
	Cavity width (wca)	6.22
	Distance between the iris walls	7
	Iris walls thickness (wi)	1.36
Coupling slot	Slot length (lc)	5.8
	Slot width (wc)	0.78
Waveguide	Waveguide width (a)	5.69

7.1.2 Simulation results for 2x2 antenna element

A 2×2 array element of the antenna was analyzed in CST Microwave Studio. The antenna is designed in a manner that enables expansion to a larger array. The reflection coefficient response in frequency has the minimum at 35 GHz and the bandwidth of

0.76 GHz. The plot is presented in Figure 62.

The antenna radiates waves with left-handed circular polarization. The peak gain achieved by the antenna is 13.5 dBi. The axial ratio bandwidth is 5.7 GHz. The axial ratio and the realized gain of LHCP plots in frequency are presented in Figure 63. The directivity patterns of the RHCP and LHCP radiation in $\Phi = 0^\circ$ and $\Phi = 90^\circ$ are presented in Figure 64.

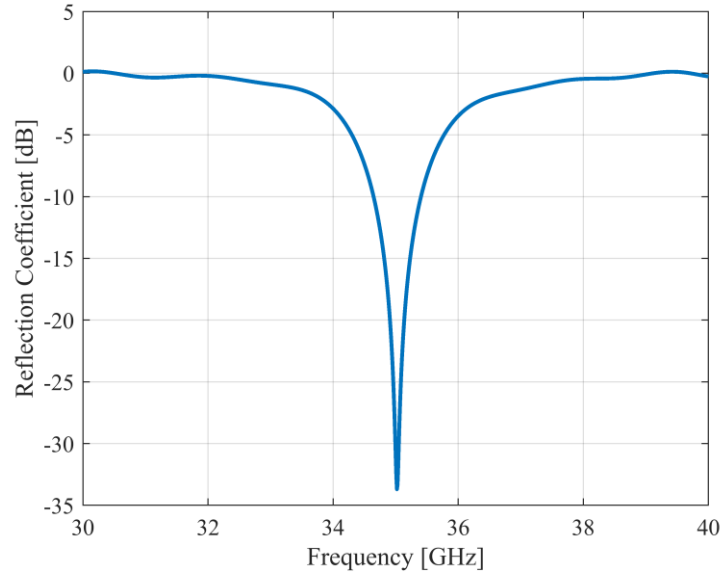


Figure 62. The reflection coefficient in the frequency of the 2x2 array element.

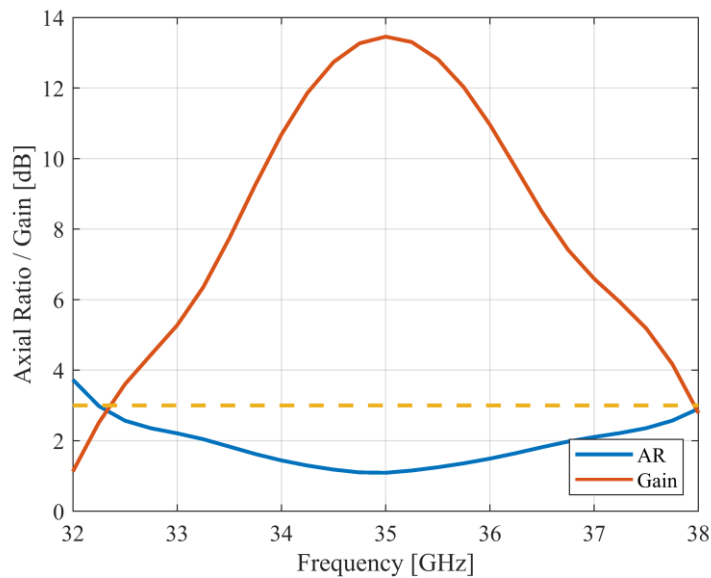


Figure 63. Axial ratio and realized gain for the LHCP in frequency of the 2x2 array element.

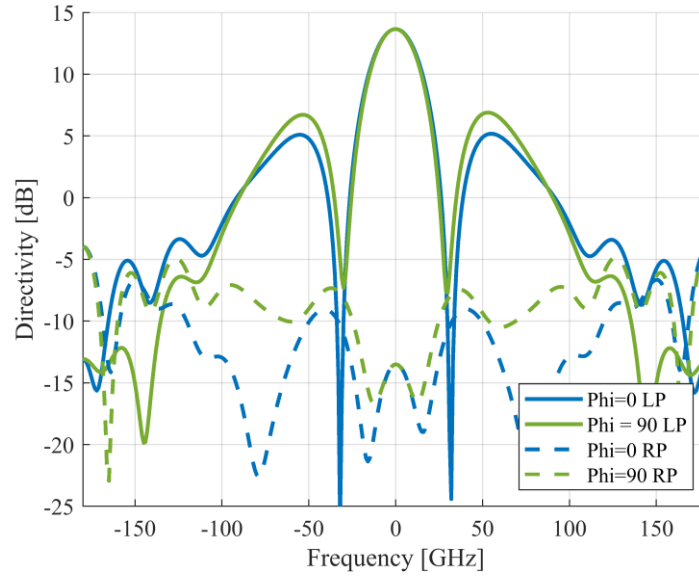


Figure 64. Directivity patterns of the LHCP and RHCP radiation in $\Phi = 0^\circ$ and $\Phi = 90^\circ$.

7.2 PROTOTYPE AT 9 GHZ

As a proof of concept, a prototype of the 2×2 array was scaled down to a central frequency of 9 GHz and manufactured from polylactic acid (PLA) by the 3D printing technique. The printed structure was metalized by a nickel spray paint. This fabrication technology provides several benefits for prototyping such as rapid manufacturing, an efficient cost, and a lightweight.

7.2.1 Antenna and transition design

The design of the antenna is corresponding with the design presented above but was scaled down to 9 GHz for a fast and cost-effective prototype manufacture. The top dielectric layer is fully made from PLA in this design.

At 9 GHz, it is easier to feed the antenna with a coaxial cable than a waveguide. Therefore, a transition from a coaxial connector to a waveguide was designed. The coaxial to waveguide transition is presented in Figure 65.

The transmission coefficient of the transition is -0.4 dB at 35 GHz.

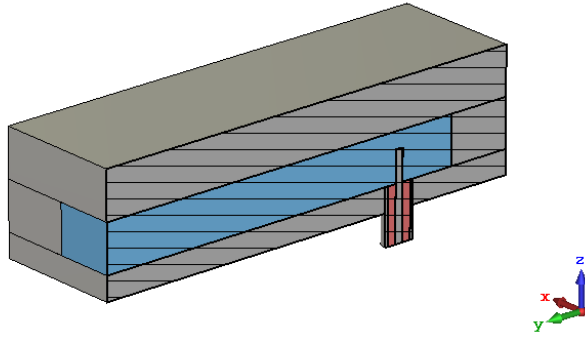


Figure 65. Coaxial to waveguide transition, YZ cut.

7.2.2 Prototype manufacturing

The antenna was manufactured in 4 pieces by the 3D printing in PLA. The functional surfaces of the PLA were metalized by a nickel spray. The patches were manufactured by a standard lithography process and glued to the top PLA layer. The dielectric permittivity of the PLA varies depending on the filling factor. Here, the permittivity was assumed to be 2.7 as measured in [86].

The manufactured antenna is presented in Figure 66.

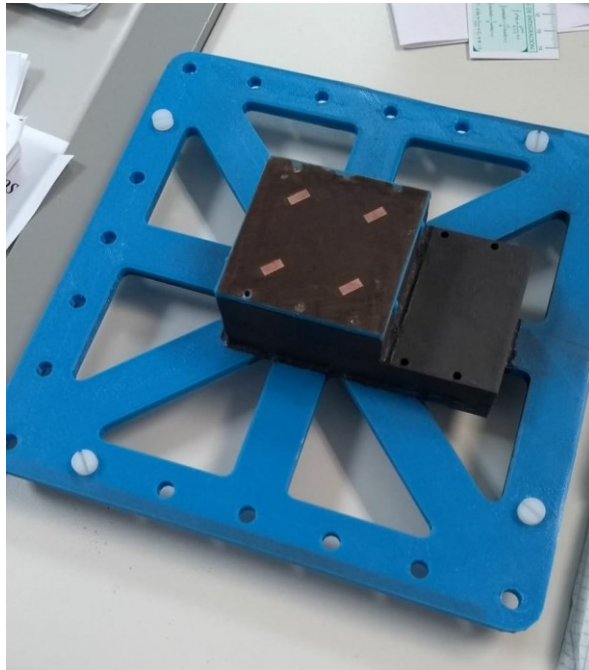


Figure 66. The 2x2 antenna prototype manufactured by 3D-printing.

7.2.3 Measurements

The simulated and measured reflection coefficients are shown in Figure 67. A small shift in the resonance frequency (about 1.4 GHz) was observed. The reason for this behavior seems to be the problem with the manufacture which was further investigated.

Axial ratio curves were prepared based on the radiation pattern measurements and are presented in Figure 68. It can be noticed that the axial ratio minima is slightly shifted to the lower frequencies. The shift probably happened because of changes in the filling factor of the PLA which caused a change of its dielectric permittivity. This was not considered as a significant problem, because the top dielectric layer can be easily redesigned and manufactured again to accommodate these inaccuracies.

The comparison of the measured and simulated radiation patterns is presented in Figure 69 and Figure 70 for different cut planes. Measured and simulated radiation patterns are in agreement and the measurements prove circular polarization operation of the antenna.

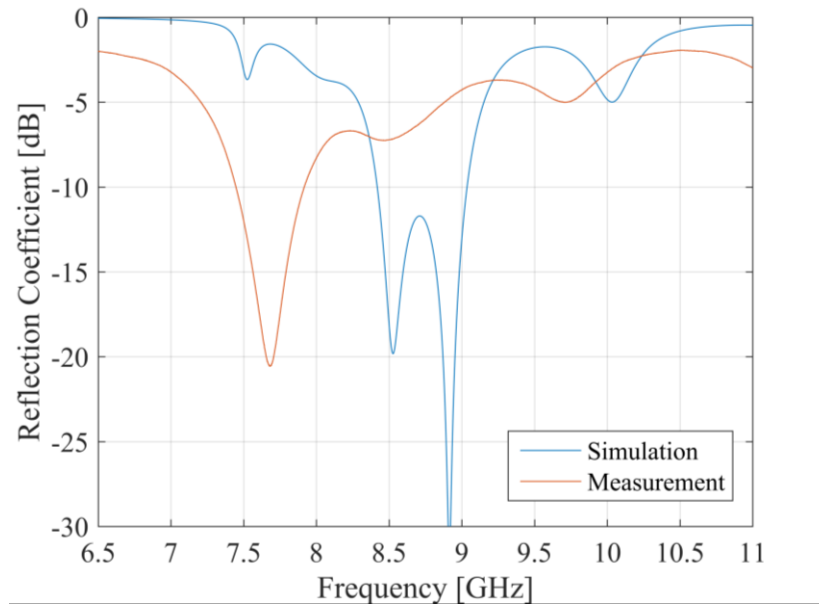


Figure 67. Measured and simulated reflection coefficient of the antenna prototype on 9 GHz.

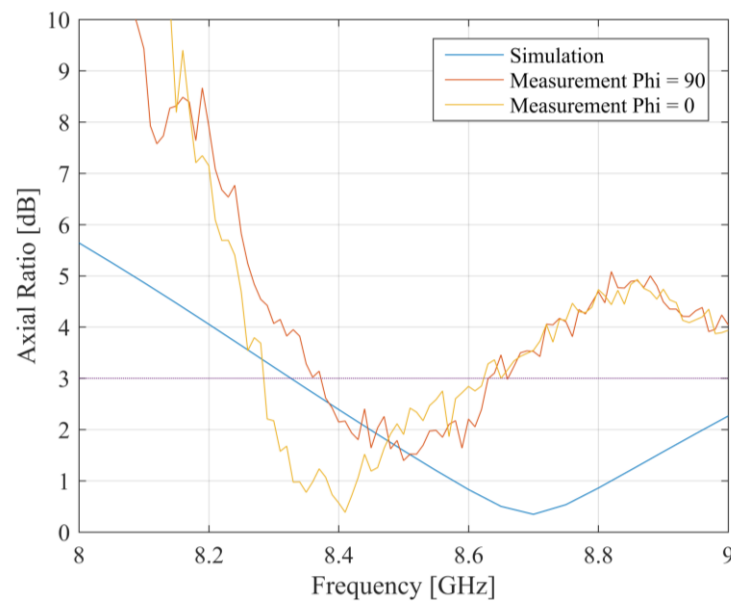


Figure 68. Measured and simulated axial ratio of the 9 GHz antenna.

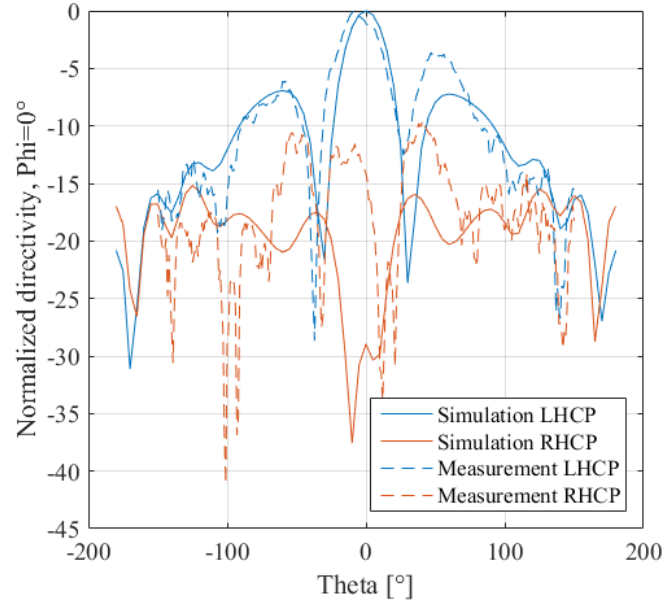


Figure 69. Comparison of the measured and simulated radiation pattern of the antenna prototype on 9 GHz, in the $\phi=0^\circ$ plane.

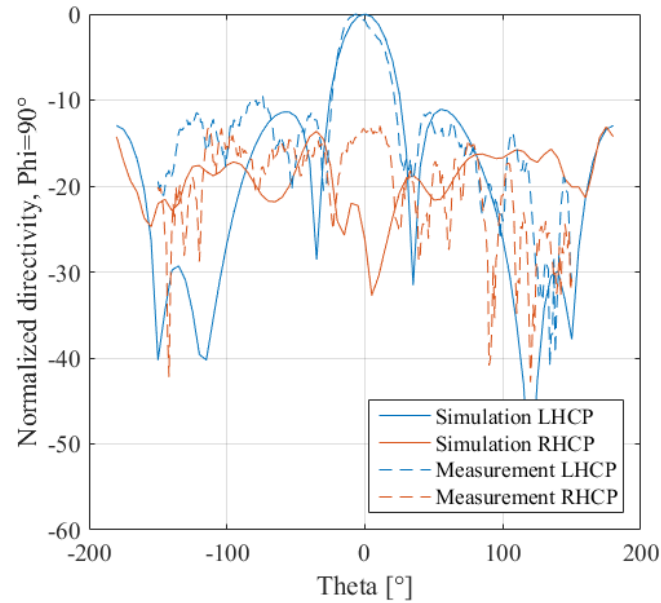


Figure 70. Comparison of the measured and simulated radiation pattern of the antenna prototype on 9 GHz, in the $\phi=90^\circ$ plane

The minor discrepancies in the results occurred, however the prototype confirmed the overall impressive performance of this antenna design at 9 GHz.

7.2.4 Dielectric waveguide analyses

In order to find out the exact manufacture problem, that was the reason for the reflection coefficient shift, tests with a simpler structure were performed.

Simple dielectric waveguide fed with a coaxial probe and ended with a radiating slot was designed. The waveguide was manufactured by 3D printing and metalized in two different ways: by sticking copper strips and by spraying copper spray. The

manufactured structures are presented in Figure 71.



Figure 71. Dielectric waveguides with radiating slots metalized with copper spray (left) and copper stripes (right).

Frequency responses of the reflection coefficient of the manufactured structures were measured. A structure with the identical design and a copper metallization was also analyzed in CST Microwave Studio. Obtained reflection coefficient in frequency is shown in Figure 72. The reflection coefficient for the fabricated structure with copper strips is presented in Figure 73 and the one for the fabricated structure with copper spray in Figure 74.

It can be observed that the measurement results of the waveguide metalized with copper strips correspond well with the simulated results, although the S_{11} levels are not so low in the resonances. However, for the waveguide metalized with the nickel spray, the measurement results do not correspond with the simulated ones (there are no resonances at all). Therefore it was concluded that the method of metallization using the nickel spray is not reliable and is likely the cause for the reflection coefficient mismatch of the antenna prototype operated at 9 GHz.

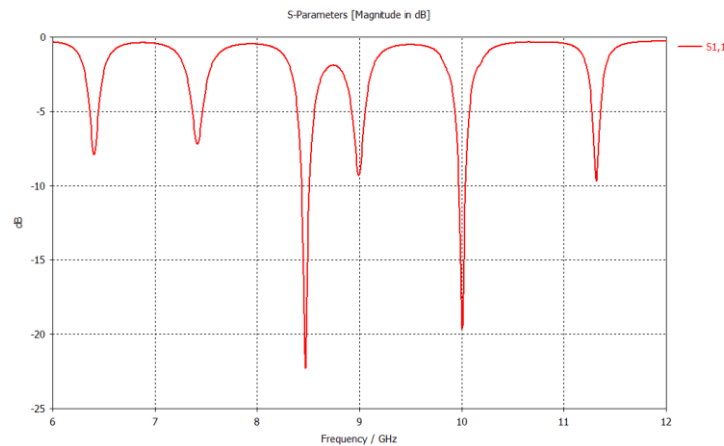


Figure 72. Simulated reflection coefficient of the dielectric waveguide with the radiating slot.

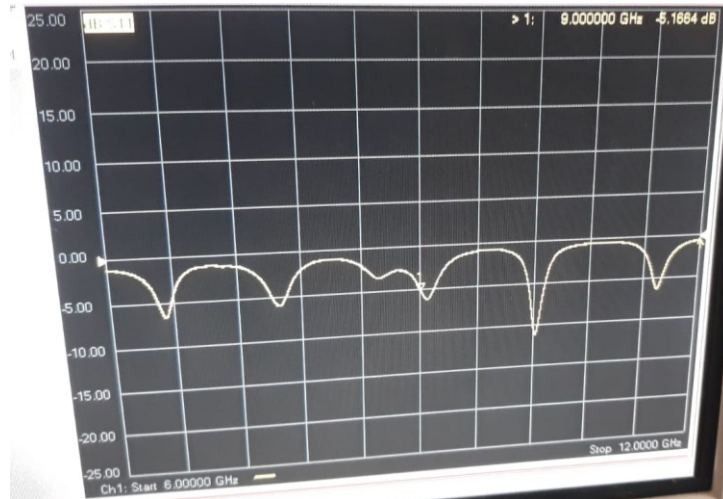


Figure 73. Measured reflection coefficient of the dielectric waveguide with radiating slot, metalized with copper strips.

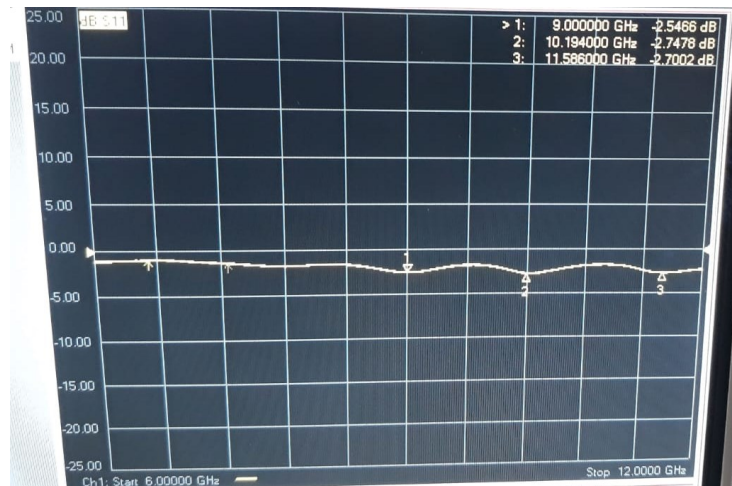


Figure 74. Measured reflection coefficient of the dielectric waveguide with radiating slot, metalized with copper spray.

7.3 THE 8X8 ANTENNA ARRAY AT 35 GHZ

7.3.1 Antenna design

The 2×2 antenna was expanded into an 8×8 array. The antenna consists of five metallic layers, with hollow waveguides, slots and cavities and one dielectric layer with metallic patches. The antenna design is presented in Figure 75. The 8x8 structure is corresponding to the 2x2 design presented in section 5.2.1. The array was expanded from 4 elements to 64 and the feeding system was added into the waveguide layer. The feeding layer consists of T and H shaped power dividers that guide and divide the signal equally to the coupling slots.

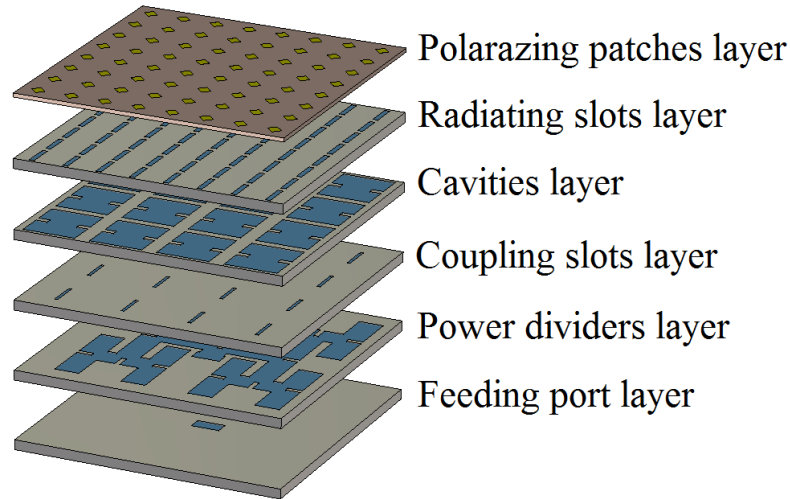


Figure 75. The 8×8 antenna array design.

7.3.2 Simulation results

The central operation frequency of the antenna is 35 GHz with the impedance bandwidth and the axial ratio bandwidth of 1.1 GHz. The antenna achieves a peak gain of 26.5 dBi. The gain is over 26 dBi in the whole band. The gain and axial ratio plots are presented in Figure 76.

The radiation patterns of the antenna are shown in Figure 77. They present a co-polar / cross-polar level in broadside ($\theta = 0^\circ$) greater than 25 dB with a front-to-back ratio higher than 35 dB. Parameters of the antenna array were optimized by the full-wave simulation in CST Microwave Studio.

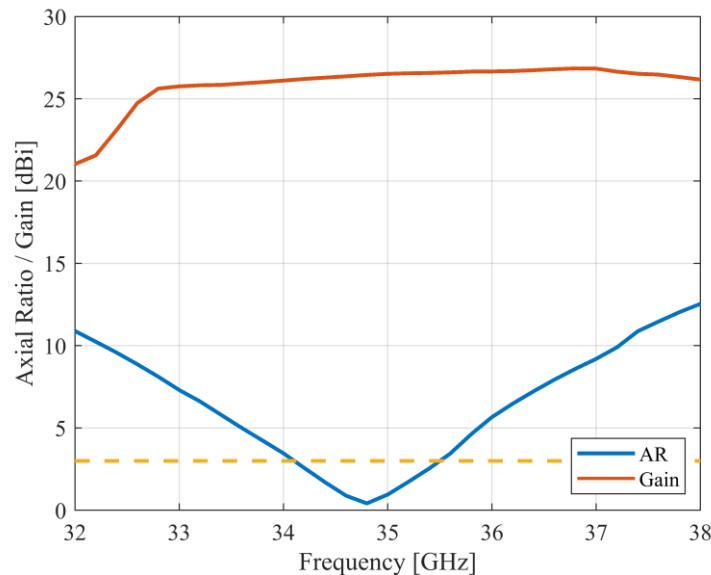


Figure 76. The 8x8 antenna array gain and axial ratio plotted in frequency.

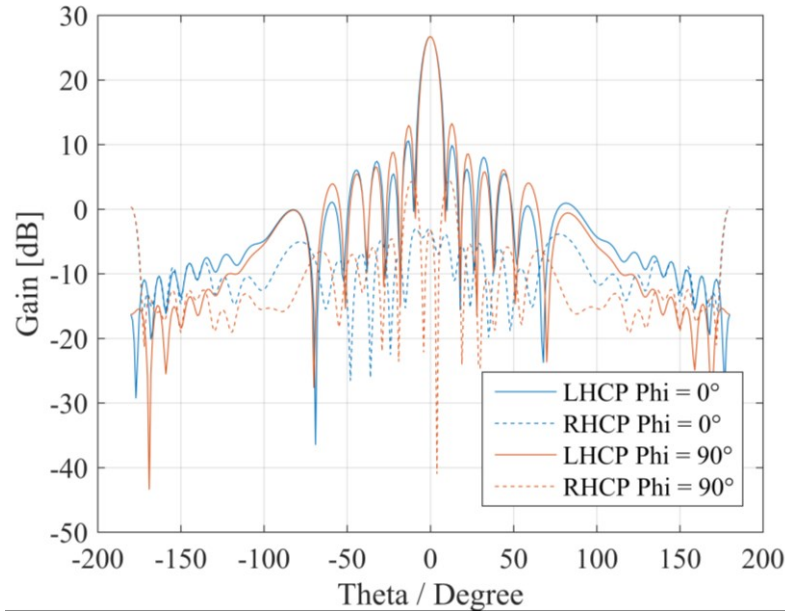


Figure 77. Radiation patterns in gain, $\theta = 0^\circ$ and $\theta = 90^\circ$, of the 8x8 antenna array at 35 GHz.

7.3.3 Manufacturing

The antenna was manufactured by CNC machining. However the results were not acceptable, a lot of inaccuracies were visible, and therefore another method was sought. The results of the CNC drilling manufacture is presented in Figure 78.

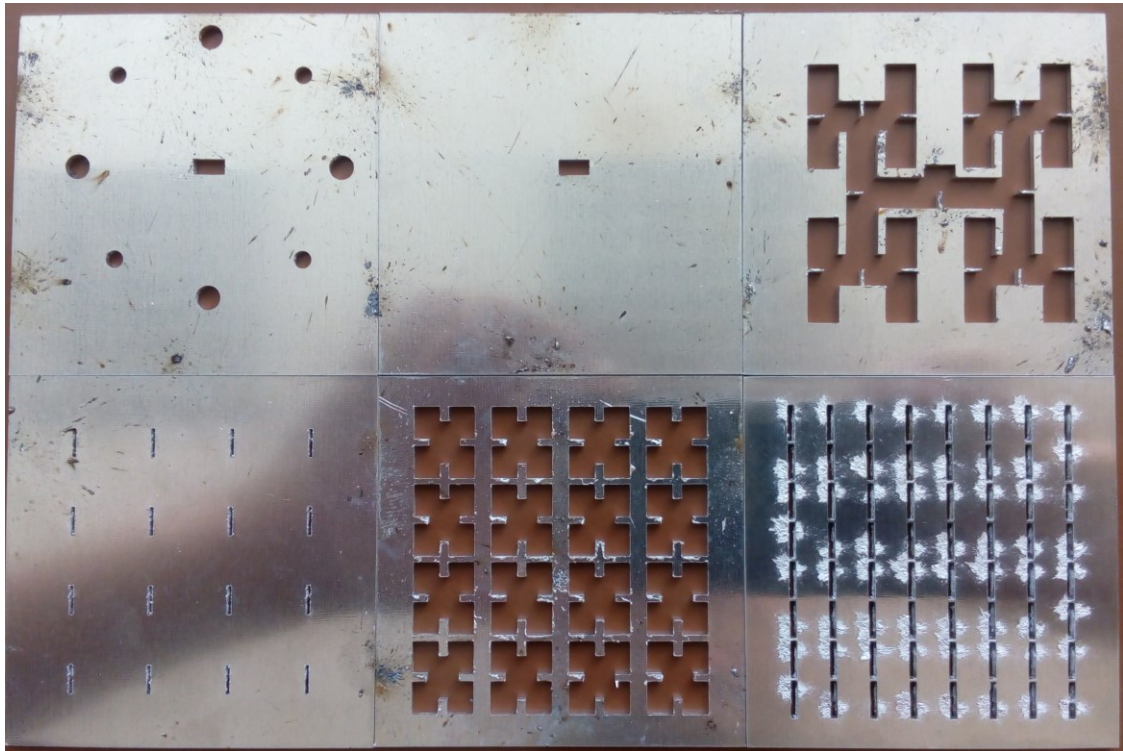


Figure 78. Results of the CNC machining antenna manufacturing.

The antenna was prepared for manufacture by wire cutting in the Penta company in Brno. Technical drawings of the antenna were prepared. Unfortunately because of unpredicted financial issues, the antenna could not be manufactured.

7.3.4 Comparisons with state of art

The designed antenna is compared with the state-of-art circularly polarized antenna designed for CubeSats [54]. The designed antenna size is $55 \text{ mm} \times 55 \text{ mm}$, which corresponds to a total area of $6 \times 6 \lambda_0$. This design is a more compact with an area of only 51% of the area of the antenna presented in [54]. The impedance bandwidth is 1.6% wider than in case of the antenna from [54].

The designed antenna has higher gain, higher co-polar to cross-polar level and much more compact size than state-of-art antennas demonstrated in [53] and [54]. The presented comparisons show that the antenna is a great fit for CubeSats applications.

Table 6. Comparison of circularly polarized antennas for CubeSats applications with this work. Center frequency f_c and impedance bandwidth BW .

Ref.	Design	f_c (GHz)	Size (λ_0)	BW (%)	Max gain (dBi)	Co-polar/ Cross- polar in the broadside (dB)	Sidelobe level
[53]	Helical antenna	30	25×0.7	53	21	24	14
[54]	Meta surface antenna	32	7×7	1.5	26	19	15
This work	8x8 slots array	35	6×6	3.1	26.5	26.5	14

7.4 SUMMARY

A circularly polarized 8x8 antenna array operating in Ka-band was designed with a peak gain of 26.5 dBi, $40 \lambda_0^2$ size, and bandwidth of 1.1 GHz. The antenna provides a higher gain and a wider bandwidth with a more compact design compared to state-of-art antennas. This makes it a great fit for a communication antenna on a CubeSat.

A prototype of the antenna was manufactured with 3D printing at 9 GHz as a proof of the concept. A good agreement between the simulated and measured radiation patterns was found and circular polarization was confirmed.

8 CONCLUSIONS

The original contribution of this thesis lies in the area of high-gain circularly polarized THz antenna design, proper modeling of thin metallic structures at THz frequencies and a description of cheaper and more available manufacture technology. Moreover, the generality of the antenna design is proven by scaling down the antenna to a lower frequency.

Modeling of metal at THz frequencies was discussed in terms of the Drude model and different conductivity measurements. Comparison of modeling approaches for metallic structures was done and the best methods were selected based on the skin depth relation with metal thickness [87].

Circularly polarized corporate feed antenna array suitable for communications applications was designed. The antennas operate at 350 GHz with 2×2 and 4×4 element configuration. The designs include the possibility of extension to a larger array and take into consideration the fabrication possibilities at THz frequencies. The designed antenna arrays radiate waves with circular polarization, have polarization and impedance bandwidths of 25 GHz and 30 GHz, with peak gains 13.8 dBi and 18.4 dBi, respectively. Antenna arrays have a low profile of only $1.3 \lambda_0$. According to the author's knowledge, the developed antennas are the first 350 GHz circularly polarized antennas with such high gain, wide bandwidth, low size and possibility to be easily extended to a larger array [87]. The designed 2×2 antenna element is analyzed by different methods and solvers and the best methods are recommended depending on the requirements [88].

The designed antenna array was expanded to an 8×8 antenna array with beam steering capabilities. The phase shifters were implemented in the feeding layer. The antenna radiates a highly directive beam with circular polarization. The beam steering is possible in two dimensions: horizon and elevation with the maximum steering capability from -8° to 8° with gain remaining above 21 dBi for all the beam directions. The designed antenna is an excellent fit for communications applications that require beam steering.

To fulfill the third objective, different manufacturing technologies were compared. The reactive ion etching was tested, however the laser cutting was eventually chosen to etch the structures. The 2×2 and 4×4 antenna arrays were manufactured in the microfabrication process. The manufacturing steps including etching, dicing, gold evaporation, bonding, lithography and assembly were described in detail [89]. The antenna reflection coefficient was measured and compared with simulations. Small discrepancies are associated with increased surface roughness of the layers. The surface roughness was measured by a scanning probe microscope and observed by scanning electron microscope and the assumptions were confirmed [87]. The radiation patterns of the antenna could not be measured because of the inability to find a suitably equipped laboratory in Europe. In order for European researchers to take the leading role in successful THz antenna design more well equipped clean rooms and measurement laboratories are necessary.

To verify the generality of the design, the THz antenna was scaled down to a Ka-band. The obtained circularly polarized 8x8 antenna array achieved a peak gain of 26.5 dBi, $7 \times 7 \lambda_0$ size, and bandwidth of 1.1 GHz. The antenna provides a higher gain with a more compact design compared to state-of-art antennas. This makes it a great fit for a communication antenna on a CubeSat. A prototype of the antenna was manufactured with 3D printing on 9 GHz as a proof of the concept. A good agreement between the simulated and measured radiation patterns was found and circular polarization was confirmed [90].

Many interesting areas for future research open up based on the work presented in this dissertation thesis. Current commercial electromagnetic solvers do not deal well with simulating THz designs. Functionalities that allow to accurately account for possible manufacture inaccuracies, for example increased surface roughness, could be very beneficial for THz antenna designers.

In relation to chapter 5, the future research could include the designed antenna array extension to a larger array to further increase the gain. Furthermore, by removing the dielectric layer and instead including additional layer of oblique shaped slots. In such way, the whole antenna design can be implement fully in silicon substrate, while maintaining the circular polarization. To improve the manufacturing technology, deep reactive ion etching can be employed for smoother surface of the etched structures and lower losses related to the inaccuracies.

Another interesting research direction is passive phase shifters operating at THz frequencies. Not much work has been done in the field of passive phase shifters at this frequency range. Moreover, not only simulation, but actual implementation of liquid crystal or carbon nanotube based phase shifters in a THz antenna would be a novelty.

Dealing with chapter 7, further research should include fabrication and measurements of the designed antenna at 35 GHz to verify its usability for satellite communications such as CubeSats. Furthermore, beam steering can be implemented in the waveguides of the feeding system of the antenna, for example by including liquid crystal filled dielectric rod waveguides.

REFERENCES

- [1] K. R. Jha and G. Singh, *Terahertz Planar Antennas for Next Generation Communication*. Cham: Springer International Publishing, 2014.
- [2] X.-C. Zhang and J. Xu, *Introduction to THz Wave Photonics*. Boston, MA: Springer US, 2010.
- [3] Y.-S. Lee, *Principles of Terahertz Science and Technology*. Boston, MA: Springer US, 2009.
- [4] I. Uchendu and J. R. Kelly, "Survey Of Beam Steering Techniques Available For Millimeter Wave Applications," *Prog. Electromagn. Res. B*, vol. 68, no. 1, pp. 35–54, 2016.
- [5] L. Mayhew, "Millimeter-Wave (MMW) Radio Transmission: Atmospheric Propagation, Link Budget and System Availability," *Light. White Pap. Ser.*, 2010.
- [6] P. B. K. and D. B. R. N. G. Alexopoulos, "Substrate Optimization for Integrated Circuit Antennas," in *1982 IEEE MTT-S International Microwave Symposium Digest*, 1982, pp. 190–192.
- [7] J. Baker-Jarvis, M. Janezic, and D. Degroot, "High-frequency dielectric measurements," *IEEE Instrum. Meas. Mag.*, vol. 13, no. 2, pp. 24–31, Apr. 2010.
- [8] J. A. Hejase, S. Member, P. R. Paladhi, S. Member, and P. P. Chahal, "Terahertz Characterization of Dielectric Substrates for Component Design and Nondestructive Evaluation of Packages," vol. 1, no. 11, pp. 1685–1694, 2011.
- [9] G. Maral and M. Bousquet, *Satellite Communications System Techniques and Technology*. Sussex, U.K.: John Wiley & Sons, Ltd., 2009.
- [10] F. E. Nathanson, *Radar design principles*, Second Edi. New Jersey: SciTech Publishing, Inc., 1991.
- [11] O. Malyuskin and V. Fusco, "Wideband circular polarised antenna with high polarisation purity over a wide angular range," in *2012 6th European Conference on Antennas and Propagation (EUCAP)*, 2012, pp. 2764–2765.
- [12] L. Sun, G. Ou, Y. Lu, and S. T, "Axial Ratio Bandwidth of a Circularly Polarized Microstrip Antenna," in *Advancement in Microstrip Antennas with Recent Applications*, InTech, 2013, pp. 229–246.
- [13] D. F. Guan, C. Ding, Z. P. Qian, Y. S. Zhang, Y. Jay Guo, and K. Gong, "Broadband High-Gain SIW Cavity-Backed Circular-Polarized Array Antenna," *IEEE Trans. Antennas Propag.*, vol. 64, no. 4, pp. 1493–1497, 2016.
- [14] D. Warmowska and Z. Raida, "Circularly Polarized Antenna Array Fed by Substrate Integrated Waveguide : Implementation Recommendations Circularly Polarized Antenna Array Fed by Substrate Integrated Waveguide : Implementation Recommendations," *Electrorevue*, vol. 19, no. 5, pp. 160–167, 2017.

-
- [15] D. Warmowska, M. Marek, and Z. Raida, "MATLAB-based Multi-objective Optimization of Broadband Circularly Polarized Antennas," in *IET Conference Publications*, 2017, vol. 2017, no. CP732.
 - [16] H. Maune *et al.*, "Liquid crystal technology for reconfigurable satcom applications," in *2017 Topical Workshop on Internet of Space (TWIOS)*, 2017, pp. 1–4.
 - [17] D. V. Lioubtchenko, I. V. Anoshkin, I. I. Nefedova, J. Oberhammer, and A. V. Raisanen, "W-band phase shifter based on optimized optically controlled carbon nanotube layer," in *2017 IEEE MTT-S International Microwave Symposium (IMS)*, 2017, pp. 1188–1191.
 - [18] D. Chicherin, M. Sterner, D. Lioubtchenko, J. Oberhammer, and A. V. Räsänen, "Analog-type millimeter-wave phase shifters based on MEMS tunable high-impedance surface and dielectric rod waveguide," *Int. J. Microw. Wirel. Technol.*, vol. 3, no. 5, pp. 533–538, Oct. 2011.
 - [19] S. Smirnov *et al.*, "Optically controlled dielectric properties of single-walled carbon nanotubes for terahertz wave applications," *Nanoscale*, vol. 10, no. 26, pp. 12291–12296, 2018.
 - [20] R. Reese *et al.*, "Liquid crystal based dielectric waveguide phase shifters for phased arrays at W-band," *IEEE Access*, vol. 7, pp. 127032–127041, 2019.
 - [21] O. Kodheli *et al.*, "Satellite Communications in the New Space Era: A Survey and Future Challenges," *IEEE Commun. Surv. Tutorials, Prepr.*, pp. 1–45, Feb. 2020.
 - [22] H. Caleb, "SpaceX submits paperwork for 30,000 more Starlink satellites," *SpaceNews*, pp. 10–12, 2019.
 - [23] R. M. Bilotta and E. B. Brown, "Spiral antennas and antenna arrays," *IEEE Antennas Propag. Soc. AP-S Int. Symp.*, vol. 1 A, no. 2, pp. 342–345, 2005.
 - [24] A. D. J. Fernandez Olvera, U. Nandi, J. Norman, A. C. Gossard, H. Roskos, and S. Preu, "Dispersive properties of self-complementary log-periodic antennas in pulsed THz systems," in *2017 42nd International Conference on Infrared, Millimeter, and Terahertz Waves (IRMMW-THz)*, 2017, pp. 1–2.
 - [25] S. Al-Daffaie, O. Yilmazoglu, A. Jumaah, and F. Kuppers, "First Demonstration of Continuous Wave Terahertz Radiation from Semi-Insulating GaAs Photomixer with Nanowire," in *2018 43rd International Conference on Infrared, Millimeter, and Terahertz Waves (IRMMW-THz)*, 2018, vol. 2018-Septe, pp. 1–2.
 - [26] A. Jumaah, S. Al-Daffaie, O. Yilmazoglu, F. Kuppers, and T. Kusserow, "Interdigital multilayer-graphene nanoelectrodes for continuous wave terahertz photomixers," in *Proceedings of European Microwave Conference in Central Europe, EuMCE 2019*, 2019, no. May, pp. 265–267.
 - [27] A. Mir and J. Yu, "Broadband circular polarized cross bow tie antenna for terahertz range," in *2014 IEEE Antennas and Propagation Society International Symposium (APSURSI)*, 2014, pp. 416–417.
 - [28] C. Lee *et al.*, "Terahertz antenna arrays with silicon micromachined-based microlens antenna and corrugated horns," in *2015 International Workshop on Antenna Technology (iWAT)*, 2015, pp. 70–73.
 - [29] W. Hou, Z. Sun, Y. Jiang, Y. Liu, and X. Lv, "A terahertz diagonal multi-layer horn

- antenna based on MEMS technology,” in *2015 IEEE MTT-S International Microwave Workshop Series on Advanced Materials and Processes for RF and THz Applications (IMWS-AMP)*, 2015, no. 1, pp. 1–3.
- [30] C. A. Balanis, *Antenna theory: Analysis and Design*, 2nd Editio. New York: John Wiley & Sons, Inc., 1997.
 - [31] K. Pitra, Z. Raida, and J. Lacik, “Low-profile circularly polarized antenna exploiting fabry-perot resonator principle,” *Radioengineering*, vol. 24, no. 4, pp. 898–905, 2015.
 - [32] B. A. Zeb and K. P. Esselle, “A partially reflecting surface with polarization conversion for circularly polarized antennas with high directivity,” in *2012 International Conference on Electromagnetics in Advanced Applications*, 2012, pp. 466–469.
 - [33] R. Orr, G. Goussetis, and V. Fusco, “Design method for circularly polarized fabry-perot cavity antennas,” *IEEE Trans. Antennas Propag.*, vol. 62, no. 1, pp. 19–26, 2014.
 - [34] C. A. Balanis, *Modern Antenna Handbook*. Hoboken: Wiley, 2008.
 - [35] K. A. Abdalmalak *et al.*, “Ultrawideband Conical Log-Spiral Circularly Polarized Feed for Radio Astronomy,” *IEEE Trans. Antennas Propag.*, vol. 68, no. 3, pp. 1995–2007, 2020.
 - [36] E. García-Muñoz *et al.*, “Photonic-based integrated sources and antenna arrays for broadband wireless links in terahertz communications,” *Semicond. Sci. Technol.*, vol. 34, no. 5, p. 54001, 2019.
 - [37] W. Hou, Z. Sun, Y. Jiang, Y. Liu, and X. Lv, “A terahertz diagonal multi-layer horn antenna based on MEMS technology,” in *2015 IEEE MTT-S International Microwave Workshop Series on Advanced Materials and Processes for RF and THz Applications (IMWS-AMP)*, 2015, pp. 1–3.
 - [38] A. Rivera-Lavado *et al.*, “Planar Lens-Based Ultra-Wideband Dielectric Rod Waveguide Antenna for Tunable THz and Sub-THz Photomixer Sources,” *J. Infrared, Millimeter, Terahertz Waves*, vol. 40, no. 8, pp. 838–855, Aug. 2019.
 - [39] A. Rivera-Lavado *et al.*, “Design of a Dielectric Rod Waveguide Antenna Array for Millimeter Waves,” *J. Infrared, Millimeter, Terahertz Waves*, vol. 38, no. 1, pp. 33–46, Jan. 2017.
 - [40] M. Geiger, M. Hitzler, and C. Waldschmidt, “A flexible dielectric leaky-wave antenna at 160 GHz,” in *2017 47th European Microwave Conference (EuMC)*, 2017, vol. 2017-Janua, pp. 240–243.
 - [41] D. Kim, J. Hirokawa, M. Ando, J. Takeuchi, and A. Hirata, “ 64×64 -element and 32×32 -element slot array antennas using double-layer hollow-waveguide corporate-feed in the 120 GHz band,” *IEEE Trans. Antennas Propag.*, vol. 62, no. 3, pp. 1507–1512, 2014.
 - [42] K. M. Luk *et al.*, “A microfabricated low-profile wideband antenna array for terahertz communications,” *Sci. Rep.*, vol. 7, no. 1, pp. 1–11, 2017.
 - [43] K. Tekkouk *et al.*, “Corporate-feed slotted waveguide array antenna in the 350-GHz band by silicon process,” *IEEE Trans. Antennas Propag.*, vol. 65, no. 1, pp. 217–225, 2017.
 - [44] J. Hirokawa, T. Tomura, Y. Miura, M. Zhang, and M. Ando, “Plate-laminated-waveguide corporate-feed slot array antennas with a polarization conversion layer,” in *2011 IEEE MTT-S International Microwave Workshop Series on Millimeter Wave Integration*

- Technologies*, 2011, pp. 29–32.
- [45] P. Lu *et al.*, “Photonic Integrated Chips for Millimeter-Wave and THz Beam Steering Antennas,” in *2019 21st International Conference on Transparent Optical Networks (ICTON)*, 2019, pp. 1–4.
 - [46] A. Gomez-Torrent *et al.*, “A Low-Profile and High-Gain Frequency Beam Steering Subterahertz Antenna Enabled by Silicon Micromachining,” *IEEE Trans. Antennas Propag.*, vol. 68, no. 2, pp. 672–682, 2020.
 - [47] K. Sarabandi, A. Jam, M. Vahidpour, and J. East, “A Novel Frequency Beam-Steering Antenna Array for Submillimeter-Wave Applications,” *IEEE Trans. Terahertz Sci. Technol.*, vol. 8, no. 6, pp. 654–665, 2018.
 - [48] H. Jalili and O. Momeni, “Scalable wideband and wide-angle beam steering mm-wave/THz radiator and phased arrays in silicon,” in *Asia-Pacific Microwave Conference Proceedings, APMC*, 2019, vol. 2018-Novem, pp. 1157–1159.
 - [49] S. Rey, T. Merkle, A. Tessmann, and T. Kurner, “A phased array antenna with horn elements for 300 GHz communications,” in *ISAP 2016 - International Symposium on Antennas and Propagation*, 2017, pp. 122–123.
 - [50] W. Fuscaldo *et al.*, “A reconfigurable multilayered THz leaky-wave antenna employing liquid crystals,” in *2017 11th European Conference on Antennas and Propagation, EUCAP 2017*, 2017, pp. 849–851.
 - [51] N. Chahat *et al.*, “CubeSat Deployable Ka-Band Mesh Reflector Antenna Development for Earth Science Missions,” *IEEE Trans. Antennas Propag.*, vol. 64, no. 6, pp. 2083–2093, 2016.
 - [52] C. Han, J. Huang, and K. Chang, “A high efficiency offset-fed X/Ka-dual-band reflectarray using thin membranes,” *IEEE Trans. Antennas Propag.*, vol. 53, no. 9, pp. 2792–2798, 2005.
 - [53] J. Che *et al.*, “6 GHz to 40 GHz CubeSat Radiometer Antenna System,” *IEEE Trans. Antennas Propag.*, vol. 67, no. 5, pp. 3410–3415, 2019.
 - [54] D. Gonzalez Ovejero, X. Morvan, N. Chahat, G. Chattopadhyay, R. Sauleau, and M. Ettorre, “Metallic Metasurface Antennas for Space,” in *12th European Conference on Antennas and Propagation (EuCAP 2018)*, 2018, no. 1, pp. 372–372.
 - [55] S. Pandey, B. Gupta, A. Chanana, and A. Nahata, “Non-Drude like behaviour of metals in the terahertz spectral range,” *Adv. Phys. X*, vol. 1, no. 2, pp. 176–193, 2016.
 - [56] N. Laman and D. Grischkowsky, “Terahertz conductivity of thin metal films,” *Appl. Phys. Lett.*, vol. 93, no. 5, pp. 1–4, 2008.
 - [57] T. A. Baginski, R. N. Dean, and E. J. Wild, “Micromachined planar triggered spark gap switch,” *IEEE Trans. Components, Packag. Manuf. Technol.*, vol. 1, no. 9, pp. 1480–1485, 2011.
 - [58] M. Beiley, J. Leung, and S. S. Wong, “A Micromachined Array Probe Card - Fabrication Process,” *IEEE Trans. Components, Packag. Manuf. Technol.*, vol. 18, no. 1, pp. 179–184, 1995.
 - [59] A. Gomez-Torrent, U. Shah, and J. Oberhammer, “Wideband 220 - 330 GHz Turnstile OMT Enabled by Silicon Micromachining,” in *IEEE MTT-S International Microwave*

- Symposium Digest*, 2018, vol. 2018-June, pp. 1511–1514.
- [60] V. L. Rubio, S. Al-Daffaie, A. Jumaah, and T. Kusserow, “Design and Implementation of a Terahertz Integrated Lens-Antenna for a Nanocontacts Based Photomixer,” in *2019 44th International Conference on Infrared, Millimeter, and Terahertz Waves (IRMMW-THz)*, 2019, vol. 2019-Sept, pp. 1–2.
 - [61] R. Ghodssi and P. Lin, Eds., *MEMS Materials and Processes Handbook*, vol. 1. Boston, MA: Springer US, 2011.
 - [62] H. V. Jansen, M. J. De Boer, S. Unnikrishnan, M. C. Louwerse, and M. C. Elwenspoek, “Black silicon method X: A review on high speed and selective plasma etching of silicon with profile control: An in-depth comparison between Bosch and cryostat DRIE processes as a roadmap to next generation equipment,” *J. Micromechanics Microengineering*, vol. 19, no. 3, 2009.
 - [63] M. D. Henry, C. Welch, and A. Scherer, “Techniques of cryogenic reactive ion etching in silicon for fabrication of sensors,” *J. Vac. Sci. Technol. A Vacuum, Surfaces, Film.*, vol. 27, no. 5, pp. 1211–1216, 2009.
 - [64] R. Dussart, T. Tillocher, P. Lefauchaux, and M. Boufnichel, “Plasma cryogenic etching of silicon: From the early days to today’s advanced technologies,” *J. Phys. D. Appl. Phys.*, vol. 47, no. 12, 2014.
 - [65] D. Tabor, “Macroscopic properties and interatomic forces,” *Phys. Educ.*, vol. 10, no. 7, pp. 487–490, Nov. 1975.
 - [66] G. Humpston and S. J. Baker, “Diffusion bonding of gold,” *Gold Bull.*, vol. 31, no. 4, pp. 131–132, Dec. 1998.
 - [67] E. Jing, B. Xiong, and Y. Wang, “Low-temperature wafer bonding based on gold-induced crystallization of amorphous silicon,” *IEEE Electron Device Lett.*, vol. 31, no. 9, pp. 1011–1013, 2010.
 - [68] Y. Poo, R. X. Wu, X. Fan, J. Q. Xiao, and B. Bin Jin, “An experiment study of gold nano-film’s conductivity at microwave and terahertz frequencies,” in *Asia-Pacific Microwave Conference Proceedings, APMC*, 2010, vol. 2, no. 1, pp. 1452–1454.
 - [69] M. Walther, D. G. Cooke, C. Sherstan, M. Hajar, M. R. Freeman, and F. A. Hegmann, “Terahertz conductivity of thin gold films at the metal-insulator percolation transition,” *Phys. Rev. B*, vol. 76, no. 12, p. 125408, Sep. 2007.
 - [70] J. Baker-Jarvis, M. D. Janezic, and D. C. Degroot, “High-frequency dielectric measurements,” *IEEE Instrum. Meas. Mag.*, vol. 13, no. 2, pp. 24–31, 2010.
 - [71] R. L. Olmon *et al.*, “Optical dielectric function of gold,” *Phys. Rev. B - Condens. Matter Mater. Phys.*, vol. 86, no. 23, pp. 1–9, 2012.
 - [72] M. A. Ordal, R. J. Bell, R. W. Alexander, L. L. Long, and M. R. Querry, “Optical properties of fourteen metals in the infrared and far infrared: Al, Co, Cu, Au, Fe, Pb, Mo, Ni, Pd, Pt, Ag, Ti, V, and W,” *Appl. Opt.*, vol. 24, no. 24, p. 4493, 1985.
 - [73] M. G. Blaber, M. D. Arnold, and M. J. Ford, “Search for the ideal lasmonic nanoshell: the effects of surface scattering and alternatives to gold and silver,” *J. Phys. Chem. C*, vol. 113, no. 8, pp. 3041–3045, 2009.
 - [74] E. J. Zeman and G. C. Schatz, “An accurate electromagnetic theory study of surface

- enhancement factors for silver, gold, copper, lithium, sodium, aluminum, gallium, indium, zinc, and cadmium,” *J. Phys. Chem.*, vol. 91, no. 3, pp. 634–643, 1987.
- [75] N. K. Grady, N. J. Halasa, and P. Nordlander, “Influence of dielectric function properties on the optical response of plasmon resonant metallic nanoparticles,” *Chem. Phys. Lett.*, vol. 339, no. 1–3, pp. 167–171, 2004.
- [76] S. Berciaud, L. Cognet, P. Tamarat, and B. Lounis, “Observation of intrinsic size effects in the optical response of individual gold nanoparticles,” *Nano Lett.*, vol. 5, no. 3, pp. 515–518, 2005.
- [77] Ansoft HFSS, “3D Boundary Manager Boundaries.” [Online]. Available: <http://read.pudn.com/downloads107/ebook/442805/hfss/bound3.pdf>.
- [78] A. Berenguer, M. Baquero-Escudero, D. Sanchez-Escuderos, and F. Vico, “Rigorous method for calculating Gap waveguides impedance using transmission line theory,” in *8th European Conference on Antennas and Propagation EuCAP*, 2014, pp. 2508–2512.
- [79] M. Asaadi and A. Sebak, “High-Gain Low-Profile Circularly Polarized Slotted SIW Cavity Antenna for MMW Applications,” *IEEE Antennas Wirel. Propag. Lett.*, vol. 16, no. c, pp. 752–755, 2017.
- [80] Rogers, “CuClad Series ® PTFE / Woven Fiberglass Laminates Typical Properties.” [Online]. Available: <https://rogerscorp.com/-/media/project/rogerscorp/documents/advanced-connectivity-solutions/english/data-sheets/cuclad-laminates-data-sheet.pdf>.
- [81] J. Joubert and S. R. Rengarajan, “Design of unequal H-plane waveguide power dividers for array applications,” *Microw. J.*, vol. 40, no. 2, pp. 24–34, 1997.
- [82] K. Sarhadi and M. Shahabadi, “Wideband substrate integrated waveguide power splitter with high isolation,” *IET Microwaves, Antennas Propag.*, vol. 4, no. 7, pp. 817–821, 2010.
- [83] P. H. Bolivar *et al.*, “Measurement of the dielectric constant and loss tangent of high dielectric-constant materials at terahertz frequencies,” *IEEE Trans. Microw. Theory Tech.*, vol. 51, no. 4 I, pp. 1062–1066, 2003.
- [84] M. Alibakhshikenari, B. S. Virdee, C. H. See, R. A. Abd-Alhameed, F. Falcone, and E. Limiti, “High-Performance 50 μ m Silicon-Based On-Chip Antenna with High Port-to-Port Isolation Implemented by Metamaterial and SIW Concepts for THz Integrated Systems,” in *2019 Thirteenth International Congress on Artificial Materials for Novel Wave Phenomena (Metamaterials)*, 2019, pp. 23–25.
- [85] Y. Zhao *et al.*, “A 0.54-0.55 THz 2x4 coherent source array with EIRP of 24.4 dBm in 65nm CMOS technology,” in *2015 IEEE MTT-S International Microwave Symposium*, 2015, pp. 1–3.
- [86] S. Zhang, C. C. Njoku, W. G. Whittow, and J. C. Vardaxoglou, “Novel 3D printed synthetic dielectric substrates,” *Microw. Opt. Technol. Lett.*, vol. 57, no. 10, pp. 2344–2346, Oct. 2015.
- [87] D. Warmowska, K. A. Abdalmalak, L. E. G. Munoz, and Z. Raida, “High-gain, Circularly-polarized THz Antenna with Proper Modeling of Structures with Thin Metallic Walls,” *IEEE Access*, pp. 1–11, 2020.

- [88] D. Warmowska and Z. Raida, “High-Gain Circularly Polarized Corporate-Feed Terahertz Antenna Array,” *Proc. 2018 20th Int. Conf. Electromagn. Adv. Appl. ICEAA 2018*, pp. 157–160, 2018.
- [89] D. Warmowska and Z. Raida, “Manufacture of a Corporate-Feed Multilayer Terahertz Antenna Array in Silicon Technology,” in *Asia-Pacific Microwave Conference Proceedings, APMC 2019*, pp. 1–2.
- [90] D. Warmowska, K. A. Abdalmalak, L. E. G. Munoz, and Z. Raida, “A Compact Circularly Polarized High-Gain Antenna Array for Ka-Band CubeSats Applications,” in *2019 IEEE-APS Topical Conference on Antennas and Propagation in Wireless Communications (APWC)*, 2019, pp. 178–180.

LIST OF FIGURES

Figure 1. Position of the THz band in the electromagnetic spectrum [1].	2
Figure 2. Atmospheric attenuation in THz and infrared range of the electromagnetic spectrum [1].	4
Figure 3. Satellite spectrum [21].	8
Figure 4. Typical geometries of THz antenna elements: a) log-spiral antenna, b) log-periodic antenna, c) bow-tie antenna.	10
Figure 5. Directivity of horn antenna with different aperture diameter and antenna height [30].	10
Figure 6. Comparison of results of deep reactive ion etching in mixed mode (cryogenic process) and pulsed mode (Bosch process) [62].	15
Figure 7. Frequency response of the real part of the conductivity obtained analytically and through measurement of dielectric permittivity.	20
Figure 8. Frequency response of the imaginary part of the conductivity obtained analytically and through measurement of dielectric permittivity.	20
Figure 9. Frequency response of the real part of the conductivity calculated by the Drude model, $f_p=2.13$ PHz, f_d varied according to minimum and maximum values available in the literature.	21
Figure 10. Frequency response of the imaginary part of the conductivity calculated by the Drude model, $f_p=2.13$ THz, f_d varied according to minimum and maximum values available in the literature.	21
Figure 11. The real part of the conductivity of gold films at (a) X band, (b) Ka band, (c) THz frequencies. The discrete dots are experimental data; the solid lines are the fittings of the Drude model [68].	22
Figure 12. Model of the waveguide with a thin gold sheet inside.	24
Figure 13. Reflection coefficient at the input port of waveguide as a function of the thickness of a gold wall in the cross-section at 200 GHz.	25
Figure 14. Reflection coefficient at the input port of waveguide as a function of the thickness of a gold wall in the cross-section at 350 GHz.	26
Figure 15. Reflection coefficient at the input port of waveguide as a function of the thickness of a gold wall in the cross-section at 500 GHz.	26
Figure 16. The 2x2 antenna element.	28
Figure 17. The electric (left) and magnetic (right) field distribution in the cavity of the antenna element.	29
Figure 18. The surface current distribution on the patches in the top layer in phases: 0° , 90° , 180° , and 270° .	30
Figure 19. Designed terahertz antenna element a) Y-axis cut, electric field distribution inside the antenna element b) top view.	30

Figure 20. Electric field distribution in the cavity. The cavity a) of half-length, b) of full-length and long iris walls, c) of full-length and optimal iris walls, d) of full-length and no iris walls	32
Figure 21. 4x4 antenna array design.	33
Figure 22. Top view of the feeding system of the 4×4 antenna array with three T-shaped power dividers.	33
Figure 23. Transmission coefficients and reflection coefficient for the input port of the power divider.	34
Figure 24. Simulated reflection coefficient and the left-handed circular polarization realized gain response vs frequency of the 2×2 and 4×4 antenna arrays.....	34
Figure 25. Simulated radiation efficiency of the 2×2 and 4×4 antenna arrays.....	35
Figure 26. Simulated gain for $\theta = 0^\circ$ and $\theta = 90^\circ$ for the right-handed circular polarization (RHCP) and the left-handed circular polarization (LHCP).	35
Figure 27. Directivity of the 4x4 antenna array for $\theta = 0^\circ$	36
Figure 28. Directivity of the 4x4 antenna array for $\theta = 90^\circ$	36
Figure 29. Frequency response of the reflection coefficient of the 2×2 array with under-etching (blue), normal etching (red), and over-etching (yellow).	37
Figure 30. Frequency response of the reflection coefficient of the models with ideal (red) and misaligned (blue) layers.	37
Figure 31. Gain and axial ratio frequency responses of 2×2 array for changing permittivity.....	38
Figure 32. Three analyzed models of the antennas from the left: PEC model, full-gold model and precise model.	40
Figure 33. Frequency response of reflection coefficient at the input port of the antenna array: comparison of different models and solvers.	41
Figure 34. Frequency response of gain and axial ratio of the antenna array: comparison of different models and solvers.	41
Figure 35. Increasing surface roughness (RMS) influence on the reflection coefficient plotted in frequency.	43
Figure 36. Radiation efficiency of the 2x2 antenna array in frequency for increasing gold surface roughness (RMS).	43
Figure 37. Directivity in $\phi = 0^\circ$ of the 2x2 antenna element for different thicknesses of the gold layer.	44
Figure 38. Directivity in $\phi = 90^\circ$ of the 2x2 antenna element for different thicknesses of the gold layer.....	44
Figure 39. The 8×8 antenna with beam steering design capability.....	45
Figure 40. Design of the feeding system of the 8×8 antenna array.	46
Figure 41. 8x8 antenna array directivity, $\theta = 0^\circ$, scanning in azimuth. β describes the progressive phase shift.....	46
Figure 42. 8x8 antenna array directivity for $\theta = 90^\circ$ scanning in elevation. β describes the progressive phase shift.....	47

Figure 43. Axial ratio and gain plot in frequency for the $\theta = 0^\circ$, and $\beta = 0^\circ$. β describes the progressive phase shift.	47
Figure 44. Microfabrication steps of the antennas.	50
Figure 45. Wafer with the 4x4 antenna array layers after dicing into samples.	51
Figure 46. Silicon samples on the holder before gold evaporation.	52
Figure 47. The inside of the gold evaporation chamber.	52
Figure 48. Side view of the 2x2 antenna array before mounting the top layer, taken by the bonding machine camera.	53
Figure 49. 4x4 and 2x2 antennas before mounting the top layer.	54
Figure 50. FlipChip bonding machined, during bonding.	54
Figure 51. Manufactured 4x4 and 2x2 antenna arrays.	55
Figure 52. Manufactured 2x2 antenna array attached to WR2.2 flange.	55
Figure 53. VNA measurement setup.	56
Figure 54. Measured frequency response of the reflection coefficient compared with the simulated one for the 2x2 antenna array.	57
Figure 55. Measured frequency response of the reflection coefficient compared with the simulated one for the 4x4 antenna array	57
Figure 56. A photo of the surface tested for the surface roughness; the captured surface is roughly $200\ \mu\text{m} \times 250\ \mu\text{m}$. Image prepared from measurement by Scanning Probe Microscope.	58
Figure 57. Surface roughness profile of $40\ \mu\text{m} \times 40\ \mu\text{m}$ spot within the area presented in Figure 53. Image prepared from measurement by Scanning Probe Microscope.	58
Figure 58. Surface of the metalized silicon layer of the manufactured antenna sample. Image from Focused Ion Beam, Scanning Electron Microscope.	59
Figure 59. View of the inside of the big alignment circle of the antenna prototype. Image from Focused Ion Beam, Scanning Electron Microscope.	59
Figure 60. Close up view of the upper layer shown in Figure 47. Image from Focused Ion Beam, Scanning Electron Microscope.	60
Figure 61. The cell consisting of 2x2 patches. The distance between layers was added to show the whole design.	62
Figure 62. The reflection coefficient in the frequency of the 2x2 array element.	63
Figure 63. Axial ratio and realized gain for the LHCP in frequency of the 2x2 array element.	63
Figure 64. Directivity patterns of the LHCP and RHCP radiation in $\Phi = 0^\circ$ and $\Phi = 90^\circ$	64
Figure 65. Coaxial to waveguide transition, YZ cut.	65
Figure 66. The 2x2 antenna prototype manufactured by 3D-printing.	65
Figure 67. Measured and simulated reflection coefficient of the antenna prototype on 9 GHz.	66
Figure 68. Measured and simulated axial ratio of the 9 GHz antenna.	66
Figure 69. Comparison of the measured and simulated radiation pattern of the antenna prototype on 9 GHz, in the $\phi=0^\circ$ plane.	67

Figure 70. Comparison of the measured and simulated radiation pattern of the antenna prototype on 9 GHz, in the $\phi=90^\circ$ plane	67
Figure 71. Dielectric waveguides with radiating slots metalized with copper spray (left) and copper stripes (right).	68
Figure 72. Simulated reflection coefficient of the dielectric waveguide with the radiating slot.	68
Figure 73. Measured reflection coefficient of the dielectric waveguide with radiating slot, metalized with copper strips.	69
Figure 74. Measured reflection coefficient of the dielectric waveguide with radiating slot, metalized with copper spray.	69
Figure 75. The 8×8 antenna array design.....	70
Figure 76. The 8×8 antenna array gain and axial ratio plotted in frequency.	70
Figure 77. Radiation patterns in gain, $\theta = 0^\circ$ and $\theta = 90^\circ$, of the 8×8 antenna array at 35 GHz.	71
Figure 78. Results of the CNC machining antenna manufacturing.	71

LIST OF TABLES

Table 1. Values of measured plasma frequency f_p and damping frequency f_d for gold.	19
Table 2 Antenna element parameters given in millimeters.....	29
Table 3. Comparison of high-gain/circularly polarized/THz frequency antennas with this work. Operation frequency f_c , impedance bandwidth BW , and circular polarization CP	39
Table 4. Numerical parameters of models	42
Table 5. Dimensions of the single-cell antenna on 35 GHz in mm.	62
Table 6. Comparison of circularly polarized antennas for CubeSats applications with this work. Center frequency f_c and impedance bandwidth BW	72

LIST OF PUBLICATIONS

1. D. Warmowska, K. A. Abdalmalak, L. E. Garcia Munoz, and Z. Raida, "High-gain, Circularly-polarized THz Antenna with Proper Modeling of Structures with Thin Metallic Walls," *IEEE Access*, pp. 1–11, 2020.
2. D. Warmowska, K. Atia Abdalmalak, L. E. García Muñoz, Z. Raida, "A Compact Circularly Polarized High-Gain Antenna Array for Ka-band CubeSats Applications", *2019 IEEE-APS Topical Conference on Antennas and Propagation in Wireless Communications (APWC)*, Granada 2019, pp. 178-180.
3. D. Warmowska, A. Jumaah, S. Al-Daffaie, O. Yilmazoglu, Z. Raida, "Manufacture of a Corporate-Feed Multilayer Terahertz Antenna Array in Silicon Technology", *Asia-Pacific Conference on Antennas and Propagation, (APCAP)*, Incheon 2019 (in press).
4. D. Warmowska, Z. Raida, "High-Gain Circularly Polarized Corporate-Feed Terahertz Antenna Array," *2018 International Conference on Electromagnetics in Advanced Applications (ICEAA)*, Cartagena des Indias, 2018, pp. 157-160.
5. D. Warmowska, M. Marek, Z. Raida, "MATLAB-based multi-objective optimization of broadband circularly polarized antennas", *Loughborough Antennas and Propagation Conference (LAPC 2017)*, 2017, pp. 1-6.
6. D. Warmowska, Z. Raida, "Circularly Polarized Antenna Array Fed by Substrate Integrated Waveguide: Implementation Recommendations", *Electrorevue Magazine* Vol.19 No.05, 2017.

LIST OF SYMBOLS, PHYSICAL CONSTANTS AND ABBREVIATIONS

β	propagation constant of the gold layer
BUT	Brno University of Technology
BW	impedance bandwidth
γ_i	transverse propagation constant of the i^{th} layer
CELTA	Convergence of Electronics and Photonics Technologies for Enabling Terahertz Applications
CNC	Computerized Numerical Control
CP	circular polarization
DRIE	Deep Reactive Ion Etching
DRW	Dielectric Rod Waveguide
δ	skin depth
ϵ_{cr}^i	relative complex permittivity
E_{tan}	tangential component of the electric field
f_0	operation frequency
f_d	damping frequency
f_p	plasma frequency
FSPL	Free Space Path Loss
H_{tan}	tangential component of magnetic field
λ_0	wavelength at the operational frequency
LHCP	Left-Handed Circular Polarization
μ_r^i	relative complex permeability
\hat{n}	unit normal vector
PCB	Printed Circuit Board
PEC	Perfect Electric Conductor
PLA	Polylactic Acid
RHCP	Right-Handed Circular Polarization
RIE	Reactive Ion Etching

RMS	Average surface roughness, calculated with Root Mean Square method
σ	conductivity
SatComs	Satellite Communications
S_{11}	reflection coefficient
τ_{δ}	electron relaxation time
THz	Tera Hertz
T_i	layer thickness
Z_s	surface impedance
Z^i	intrinsic and impedance of layer i^{th}
Z_{tran}^i	transfer impedance of layer i^{th}
Z_w	characteristic impedance of the waveguide
ω_d	angular damping frequency
ω_p	angular plasma frequency

CURRICULUM VITAE

DOMINIKA WARMOWSKA

Date of birth: 25 February 1992
Nationality: Polish
E-mail: Dominika.Warmowska@gmail.com
Phone: +420 608 125 251

EDUCATION

- 2016.10 - current **Brno University of Technology**
Ph.D. candidate
Thesis subject: THz antenna arrays
- 2015.02 - 2016.08 **Gdańsk University of Technology**
Msc.: Electronics and Telecommunications
- 2011.10 - 2015.02 **Gdańsk University of Technology**
Bsc.: Electronics and Telecommunications

RESEARCH STAYS

- 2018.09 - 2019.01 **Technical University of Darmstadt**
2018.04 - 2019.05 Work in a cleanroom. Micro- and nano- fabrication technologies. Studies on plasma etching, gold evaporation and silicon bonding.
- 2018.04 - 2018.05 **Carlos the Third University in Madrid**
2019.03 - 2019.04 Work on a high gain, low profile, circularly polarized antenna array suitable for CubeSats and space applications.
- 2017.10 - 2018.01 **KTH Royal Institute of Technology in Stockholm**
Studies about micromachining technology, dielectric waveguides and waveguide slot antennas.

WORK EXPERIENCE

- 2016.10 - 2019.10 **Convergence of Electronics and Photonics Technologies for Enabling Terahertz Applications (CELTA)**
Early Stage Researcher, Marie Skłodowska-Curie scholarship beneficiary
International collaboration in order to utilize Terahertz technology for applications for sensing, instrumentation, imaging, spectroscopy, and

communications.

2014.07 - 2014.09 **Powel AS Norway**

Intern in the Strategy and Technology Department

Developing a strategic plan for a new product that Powel was to introduce, conducting market research, analyzing existing solutions, customizing the software to a suitable demo case, developing a user-friendly interface, evaluating success criteria.

2014.06 - 2014.07 **PIT RADWAR**

Intern in the Analog Technologies Department

Designing parts of radiolocation systems, modeling and simulating passive elements, measuring characteristics of antennas, analyzing the outcomes.

2011.11 - 2014.06 **Board of European Students of Technology**

Member of the local group and International Financial Team

Teamwork in organizing local and international student events. Managing finances of the international organization, various soft-skills trainings.